

UNIVERSIDADE FEDERAL DE JUIZ DE FORA
INSTITUTO DE CIÊNCIAS EXATAS / FACULDADE DE ENGENHARIA
PROGRAMA DE PÓS-GRADUAÇÃO EM MODELAGEM
COMPUTACIONAL

Andrés Ricardo Valdez

Inverse and forward uncertainty quantification of models for foam-assisted
enhanced oil recovery

Juiz de Fora
2021

Ficha catalográfica elaborada através do Modelo Latex do CDC da UFJF
com os dados fornecidos pelo(a) autor(a)

Valdez, Andrés Ricardo.

Inverse and forward uncertainty quantification of models for foam-assisted enhanced oil recovery / Andrés Ricardo Valdez. – 2021.

134 p. : il.;29,7cm.

Orientador: Rodrigo Weber dos Santos

Coorientador: Bernardo Martins Rocha

Tese (Doutorado) – Universidade Federal de Juiz de Fora, Instituto de Ciências Exatas / Faculdade de Engenharia. Programa de Pós-Graduação em Modelagem Computacional, 2021.

1. Quantificação de incertezas. 2. Análise de sensibilidade. 3. Expansão em polinomial chaos. 4. Escoamento de espumas em meios porosos. 5. Recuperação avançada de petróleo. I. Weber dos Santos, Rodrigo, orient. II. Martins Rocha, Bernardo, coorient. III. Título.

Andrés Ricardo Valdez

**Inverse and forward uncertainty quantification of models for foam-assisted
enhanced oil recovery**

Tese apresentada ao Programa de Pós-Graduação em Modelagem Computacional da Universidade Federal de Juiz de Fora como requisito parcial à obtenção do título de Doutor em Modelagem Computacional. Área de concentração: Modelagem Computacional.

Orientador: Prof. D.Sc. Rodrigo Weber dos Santos

Coorientador: Prof. D.Sc. Bernardo Martins Rocha

Juiz de Fora

2021

Andrés Ricardo Valdez

Inverse and forward uncertainty quantification of models for foam-assisted enhanced oil recovery

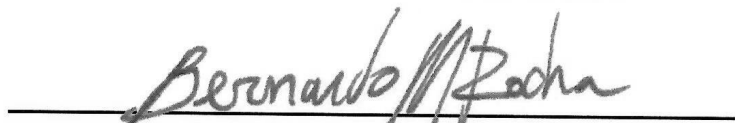
Tese apresentada ao Programa de Pós-Graduação em Modelagem Computacional da Universidade Federal de Juiz de Fora como requisito parcial à obtenção do título de Doutor em Modelagem Computacional. Área de concentração: Modelagem Computacional.

Aprovada em 26 de agosto de 2021

BANCA EXAMINADORA



Prof. D.Sc. Rodrigo Weber dos Santos – Orientador
Universidade Federal de Juiz de Fora



Prof. D.Sc. Bernardo Martins Rocha – Coorientador
Universidade Federal de Juiz de Fora



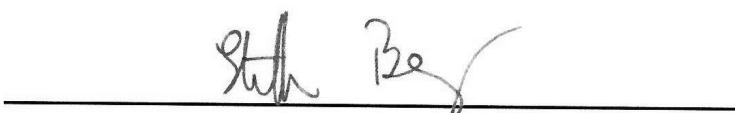
Prof. D.Sc. Grigori Chapiro
Universidade Federal de Juiz de Fora



Prof. Ph.D. Johannes Bruining
Delft University of Technology



Prof. Ph.D. Pacelli Lidio Jose Zitha
Delft University of Technology



Prof. Ph.D. Steffen Berg
Shell Global Solutions International B.V.

I dedicate this work to Anna my wife, and Amelia my princess.

AGRADECIMENTOS

This work reflects part of the efforts, the time, and the energy invested by many people to bring me to this point. Chronologically, I will start mentioning my parents for teaching me that freedom comes with Education; where I come from, this is not the general behavior. Five years ago, I arrived at the Graduate Program in Computational Modeling after a complicated academic situation. Bernardo Rocha and Iury Igreja took me under their mentoring extending always important advice; on more than one occasion, they gave me their opinion on topics that were little related to the academic life; for this, I consider them as my friends. The first lecture I assisted as a master's student was given by Rodrigo Weber (I must confess that) I recognize myself as an average student. However, Rodrigo (and many others) always trusted my capabilities to deliver a meaningful piece of research. I believe this thesis does not belong entirely to myself, but also it is shared with Rodrigo and Bernardo. We live in chaotic days, even before the COVID-19 outbreak. Yet, the chaos was much more fun thanks to Lucão, Ruy, João, Joventino, João Yamin, Lucas, Pedro and Elias. I would like to mention the support and partnership gained from Martin, Felipe, the Santa Fe crew Pablo, Gabriel and Raul, and the Córdoba MeCom-team Adrian, Dario and Francisco. Since my arrival to Juiz de Fora, I was financially supported by FAPEMIG, CAPES, and SHELL Brasil LTDA.; their investments are very well appreciated.

Finally, I will use the last paragraph to thank my wife Anna and my daughter Amelia. This thesis, as well as all the future outcomes, also belongs to them. This time was much easier thanks to the motivation of having them. Gracias.

This research was carried out in association with the ongoing R&D project registered as ANP 20715-9, "*Modelagem matemática e computacional de injeção de espuma usada em recuperação avançada de petróleo*", Universidade Federal de Juiz de Fora (UFJF) / Shell Brasil / ANP. Mathematical and computational modeling of foam injection as an enhanced oil recovery technique applied to Brazil pre-salt reservoirs, sponsored by Shell Brasil under the ANP R&D levy as "*Compromisso de Investimentos com Pesquisa e Desenvolvimento*". This project is carried out in partnership with Petrobras.

Andrés tenés dos alternativas, Estudiar o estudiar.
-Mamá.

RESUMO

Como muitos projetos de engenharia, a recuperação de petróleo, bem como a recuperação avançada de petróleo, são sensíveis ao gerenciamento correto dos recursos econômicos. Ensaios em plantas piloto, bem como experimentos em amostras retiradas do reservatório, são ferramentas fundamentais para estimar o retorno econômico do processo estudado. Nesse sentido, as simulações numéricas aparecem como alternativas acessíveis para resolver diferentes cenários em várias escalas (escala de poros, escala de laboratório, escala de campo). Apesar das muitas vantagens que um simulador tem, eles não são protegidos contra incertezas. Nesta tese mostramos avanços e contribuições na análise de incertezas em simulações bifásicas em meios porosos. A calibração dos modelos foi realizada usando o método de Markov Chain Monte Carlo. Além disso, a incerteza dos parâmetros foi verificada por meio de estudos de identificabilidade revelando os casos em que a incerteza dos parâmetros foi superestimada. A confiabilidade dos modelos foi determinada usando emuladores como a expansão em polinomial chaos, nos casos em que o custo computacional era uma complicação. Uma vez que as incertezas dos modelos foram estimadas, realizamos uma análise de sensibilidade para vincular a incerteza dos modelos com as incertezas nos parâmetros e identificar suas interações. Calculamos os índices Sobol principais e totais para materializar a análise de sensibilidade. Os resultados apresentados nesta tese mostram uma metodologia consistente para estimar e reduzir incertezas em modelos de escoamento de espuma em meios porosos, que por sua vez pode fornecer simulações confiáveis. Essas conclusões são de grande interesse e relevância; no projeto de técnicas adequadas para recuperação avançada de petróleo.

Palavras-chave: Quantificação de incertezas. Análise de sensibilidade. Expansão em polinomial chaos. Escoamento de espumas em meios porosos. Recuperação avançada de petróleo.

ABSTRACT

Like many other engineering applications, oil recovery and enhanced oil recovery are sensitive to the correct administration of economic resources. Pilot tests and core flood experiments are crucial elements to design an enhanced oil recovery (EOR) project. In this direction, numerical simulators are accessible alternatives for evaluating different engineering configurations at many diverse scales (pore, laboratory, and field scales). Despite the advantages that numerical simulators possess over laboratory experiences, they are not fully protected against uncertainties. In this thesis, we show advances in analyzing uncertainties in two-phase reservoir simulations, focusing on foam-based EOR. The methods employed in this thesis analyze how experimental uncertainties affect reservoir simulator's responses. Our framework for model calibration and uncertainty quantification uses the Markov Chain Monte Carlo method. The parametric uncertainty is tested against identifiability studies revealing situations where posterior density distributions with high variability are related to high uncertainties and practical non-identifiability issues. The model's reliability was evaluated by adopting surrogate models based on polynomial chaos expansion when the computational cost was an issue for the analysis. Once we quantified the model's output variability, we performed a global sensitivity analysis to map the model's uncertainty to the input parameters distributions. Main and total Sobol indices were used to investigate the model's uncertainty and highlight how key parameters and their interactions influence the simulation's output. As a consequence of the results presented in this thesis, we show a technique for parameter and uncertainty estimation that can be explored to reduce the uncertainty in foam-assisted oil recovery models, which in turn can provide reliable computational simulations. Such conclusions are of utmost interest and relevance for the design of adequate techniques for enhanced oil recovery.

Keywords: Uncertainty quantification. Global sensitivity analysis. Polynomial chaos expansion. Foam flood experiment. Enhanced oil recovery.

List of Figures

Figure 1	– Detail of production wells in the pre-salt since 2006, adapted from [111].	18
Figure 2	– ANP short term expectation of produced oil and gas considering continental activities (left) and offshore reservoirs operations (right), adapted from [110].	19
Figure 3	– Absolute permeability field for the 36 th layer of the SPE10 project (left) and simulation results of water saturation in a gas flooding experiment (right). (adapted from [34]).	21
Figure 4	– Interpretation of the posterior error-estimation workflow proposed in [134, 135]. Gray lines represent different model's evaluations, whereas color lines represent the (deterministic) "best fit" solution.	24
Figure 5	– Framework to perform inverse-forward uncertainty quantification and sensitivity analysis.	26
Figure 6	– Schematic representation of the removal of a fluid from a porous domain with the injection of a different fluid.	28
Figure 7	– Measurement of removed fluid from the porous domain and assessment of the pressure drops δp during the experiment.	29
Figure 8	– Comparison of different kind of interfaces recognized in the displacement of immiscible fluids in a porous medium.	29
Figure 9	– Relative permeability models vs. model evaluations.	36
Figure 10	– Schematic representation of the LQR-HQR regimes.	40
Figure 11	– LK and CMG-STARs models evaluation vs foam quality.	44
Figure 12	– LK and CMG-STARs models' evaluation vs water saturation.	45
Figure 13	– Main parts of the UQ-SA workflow and it's interactions.	47
Figure 14	– Inverse modeling calibration results and the MAP estimate.	49
Figure 15	– Posterior distributions obtained the parameters α (left) and β (right).	50
Figure 16	– Parametric uncertainty propagation study MC evaluations vs PCE. Solid lines represent the expected values and shaded regions represent the \pm standard deviation.	55
Figure 17	– Comparison between MC and PCE concerning the number of samples.	56
Figure 18	– Relative permeability values for water κ_{rw} and oil κ_{ro} as a function of water saturation S_w for the two datasets from the literature [90, 56].	62

Figure 19 – Summary of parameter values from the results of MCMC for Chierici’s (panels (a) and (b)) and LET (panels (c) and (d)) models considering dataset 1. The panels on the diagonal show the histograms of each model parameter, with dashed vertical lines to indicate the 2th, 16th, 50th, 84th and 98th percentiles of the samples in the marginalized distributions. The off-diagonal panels show projections of the posterior probability distributions of each pair of parameters.	68
Figure 20 – Summary of parameter values from the results of MCMC for Chierici’s (panels (a) and (b)) and LET (panels (c) and (d)) models considering dataset 2. The panels on the diagonal show the histograms of each model parameter, with dashed vertical lines to indicate the 2th, 16th, 50th, 84th and 98th percentiles of the samples in the marginalized distributions. The off-diagonal panels show projections of the posterior probability distributions of each pair of parameters.	69
Figure 21 – Parametric uncertainty propagation study of recovery factors (oil and water cut). Solid lines represent the expected values and shaded regions represent the 90% prediction interval.	71
Figure 22 – Variance based SA results for all QoIs considering the dataset 1.	73
Figure 23 – Variance based SA results for all QoIs considering the dataset 2.	74
Figure 24 – SA results using the LET for dataset 1 considering the LET model parameters and the relative permeability endpoints (κ_w^0 , κ_o^0 , S_{w0} , and S_{o0}) for the analysis.	75
Figure 25 – Density distribution estimated for S_{cpt} using the different models for both datasets.	75
Figure 26 – Schematic drawing of coreflood apparatus used for foam injection.	82
Figure 27 – Foam quality-scan experiment results: (top) pressure drop at steady state, (left) adjusted relative permeability curves adapted from [102]; and (right) apparent viscosity values as function of foam quality.	87
Figure 28 – Kernel density estimates for each parameter posterior distribution of the STARS (left/green) and linear kinetic [5] (right/blue) foam models.	88
Figure 29 – Uncertainty quantification results of (a-b) apparent viscosity; (c-d) mobility reduction factor (MRF); and (e-f) total relative mobility (λ_{rt}) for the STARS (left column) and linear kinetic [5] (right column) foam models. The shaded regions correspond to the 90% prediction interval (90% PI) and the solid lines represent the expected values.	90
Figure 30 – Uncertainty propagation in the pressure drop using STARS (left) and Linear Kinetic (right) models. Box plots of the data evaluated by the MC execution and experimental data (red squares).	91

Figure 31 – Sensitivity analysis using Sobol indices results of (a-b) apparent viscosity; (c-d) mobility reduction factor (MRF); and (e-f) total relative mobility (λ_{rt}) for the STARS (left column) and LK [5] (right column) foam models.	93
Figure 32 – Sensitivity analysis of the pressure drop for different foam quality levels. Main Sobol and total Sobol indices are shown for STARS and linear kinetic (LK).	94
Figure 33 – Experimental records of pressure drop and evaluations of the exponential model.	96
Figure 34 – Uncertainty quantification results of augmented data set: (a-b) apparent viscosity; (c-d) and pressure drop for the STARS (left column) and linear kinetic [5] (right column) foam models. The shaded regions correspond to the 90% prediction interval (90% PI) and the solid lines represent the expected values.	97
Figure 35 – Mobility reduction factor (MRF) and total relative mobility (λ_{rt}) for STARS $\{fmmob = 293.27, SF = 0.437, sfbet = 359.33\}$ and Linear Kinetic $\{C_{mrf} = 276.40, S_w^* = 0.433, A = 152.32\}$	98
Figure 36 – Profile likelihood for the synthetic dataset #1 considering the different objective functions. Red stars correspond to the minimum and dashed green line to the ground truth parameter set.	109
Figure 37 – Posterior PDFs obtained for the synthetic dataset #1.	110
Figure 38 – Forward uncertainty quantification in terms of apparent viscosity and mobility reduction factor for the synthetic dataset # 1.	111
Figure 39 – Profile likelihood comparison analyzing the best fit configurations of the Synthetic dataset #2. Red stars correspond to the minimum.	112
Figure 40 – Posterior density distributions obtained employing the objective functions OF1, OF2, and OF3; employing the Synthetic dataset #2.	112
Figure 41 – Forward uncertainty quantification in terms of apparent viscosity and mobility reduction factor for the synthetic dataset #2.	114
Figure 42 – Posterior density distributions obtained employing the objective functions OF1, OF2, and OF3; employing the Kapetas <i>et al.</i> (2016) dataset.	114
Figure 43 – Forward uncertainty quantification in terms of apparent viscosity and mobility reduction factor for Kapetas <i>et al.</i> (2016) dataset. Top row: uncertainty propagation for the apparent viscosity as function of the foam quality. Bottom row: uncertainty propagation for the mobility reduction factor as function of the foam quality.	115
Figure 44 – Posterior density distributions obtained employing the objective functions OF1, OF2, and OF3; employing the Moradi–Araghi <i>et al.</i> (1997) dataset.	115

- Figure 45 – Summary of forward uncertainty quantification and sensitivity analysis results considering the Moradi–Araghi *et al.* (1997) dataset, comparing the three objective functions. Top row: uncertainty propagation for the apparent viscosity as function of the foam quality. Bottom row: uncertainty propagation for the mobility reduction factor as function of the foam quality. 116
- Figure 46 – Main and total Sobol sensitivity indices for the synthetic dataset #1. Red: *fmmob*, yellow: *SF*, blue: *sfbet*, and green: *epcap*. 118

List of Tables

Table 1 – Evaluation of water–breakthrough instant, saturation of the shock front, mobility ratio at shock front saturation, and relative permeability crossing point, using different relative permeability models.	37
Table 2 – Petrophysical properties of the two core samples [90, 56].	62
Table 3 – Calibrated posterior distribution of model parameters considering the different datasets. For each case, minimum, maximum and the corresponding normal (or log-normal) posterior probability distribution is presented in terms of mean μ and standard deviation σ as $\mathcal{N}(\mu, \sigma)$	70
Table 4 – Uncertainty propagation in terms of expected value (μ), standard deviation (σ) coefficient of variation (CoV) for the QoIs = $\{S_{cpt}, S_f, V(1)\}$	72
Table 5 – Ionic composition of injection water (IW) used in this study.	81
Table 6 – Dimensions and petrophysical properties of Indiana limestone used in this work. L , D , PV , φ , and k are the length, diameter, pore volume, porosity, and permeability of the Indiana Limestone core respectively.	81
Table 7 – Prior and posterior distributions of the parameters in the foam models: STARS and Linear Kinetic [5].	89
Table 8 – Overview of input parameters for all investigations of this study.	104
Table 9 – Prior distributions of the parameters in the STARS non–Newtonian foam model used for Bayesian estimation.	107
Table 10 – Non–Newtonian model parameters calibrated to fit the synthetic dataset #1.	110
Table 11 – Non–Newtonian model parameters calibrated to fit the synthetic dataset #2.	113

LIST OF ABBREVIATIONS

UQ	Uncertainty Quantification
SA	Sensitivity Analysis
QoI	Quantity of Interest
MC	Monte Carlo (method)
PCE	Polynomial Chaos Expansion
MCMC	Markov Chain Monte Carlo (method)
EOR	Enhanced oil recovery
WAG	Water-Alternated Gas
MRF	Mobility reduction factor
LE	Local equilibrium (state)
LQR	Low quality regime
HQR	High quality regime

LIST OF SYMBOLS

u, v	Scalar functions
\mathbf{u}, \mathbf{v}	Vectorial functions
nd	Number of spatial dimension
Ω	Physical domain
φ	Porosity
κ	Absolute permeability
δp or Δp	Pressure drop
S_α	Saturation of the α phase
ρ_α	Density of the α phase
\mathbf{q}_α	Flux vector of the α phase
λ_α	Mobility of the α phase
κ_α	Relative permeability of the α phase
μ_α	viscosity of the α phase
p_α	pressure of the α phase
f_α	Fractional flow of the α phase
Q_α	Flow rate of the α phase
κ_α^0	Endpoint relative permeability of the α phase
S_α^0	Saturation at endpoint relative permeability of the α phase
κ_α^0	Endpoint relative permeability of the α phase
N_α^0	Corey's [32] relative permeability exponent of the α phase
$\{A, L, B, M\}$	Chierici's [25] relative permeability coefficients
$\{L_\alpha, E_\alpha, T_\alpha\}$	LET [92] relative permeability coefficients
μ_{app}	Apparent viscosity
(f_g^*, μ_{app}^*)	Foam quality and apparent viscosity at the LQR–HQR transition regime
n_D	Normalized foam texture
(r_g, r_c)	Foam generation and destruction functions
n_D^{LE}	Foam texture at local equilibrium
(p_c^*, S_w^*)	Limiting capillary pressure and water saturation
$\mathcal{Y}, \mathcal{Y}^{PC}$	Model and PCE model approximation
$\mathbb{E}(\mathcal{Y}), \mathbb{V}(\mathcal{Y})$	Expected value and variance of the model \mathcal{Y}
S_i, S_{Ti}	Sobol sensitivity indices (main and total)

Contents

1	Introduction	18
1.1	Contextualization	18
1.2	Motivation	19
1.3	Oil recovery and enhanced oil recovery	20
1.3.1	Gas and foam injection	20
1.3.2	Historical review of foam assisted EOR	21
1.4	Uncertainty estimations in reservoir simulators	22
1.5	Objectives	25
1.5.1	Main objective	25
1.5.2	Specific objectives	25
1.6	Contributions of this work	26
1.7	Organization of the text	27
2	Mathematical models	28
2.1	Fundamental concepts	28
2.2	Two phase flow in porous media	30
2.3	The Buckley–Leverett equation	31
2.4	Relative permeability models	32
2.4.1	Evaluation of relative permeabilities	33
2.4.2	Corey’s model	34
2.4.3	Chierici’s model	34
2.4.4	LET model	34
2.5	Comparing the relative permeability models	35
2.6	Foam flow in porous media	37
2.6.1	Foam models	42
2.7	Comparing the LK and the CMG–STARS models	43
3	Uncertainty quantification and sensitivity analysis techniques	46
3.1	Uncertainty Quantification	46
3.2	Modeling of uncertainties in the system’s inputs	47
3.2.1	Estimating input uncertainties	48
<i>3.2.1.1</i>	Identifiability analysis	50
3.3	Propagation of uncertainties	51
3.4	Sensitivity Analysis	51
3.5	Emulators, surrogate models	52
3.5.1	Polynomial Chaos Expansion (PCE)	52
3.5.2	Accuracy of the surrogate model	54
3.6	Computing Sobol’ sensitivity indices	56

4	Uncertainty quantification and sensitivity analysis for relative permeability models	58
4.1	Introduction	58
4.2	Methods	60
4.2.1	Two-phase flow model	60
4.2.2	Relative permeability models	60
4.2.3	Datasets	61
4.2.4	Input Parameters and Quantities of Interest	62
4.2.5	Parameter and distribution estimation	63
4.2.6	Uncertainty quantification	64
4.2.7	Sensitivity analysis	65
4.2.8	Calibration of the surrogate model	65
4.2.9	Computational implementation	66
4.3	Results	67
4.3.1	Parameter estimation using MCMC	67
4.3.2	Surrogate model calibration	70
4.3.3	Forward uncertainty quantification	71
4.3.4	Sensitivity analysis	72
4.3.5	Effects of relative permeability endpoints	74
4.4	Discussion	75
4.5	Conclusions	77
5	Foam assisted water–gas flow parameters: from core–flood experiment to UQ and SA	78
5.1	Introduction	78
5.2	Foam displacement in porous media	80
5.2.1	Fluids and Rocks	80
5.2.2	Coreflood experiments	81
5.2.3	Mathematical models	83
5.2.4	STARS model	83
5.2.5	Linear kinetic model	84
5.3	Methods for uncertainty quantification and sensitivity analysis	84
5.3.1	Quantities of Interest	84
5.3.2	Parameter estimation and propagation of uncertainties	85
5.3.3	Sensitivity analysis	86
5.4	Results	86
5.4.1	Quality-scan experiment	86
5.4.2	Characterization of foam model parameters	87
5.4.3	Uncertainty propagation	90
5.4.4	Sensitivity analysis	92

5.5	Discussions	94
5.5.1	Experimental data and model discrepancy	95
5.5.2	Source of uncertainties	96
5.5.3	Comparing the two models	97
5.5.4	Limitations	98
5.6	Conclusions	98
6	Assessing uncertainties and identifiability of foam displacement models employing different objective functions for parameter estimation	100
6.1	Introduction	100
6.2	Methods	101
6.2.1	Foam displacement in porous media	101
6.2.2	Foam model	102
6.2.3	Datasets	103
6.2.4	Parameter estimation	105
6.2.5	Bayesian estimation	106
6.2.6	Identifiability analysis	107
6.2.7	Uncertainty quantification and sensitivity analysis	108
6.3	Results	108
6.3.1	Synthetic datasets	108
6.3.2	Experimental data from Kapetas <i>et al.</i> (2016)	113
6.3.3	Experimental data from Moradi–Araghi <i>et al.</i> (1997)	114
6.4	Discussion	116
6.4.1	Sensitivity analysis	117
6.5	Conclusions	117
7	Conclusions	119
7.1	Academic contributions	121
7.2	Future steps	122
	Bibliography	123

1 Introduction

This chapter describes this work’s general context, its motivations, a brief literature review, and the objectives pursued with this thesis.

1.1 Contextualization

The pre-salt reservoir is a new kind of deepwater reservoir (i.e., deepness beyond 400 *m*), discovered in 2006 during exploration and drilling operations conducted by Petrobras. The pre-salt belongs to the Atlantic continental shelf under a 2 *km* layer of salt. The pre-salt extended the level of oil production to a new level, and it remains under exploration. The extraction locations are depicted in Figure 1 showing the proximity between the wells and the Brazilian coast.

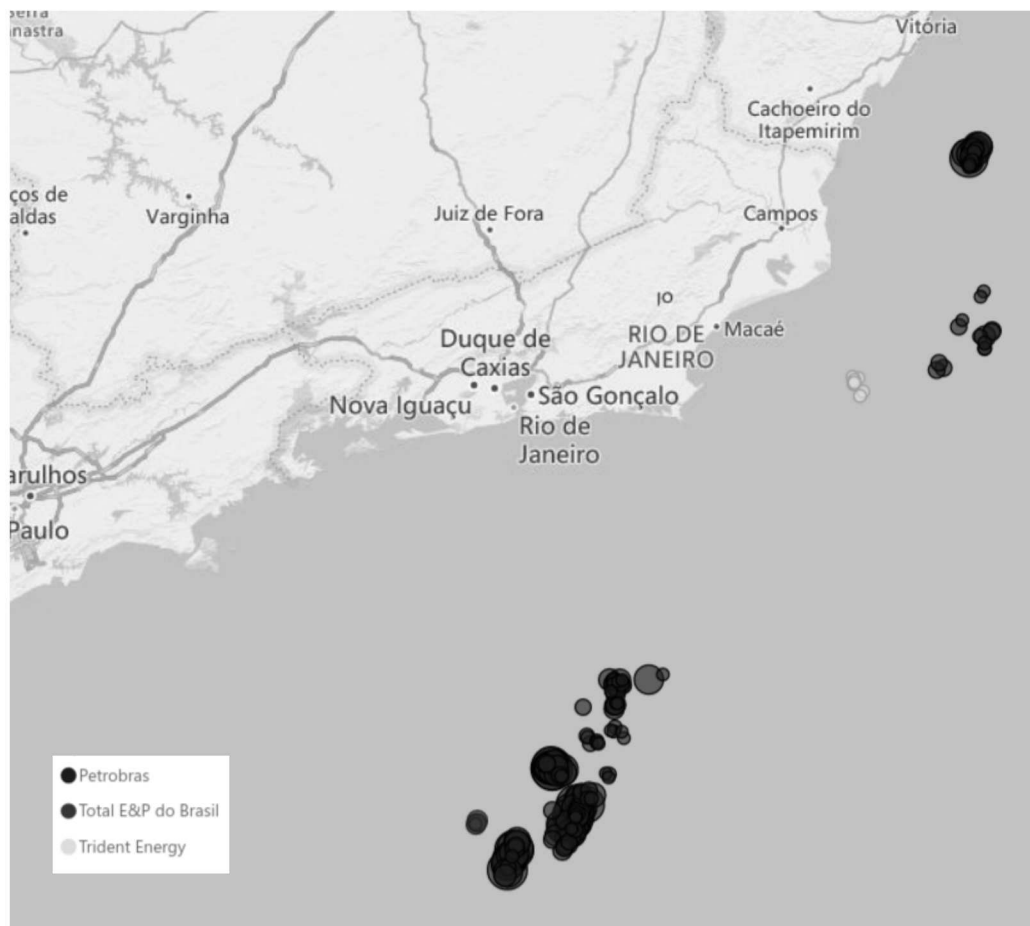


Figure 1 – Detail of production wells in the pre-salt since 2006, adapted from [111].

At present, the pre-salt reservoir has been explored only in a small proportion compared to its full extension. Within the first ten years of production, the operative oil & gas companies extracted in 2017 the record of 1.5 million oil barrels per day. In 2018, the pre-salt contained just 83 extraction locations, returning an average production rate

of 17 thousand oil barrels per day. Figure 1 shows the location of the active production wells reported by September 2020.

In December 2017, the Brazilian reserves of oil and gas were proven to be 12.8 billion barrels of oil and 363 billion cubic meters of gas. The pre-salt contains more than half of such reserves (56% of the total oil, and 53% of the estimated gas [110]). The remainder of fossil reserves is distributed within other "traditional" offshore operative wells and continental extraction wells. The potential of offshore activities has dominated investments since the very beginning of such operations [122]. The immediate future of oil and gas extraction in Brazil reflects a trend to avoid investments in continental reservoirs, increasing the financial resources destined for offshore production wells. ANP [110] released the predictions for a short term period contemplating until 2024, these trends are depicted in Figure 2.

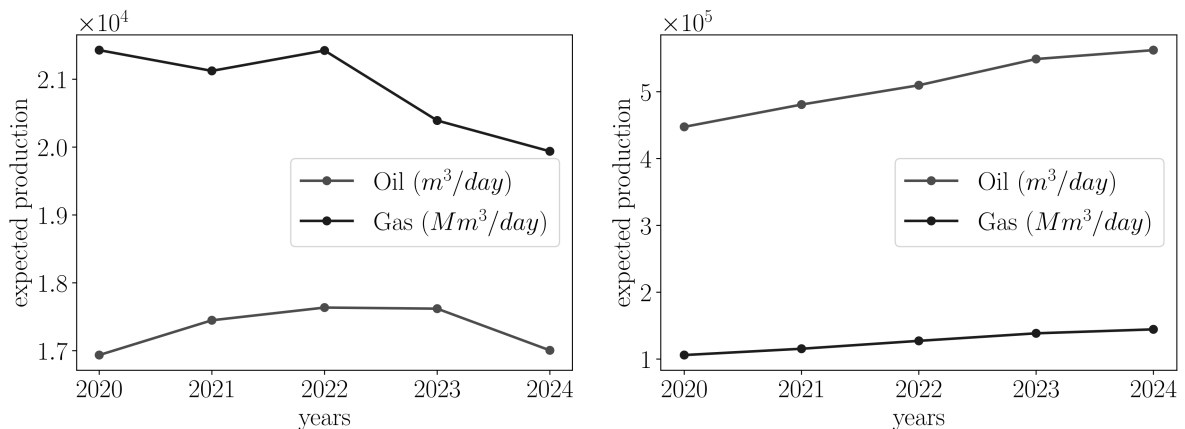


Figure 2 – ANP short term expectation of produced oil and gas considering continental activities (left) and offshore reservoirs operations (right), adapted from [110].

1.2 Motivation

As discussed in [6] EOR activities are often conditioned to the following main threats (i) reducing the complexity from the physical extraction process to deal with laboratory scale solvable problems. Such simplifications are responsible for distorted synthetic reservoir responses. (ii) Controversial choices of laboratory scale samples to generalize the physical behavior, even considering pilot tests. In silico evaluations are excellent techniques to extend the experimental evidence obtained from laboratory scale samples. However, the validity of such simulations is constrained to the degree of representation that the core sample provides towards the pilot test scale experiment. (iii) Eventual variations in the EOR project execution may affect the performance of the technique. EOR projects do not differ from other engineering projects; they become less attractive when the invested resources are higher than the benefits obtained.

1.3 Oil recovery and enhanced oil recovery

The removal of oil from a reservoir can be divided into different stages. Initially, when the reservoir is perforated, the pressure difference between the fracture and the reservoir mobilizes the oil. This stage is known as primary recovery. However, the pressure drop that mobilizes the oil in the reservoir decreases as being extracted. Other techniques, such as water injection, gas, and other fluids, can continue the extraction. The stage that corresponds to the injection of fluids to maintain the flowing pressure is secondary recovery. At a certain point, the oil recovery ceases, and advanced techniques are used to extract the remaining oil from the reservoir. This stage is known as tertiary recovery. In terms of extracted oil, the primary recovery corresponds to only $\sim 10\%$ of the removable oil, while the secondary recovery corresponds to $\sim 30\%$ of the removable oil [84]. The remaining oil is supposed to be extracted with enhanced oil recovery (EOR) techniques, usually associated with the tertiary oil recovery stage. EOR has been defined [6] as *injection of a fluid, with or without additives, to the reservoir, to displace oil while changing the oil and interfacial properties and providing extra pressure at the secondary, tertiary, or even primary stage.*

EOR methods may involve the injection of fluids (liquids or gases), chemicals, and energy transport (for example, thermal energy). The injection of fluids aims to remove oil from the reservoir by generating a (shock) front with the remaining oil. Usually, the injected gases are carbon dioxide, nitrogen. Similarly, chemical substances like polymers, surfactants, and hydrocarbon solvents are used to remove the oil from reservoirs. In the same way, energy can be injected into the reservoir as heat. In general, EOR techniques inject an external agent to the reservoir to create favorable conditions to remove oil, like reduce the interfacial tension with the oil, alter the reservoir's wettability, modify the oil's viscosity, among others.

1.3.1 Gas and foam injection

Injection of fluids into the reservoir contemplates oil recovery improvement, creating suitable conditions to displace the oil. However, the effects of displacing oil injecting continuous slugs of one fluid meet the efficiency break point when the production well receives the injected fluid. To further extend the efficiency of the fluid injection, the continuous slug should be interrupted with alternatives like water alternated gas (WAG) schemes to perform this injection swap.

The sweep efficiency of (in-) miscible schemes may be hampered by the formation of viscous fingers as proved mathematically by Saffman & Taylor [118], and experimentally by Tabeling *et al.* [132], as well as Woods [141]. The Saffman–Taylor instability occurs when the injected fluid has less viscosity than the resident fluid. Recently, numerical studies such as the works of Jha *et al.* [70], Yazdi & Norouzi [146], and Abdul & Muggeridge [1]

corroborated the negative effects of viscous fingers in oil recovery. In particular, Abdul & Muggeridge [1] studied the dynamics of viscous fingers, analyzing their evolution to provide a prior-estimate to avoid the formation of fingers.

Moreover, WAG projects can have their efficiency reduced by buoyancy effects (also known as gravity override), where the less dense fluid (often the gas) attempts to flow through the higher layers of the reservoir. Furthermore, channeling is caused by the heterogeneities of the reservoir, as reported by [133, 62]. Examples of heterogeneities are fractures and preferential paths. Figure 3 shows the effects of a preferential path, altering the bulk streamflow.

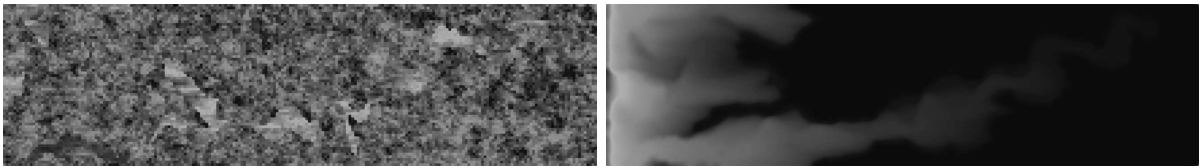


Figure 3 – Absolute permeability field for the 36th layer of the SPE10 project (left) and simulation results of water saturation in a gas flooding experiment (right). (adapted from [34]).

1.3.2 Historical review of foam assisted EOR

WAG oil recovery projects benefit from the foam dynamics properties, Albrecht *et al.* [2] reported two main advantageous features like delay the gas flow and block the gas flow. Initially, [2] presented experimental shreds of evidence on unconsolidated sand-packs and sandstones revealing excellent capabilities to seal gas leaks in a reservoir. In particular [2], suggests the use of foam process in the sealing of natural gas reservoirs. The experimental evidence belongs to core samples with permeabilities varying from 3 to 16 Darcy, including in some cases fractures. In these harsh scenarios, the author claims to achieve the blocking of the gas phase.

In the mid '80s [64, 41, 42] presented valuable contributions accepted until our days on the modeling of foam dynamics at pore-scale. These articles and others used arrays of capillary tubes to mimic the flow through a pore throat and pore networks. Hirasaki & Lawson [64] proposed a mathematical model to explain the effects of foam dynamics on the viscosity of the gas phase. Falls *et al.* [41] extended the model presented in [64], adding new mechanisms to generate new bubbles. In terms of mathematical models, the mechanisms to generate foam bubbles were incorporated, adding a population balance partial differential equation, yielding a more complex model, but gaining a modeling technique to evaluate transient aspects of foam dynamics. Experimentally this was achieved, including capillary tubes with bifurcations. Falls *et al.* [42] generalized the findings reported in [64, 41] with an experimental setup that consisted of a capillary flow including a regular array of obstacles that altered the streamflow. The models were validated with experimental observations,

and their relevance remains valid until the present day. In addition to this, the three articles exposed modifications exclusively on the gas viscosity.

The contributions from Heller & Kuntamukkula [61], Khatib *et al.* [82], as well as Hanssen [57, 58] were focused on relate the microfluidic findings from [64, 41, 42] to Darcy’s-scale properties. Pore scale and Darcy’s scale models including their experimental validation suggest that the collapse of foam bubbles is achieved at pore scale when the critical disjoining pressure is achieved; whereas at Darcy’ scale when the system meets the critical capillary pressure. At Darcy’s scale, the massive collapse of foam bubbles was corroborated experimentally by Osterloh & Jante [109] and Alvarez *et al.* [3], clearly recognizing two flowing regimes low-quality regime (LQR) featuring stable and wet foam, and high-quality regime (HQR) presenting unstable and dry foams.

On a different take, Hirasaki *et al.* [65] documented the results of a pilot test involving a contaminated aquifer, where the contaminant was segregated to the lower layers of the reservoir. Foam processes were applied to mobilize the contaminated water, diverting surfactants to the lower permeability regions, showing promising performances. The aquifer had permeability regions varying from 10 to 100 Darcy. The injection well had 6 meters long, and three extraction wells were located on a radial basis, separated each from the other 3.7 meters. Extraordinary responses were evidenced, taking into account that the reservoir was located 47 meters under the surface level. This work was confirmed by Portois *et al.* [113], where the authors explored the sealing capabilities of foam assisted soil remediation.

In 2019, Katiyar *et al.* [81] reported outstanding results in a pilot test project involving foam-assisted EOR. The authors screened at least 11 commercial surfactants subjected to harsh conditions (120⁰C, 3.23% salinity, and $\sim 27\%$ of Clay). The chosen surfactant was additionally tested against rock adsorption, ensuring economic viability. The pilot test consisted of a single horizontal well surrounded by two production wells. The baseline operation was composed of the co-injection of water and gas at constant fractional flow and flow rate. Within five weeks of surfactant injection, the oil recovery exceeded the baseline configuration in more than 2000 oil barrels. The oil recovery trend was increasing monotonically during six weeks.

1.4 Uncertainty estimations in reservoir simulators

Reservoir simulators combine mathematical models with engineering expertise to assess the reservoir’s behavior considering particular geological settings and production conditions. Considering simulators as black-box processes that receive specific inputs and return a set of outputs, this work analyzes the effects of uncertainties on the simulations. Uncertainties usually have origin from two factors [100]: (i) the adopted model and (ii) the quality of the data used to calibrate the model. This work will explore these uncertainties

and how they can affect predictions of two-phase flow models, focusing on foam flow for EOR.

Laboratory experiments, and often field data, are commonly used to calibrate the parameters of the mathematical models behind reservoir simulators. In particular, the acquisition of accurate relative permeabilities data is critical and has been of interest in the petroleum industry and scientific community [101]. The inherent difficulty to experimentally determine relative permeabilities have been extensively reported in the literature [101, 14, 124]. Laboratory experiments to obtain relative permeabilities are complicated and time consuming [124]. Three methods are commonly used for measuring the relative permeability data: unsteady-state, steady-state, and centrifuge. These methods are discussed in terms of their disadvantages and limitations in [14]. The authors highlight the fact that these data are subject to errors and uncertainties. The errors in relative permeabilities estimated from displacement experiments under different operating conditions using the Johnson, Bossler, and Naumann (JBN) method [71] were studied in [134, 135]. Their results indicate that errors were in the range of 0.2% to 15%.

In most cases, errors were below 5%, except near the residual water saturation, where they were notoriously higher. Also, the relative permeabilities are functions of the phase saturations and are affected by several other parameters that may contain uncertainties as well [67]. Figure 4, exposes the consequences of uncertainty propagation in a simulator based on the Buckley–Leverett Equation, following the structure developed by Tao & Watson [134, 135].

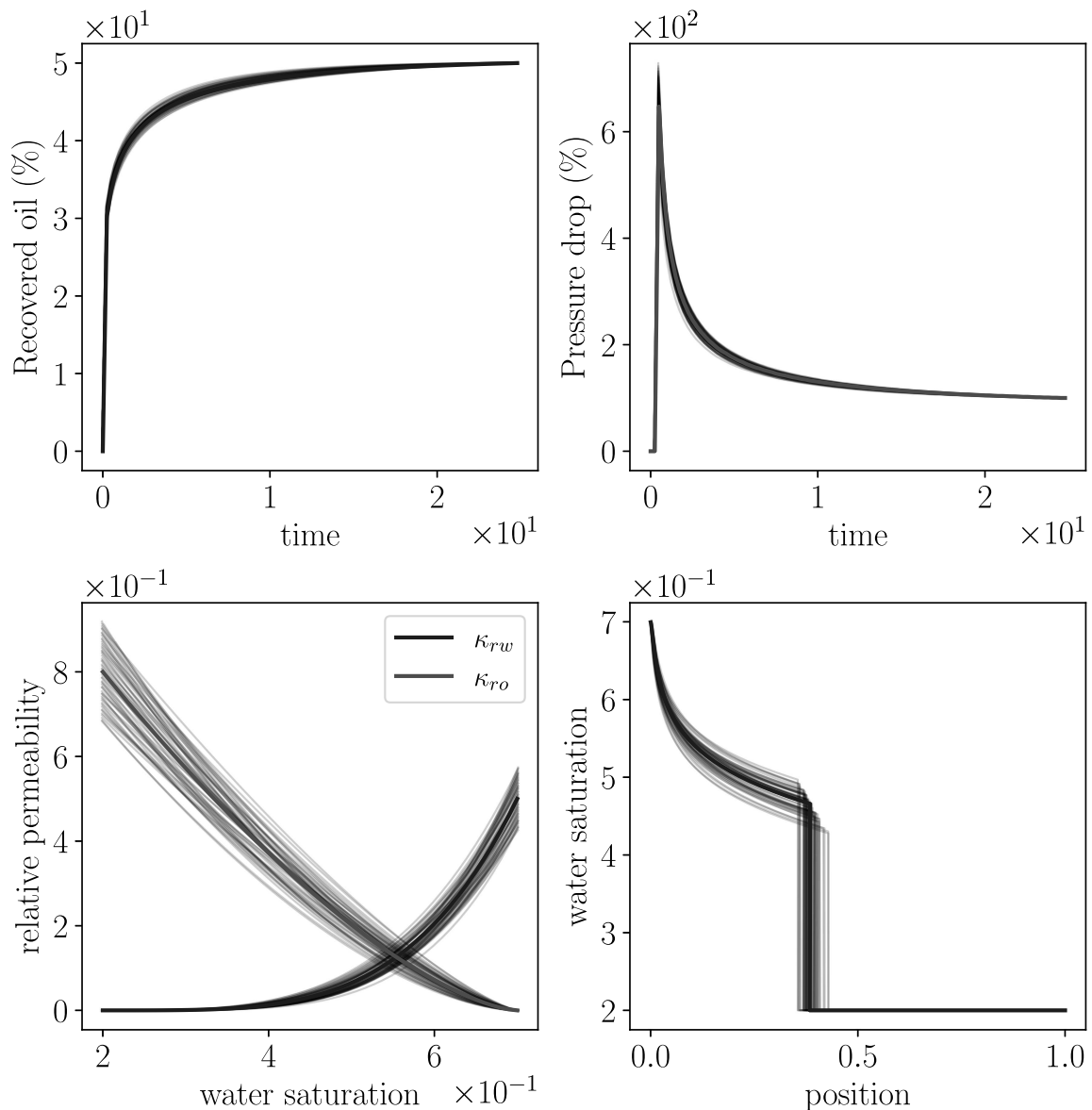


Figure 4 – Interpretation of the posterior error–estimation workflow proposed in [134, 135]. Gray lines represent different model’s evaluations, whereas color lines represent the (deterministic) "best fit" solution.

Similar findings were reported by Berg *et al.* [8, 9], where the authors exposed how experimental uncertainties affect the uniqueness of the model calibration; considering two different relative permeability models.

Concerning foam flow for EOR, experimental studies have been explored quite successfully in the literature [62]. Foam quality–scan and flow–rate–scan experiments are usually employed to assess foam properties for calibrating the parameters of computational models [148]. In the flow quality–scan experiment, the total flow rate is constant, while the pressure drop in the core sample is measured as a function of foam quality (i.e. gas

fractional flow). In the flow-rate-scan, the foam quality is fixed, while the flow rate is varied. In this context, physical modeling of the foam flow in porous media [5, 74, 23, 149] is challenging due to its non-Newtonian nature, its dependence on the foam texture, and the complex bubble generation/coalescence process. Consequently, model calibration is not straightforward, and the role of uncertainties in the estimated parameters remains unexplored [12, 95, 98, 148].

The methods commonly used for parameter estimation of foam flow models neglect the inherent uncertainty due to technical limitations or measurement errors present in experimental data. In addition, model discrepancy, i.e., the mismatch between model and experiment, and the correlation between the parameters are also overlooked. The uncertainties in the experimental data and the model discrepancy should be considered to assess the mathematical model's reliability.

1.5 Objectives

This thesis focuses on two goals, firstly the calibration of different two-phase models used in reservoir simulators taking into account experimental data and its variability. And secondly, study how the uncertainty is propagated from the model's input parameters to the reservoir simulator's outputs. In particular, this thesis aims to shed light on foam-assisted EOR projects and different problems related to two-phase flow in porous media. The objectives pursued here are listed as follows.

1.5.1 Main objective

Analyze how experimental uncertainty impacts the predictions of different models used in two-phase reservoir simulators, in particular those related to foam-based EOR.

1.5.2 Specific objectives

To accomplish the main objective of this work, the following specific objectives are listed:

- Tailor a robust computational framework designed for two-phase flow in porous media to conduct model inversion considering measurement errors in the experimental data.
- Recognize model's identifiability issues to determine which parameters challenge model calibration and increase model uncertainty.
- Perform uncertainty quantification (UQ) studies to determine the reliability of the analyzed model's predictions.

- Execute global sensitivity analysis (SA) based on variance to identify key parameters for model calibration and uncertainty quantification.
- Investigate the impact of different objective functions and experimental data in parameter estimation and uncertainty quantification processes.

An overview of the framework and techniques considered in this work is presented in Figure 5 to tackle uncertainty in two-phase foam displacement models. The framework relies on experimental data and a mathematical model. The inverse UQ problem is solved by combining the efforts of identifiability analysis with Bayesian inference. Depending on the size and complexity of the problem, emulators or simulators are used to propagate the parametric uncertainty through the mathematical models, solving the forward UQ problem. Later the variability of the analyzed QoI is plausible to be reduced by identifying relevant input parameters. Here a global sensitivity analysis is conducted using the Sobol indices. By the end of these operations, we can improve the reliability of the model's prediction.

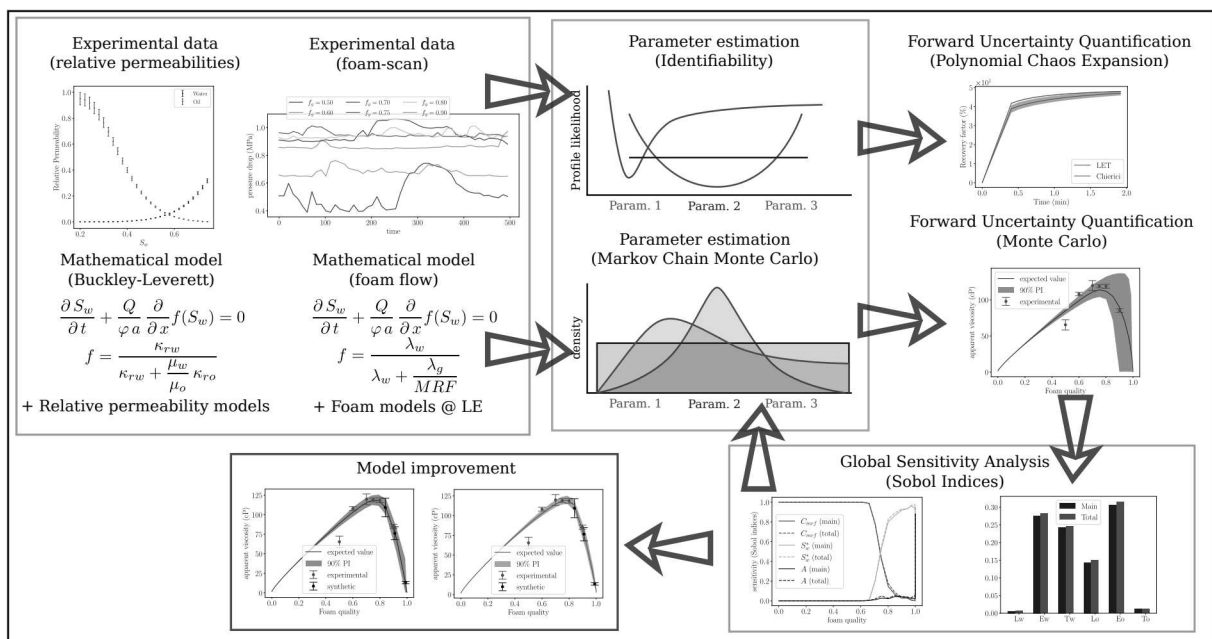


Figure 5 – Framework to perform inverse-forward uncertainty quantification and sensitivity analysis.

1.6 Contributions of this work

The studies and results presented in this thesis aim to shed light on practical aspects related to two-phase reservoir simulations, model validation, and decision making. Assessing the reliability of a specific model establishes the appropriate environment to decide if the model is a good or lousy approximation for a given experimental observation.

In addition to this, the reliability analysis will expose the variability of a model in many other different scenarios. We show efforts towards analyzing uncertainties arising from (i) oil–water displacement satisfying the Buckley-Leverett equation, where solutions were computed using the fractional flow theory. (ii) calibration of two different foam models (where one is used in the industry). Furthermore, (iii) the effects of the adjustment (objective) function to obtain more reliable calibration results for a foam model used in the industry. Each of these research efforts were compiled into the following research articles.

- Uncertainty quantification and sensitivity analysis for relative permeability models of two-phase flow in porous media. *Journal of Petroleum Science and Engineering*, 2020. doi: 10.1016/j.petrol.2020.107297.
- Foam assisted water-gas flow parameters: from core-flood experiment to uncertainty quantification and sensitivity analysis. *Transport in Porous Media*, 2021. doi: 10.1007/s11242-021-01550-0
- Assessing uncertainties and identifiability of foam displacement models employing different objective functions for parameter estimation. *in preparation*.

1.7 Organization of the text

The remaining chapters of this thesis are organized as follows. Chapter 2 presents the mathematical modeling techniques used to study the displacement of two phases in a porous medium. Particular focus is given to the Buckley-Leverett equation and the analysis of different models to study the displacement of foam in a porous medium. Then, Chapter 3 introduces the methods used for uncertainty quantification and sensitivity analysis. Next, the Chapters 4, 5, and 6 presents the results obtained so far in this work, where three peer–reviewed articles are included. Finally, Chapter 7 presents the conclusions of this work, discussions exposing the limitations of our study. Future research lines are also suggested in this chapter.

2 Mathematical models

2.1 Fundamental concepts

This work focuses on modeling the scenario where a fluid is injected into a porous medium to remove other resident fluid from the domain. The removal of the resident fluid or phase can be divided into two different stages. The initial stages correspond to the period where the injected fluid did not reach the production well, while at a later stage, the injected fluid reaches the production well. Figure 6 shows three different schematic representations to describe the removal of a resident fluid by injecting another fluid. In particular Figures (6 (a)) and (6 (b)) are equivalent qualitative scenarios, where the injected fluid did not reach the outlet of the porous medium. Nevertheless, Figure (6 (c)) shows that at the outlet, the product contains a mixture of both fluids (resident and injected).

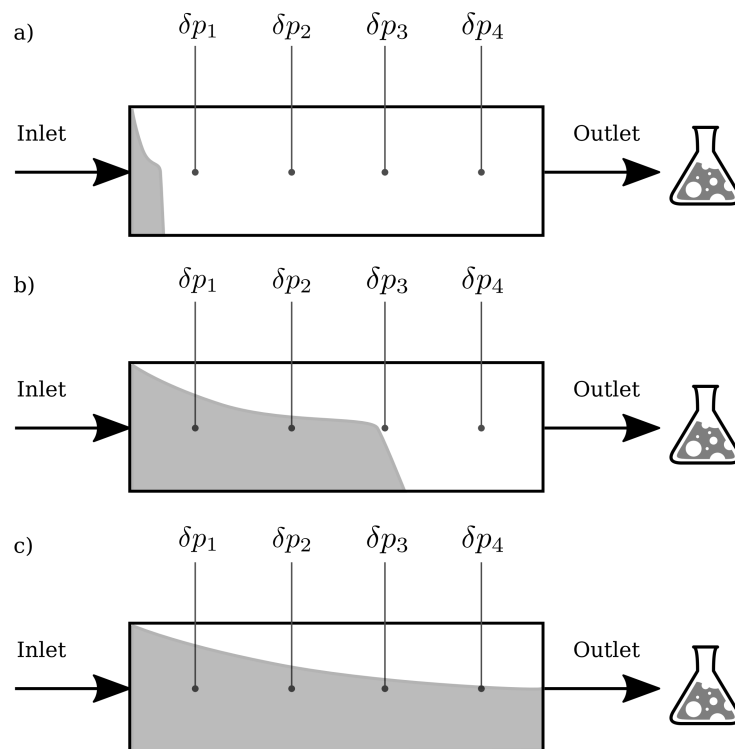


Figure 6 – Schematic representation of the removal of a fluid from a porous domain with the injection of a different fluid.

The diagram represented before shows devices to measure the pressure drop at different positions of the domain and devices to measure the fluids obtained at the outlet. Figure 7 shows typical curves for the accumulated (removed) fluid and the pressure drop recorded during the execution of the experiment. Figure 7 distinguishes the regime where the injected fluid did not meet the production well and when the injected fluid reached the production well.

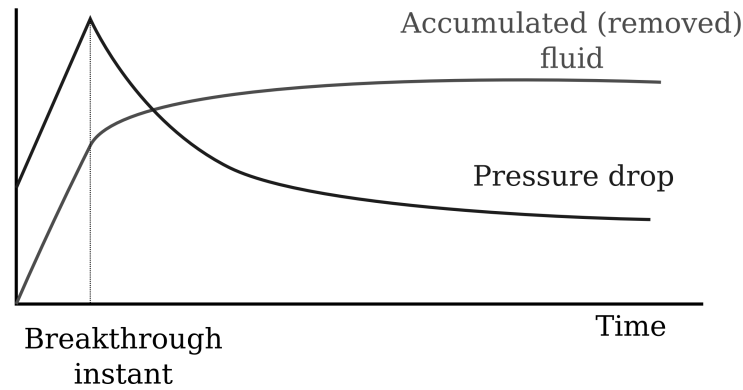


Figure 7 – Measurement of removed fluid from the porous domain and assessment of the pressure drops δp during the experiment.

Different factors can affect the performance of the fluid's removal. In Figure 7 it is possible to recognize that after the breakthrough time, the accumulated (removed) fluid reaches a stagnation state. It does not matter how much fluid is injected; the accumulated (removed) fluid will not increase considerably. Typically, the removal of the fluid can face two situations (see Figure 8): (a) stable piston-like displacement, and (c) unstable displacement. The concept of stability is linked to the formation of different shock fronts that affects the shape of the fluid's interface, as proved by Saffmann & Taylor [118] and commented by Langtangen *et al.* [85], Tripathi & Mohanty [136], and Chorin [28].

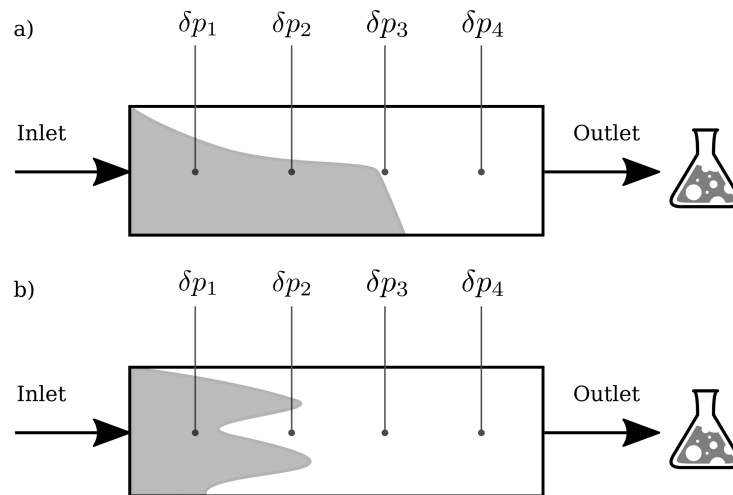


Figure 8 – Comparison of different kind of interfaces recognized in the displacement of immiscible fluids in a porous medium.

Next, the mathematical formulation of a two-phase flow problem in a porous domain is described. We start with some essential definitions and then extend the single-phase Darcy's law to more flowing phases. Two problems are presented: (i) the Buckley–Leverett equation [19], and (ii) mathematical models that take into account the effects of foam in the water–gas flow.

2.2 Two phase flow in porous media

To model the flow of two species in a porous medium, we start recalling some definitions. The porosity is defined as the ratio of the porous domain Ω that is occupied by void space. It is represented by:

$$\varphi = \frac{V_{porous}}{V},$$

where V is the total volume and V_{porous} is the volume of the void space. The absolute permeability $\boldsymbol{\kappa}$ describes the resistance that the porous medium offers to the flowing fluids, and it is usually measured in Darcy D (or mili-Darcy mD) or surface units m^2 . The saturation S_α of any phase α is defined as the fraction of the pore volume occupied by the α phase. In general, the saturation S_α is given by:

$$S_\alpha = \frac{V_\alpha}{V_{porous}},$$

where V_α is the volume occupied the the α phase.

The equations describing two-phase flow in porous media are obtained from the principle of mass conservation of each phase [7]. Considering the porous domain $\Omega \subseteq \mathbb{R}^{nd}$, where nd is the number of spatial dimensions, the mass balance of the α phase is given by:

$$\frac{\partial(\varphi S_\alpha \rho_\alpha)}{\partial t} + \text{div}(\rho_\alpha \mathbf{q}_\alpha) = 0, \quad \text{in } \Omega \times [0, T], \quad (2.1)$$

where \mathbf{q}_α is the flux vector of the α phase. Assuming that the flowing phases have no mass transfer between them and that the interface remains chemically inertial, each phase's composition remains constant during the entire modeling time. The flux vector is derived from Darcy's law for a single phase [105, 140], and can be written as:

$$\mathbf{q}_\alpha = -\boldsymbol{\kappa} \lambda_\alpha (\nabla p_\alpha + \rho_\alpha \mathbf{g} \nabla z), \quad \text{in } \Omega \times [0, T], \quad (2.2)$$

where the term $\rho_\alpha \mathbf{g} \nabla z$ represents buoyancy effects, ∇p_α is the pressure gradient of the phase, and λ_α is the mobility of the α phase. The phase mobility λ_α is defined in terms of the relative permeability of the phase ($\kappa_{r\alpha}$) and viscosity (μ_α) as:

$$\lambda_\alpha = \frac{\kappa_{r\alpha}}{\mu_\alpha}. \quad (2.3)$$

Considering that the porous medium is fully saturated ($\sum_\alpha S_\alpha = 1$), the porous domain is rigid, and assuming the phases are incompressible, Equation (2.1) can be rewritten as:

$$\varphi \frac{\partial S_\alpha}{\partial t} + \text{div}(-\boldsymbol{\kappa} \lambda_\alpha (\nabla p_\alpha + \mathbf{g} \nabla z)) = 0, \quad \text{in } \Omega \times [0, T]. \quad (2.4)$$

To obtain solutions for the Equation (2.4) boundary conditions and initial values must be declared.

2.3 The Buckley–Leverett equation

The mass balance equation written in Equation (2.4) represents the conservation of each phase. The conservation of the total mass can be obtained by adding both components of Equation (2.4). For simplicity, here, the phases are denoted with w and n , describing the wetting phase and non-wetting phase, respectively. Neglecting buoyancy effects the following equation is obtained for the total mass conservation:

$$\varphi \left(\frac{\partial S_w}{\partial t} + \frac{\partial S_n}{\partial t} \right) + \operatorname{div}(-\kappa \lambda_w \nabla p_w - \kappa \lambda_n \nabla p_n) = 0, \quad \text{in } \Omega \times [0, T]. \quad (2.5)$$

The first term (transient) is zero, since $S_w + S_n = 1$. Capillary effects are introduced as the difference between the phases pressure, $p_c = p_w - p_n$, therein it is possible to write the mass balance in terms of p_w and p_c as:

$$\operatorname{div}(-\kappa \lambda_w \nabla p_w - \kappa \lambda_n \nabla p_w + \kappa \lambda_n \nabla p_c) = 0, \quad \text{in } \Omega \times [0, T]. \quad (2.6)$$

In particular assuming that p_c is constant in $\Omega \times [0, T]$, the total mass balance is re-arranged:

$$\operatorname{div}(-\kappa \lambda_w \nabla p_w - \kappa \lambda_n \nabla p_w) = 0, \quad \text{in } \Omega \times [0, T]. \quad (2.7)$$

The total mobility λ_T is defined as $\lambda_T = \lambda_w + \lambda_n$. Consequently, the total mass balance results in:

$$\operatorname{div}(-\kappa \lambda_T \nabla p_w) = 0, \quad \text{in } \Omega \times [0, T]. \quad (2.8)$$

The vector resultant from the operation $-\kappa \lambda_T \nabla p_w$ is the total Darcy's velocity \mathbf{u} . It is common to write the phase balance in terms of the total flux vector; this is possible defining the *fractional flow* (f_w) as the ratio:

$$f_w = \frac{\lambda_w}{\lambda_T} = \frac{\kappa_{rw}}{\kappa_{rw} + \left(\frac{\mu_w}{\mu_n} \right) \kappa_{rn}}, \quad (2.9)$$

consequently, the conservation of the wetting phase reads the following expression:

$$\varphi \frac{\partial S_w}{\partial t} + \operatorname{div}(\mathbf{u} f_w) = 0, \quad \text{in } \Omega \times [0, T]. \quad (2.10)$$

For a one-dimensional flow $\Omega = [0, L]$, where L is the length of the domain, the conservation of the wetting phase reads the next expression:

$$\varphi \frac{\partial S_w}{\partial t} + \frac{\partial}{\partial x} (u f_w) = 0, \quad \text{in } [0, L] \times [0, T]. \quad (2.11)$$

Assuming the relation flux-velocity $Q = u a$, where a is the cross-section of the porous domain, the conservation of the mass for the wetting phase relies on the so-called Buckley–Leverett [19] equation:

$$\frac{\partial S_w}{\partial t} + \frac{Q}{\varphi a} \frac{\partial}{\partial x} (f_w) = 0, \quad \text{in } [0, L] \times [0, T]. \quad (2.12)$$

The Buckley–Leverett equation is solved supplying boundary conditions (for example fixing $S_w(0, t)$) and initial values (for example fixing $S_w(x, 0)$). Within this context, semi-analytic solutions are obtained for Equation (2.12) employing the method of characteristics following Marle [99] and Welge [139]. To illustrate the method of characteristics, the total differential for a fixed wetting phase saturation $S_w(x, t) = S$ is:

$$d S_w = \frac{\partial S_w}{\partial t} dt + \frac{\partial S_w}{\partial x} dx = 0. \quad (2.13)$$

Isolating $\frac{\partial S_w}{\partial t}$ and replacing in (2.12) the following expression is obtained:

$$-\frac{\partial S_w}{\partial x} \left(\frac{dx}{dt} \right)_{S_w=S} + \frac{Q}{\varphi a} \frac{\partial}{\partial x} (f_w) = 0, \quad \text{in } [0, L] \times [0, T]. \quad (2.14)$$

In particular, assuming that the fractional flow depends only on the wetting saturation $f_w = f_w(S_w)$, the next identity can be recognized:

$$\left(\frac{dx}{dt} \right)_{S_w=S} = \frac{Q}{\varphi a} \frac{df_w}{dS_w}, \quad (2.15)$$

which means that any wetting saturation $S_w = S$ takes initial and boundary data and transports them through the x -axis with speed given by $\frac{Q}{\varphi a} \frac{df_w}{dS_w}$. This speed is often called characteristic speed. Further readings concerning the method of characteristics can be found on Marle [99] and Welge [139].

2.4 Relative permeability models

Supported by experimental evidence, Darcy's law [33] relates the pressure gradient with the velocity of a single flowing phase. The extension to many flowing phases demanded nearly 80 years, until Muskat & Meres [105] proposed Equation (2.2) modeling the experimental observations reported in the works of Wyckoff *et al.* [143] and Wyckoff & Botset [142]. Wyckoff & Botset [142] compiled a vast collection of experimental evidence employing different combinations of gas and oil using unconsolidated sand; the authors introduced the concept of "experimental" relative permeabilities. Similarly, Leverett [89] presented results for displacements of water and oil considering unconsolidated sands. The work of Leverett [87] presents the functional relation between capillary pressures and wetting phase saturation. In the same article, Leverett introduces a new non-dimensional relation named after him as J-Leverett function. Finally, Leverett [87] corroborates that the extension of Darcy's law to more flowing phases showing a similar conclusion as the done by Muskat & Meres [105]. In Leverett & Lewis [88] the authors show experimental observations to certify the displacement of oil-water-gas considering steady-state and unconsolidated sands.

2.4.1 Evaluation of relative permeabilities

In Burdine [20], the author expresses the flowing rate of the wetting and non-wetting phases employing the Poiseuille law for a collection of tubes with radii between r and $r + dr$ analyzing $f(r) dr$ tubes, yielding the next expressions:

$$Q_w = -\frac{\pi \nabla p}{8 \mu_w} \int_{r_{min}}^r r^4 f(r) dr, \quad Q_n = -\frac{\pi \nabla p}{8 \mu_n} \int_r^{r_{max}} r^4 f(r) dr. \quad (2.16)$$

The wetting phase covers the smallest tubes, and the non-wetting phase flows through the largest tubes. Relative permeabilities are defined normalizing the fourth-order moments, yielding the following expressions

$$\kappa_w = \frac{\int_{r_{min}}^r r^4 f(r) dr}{\int_{r_{min}}^{r_{max}} r^4 f(r) dr}, \quad \kappa_n = \frac{\int_r^{r_{max}} r^4 f(r) dr}{\int_{r_{min}}^{r_{max}} r^4 f(r) dr}. \quad (2.17)$$

The pore size distribution for this particular case is defined as follows [11],

$$G(r) = \frac{r^3 f(r)}{\int_{r_{min}}^{r_{max}} r^4 f(r) dr}, \quad (2.18)$$

and it is related to the capillary pressure through the next relation [11, 7],

$$G(r) = -p_c \frac{dS_w}{dp_c}, \quad (2.19)$$

where p_c is a function of the tube's radius $p_c = 2 \sigma \cos \theta r^{-1}$, σ is the surface tension between the flowing phases, and θ is the wettability contact angle. After some algebra, Burdine [20] reaches the next expressions that links relative permeabilities with capillary pressures,

$$\kappa_w = \frac{\int_{\min S_w}^{S_w} p_c^{-2} dS_w}{\int_{\min S_w}^{\max S_w} p_c^{-2} dS_w}, \quad \kappa_n = \frac{\int_{S_w}^{\max S_w} p_c^{-2} dS_w}{\int_{\min S_w}^{\max S_w} p_c^{-2} dS_w}. \quad (2.20)$$

The previous expressions are often known as Burdine's relative permeability equations.

Different authors proposed models to relate the capillary pressure with the wetting phase saturation, such as Gardner's model [50] where the author proposes two models, a rational and an exponential expression. Childs and Collis-George [27], Irmay [69] and Corey [32] proposed polynomial equations to relate the wetting phase saturation with the relative permeabilities. In particular Brooks & Corey [16] extended Corey's model [32] adding physical parameters in the mapping of capillary pressure and water saturation. Within this framework, it is possible to write relative permeabilities as functions of the wetting phase saturation.

In general, polynomial approaches for relative permeability, like the Corey's model [32], presents limitations to capture changes on curvature near the endpoint

saturations. Some models were proposed to overcome these limitations. In particular, Chierici [25] proposed an exponential model, whereas Lomeland *et al.* [92] proposed a rational model, known as the LET model. Both models (Chierici's and LET) also depend exclusively on the saturation of the wetting phase. In particular, any of these models show dependencies with the relative permeability endpoints (S_{w0}, κ_w^0) and (S_{n0}, κ_n^0) . This work will use and compare the following models: Corey, Chierici, and LET.

2.4.2 Corey's model

Corey's relative permeability model [32] remains one of the most used models due to its simplicity. It depends on four physical parameters and two empirical parameters without physical meaning. These non-physical parameters are adjusted using experimental data. Corey's model is given by:

$$\kappa_{rw} = \kappa_w^0 (S_{we})^{N_w}, \quad \kappa_{rn} = \kappa_n^0 (1.0 - S_{we})^{N_n}, \quad (2.21)$$

where N_w and N_n are Corey's exponents (real numbers to be determined), κ_w^0 , and κ_n^0 are the relative permeabilities at endpoints for wetting and non-wetting phases, respectively. Here S_{we} refers to the mobile saturation defined as a function that depends on the endpoints saturations, (S_{w0} for wetting and S_{n0} for non-wetting phase), yielding the following expression:

$$S_{we} = \frac{S_w - S_{w0}}{1 - S_{w0} - S_{n0}}. \quad (2.22)$$

2.4.3 Chierici's model

Chierici's model [25] consists of two exponential equations. The number of parameters that need to be determined (or adjusted to experimental data) is two for each phase. The model has better performance than Corey's model [32] and other polynomial approaches, especially near the saturation endpoints and in the presence of experimental data points showing curvature changes. Chierici's model yields the following expression:

$$\kappa_{rw} = \kappa_w^0 \exp(-B S_{wt}^{-M}), \quad \kappa_{rn} = \kappa_n^0 \exp(-A S_{wt}^L), \quad S_{wt} = \frac{S_w - S_{w0}}{1 - S_w - S_{n0}}, \quad (2.23)$$

where A , L , B and M are the parameters of the model.

2.4.4 LET model

The LET model was proposed by Lomeland, Ebeltoft, and Thomas [92]. The primary capability, when compared to Corey's model [32] and Chierici's model [25], is the flexibility to capture relative permeability points showing substantial curvature changes (S-shaped). The number of parameters to be determined employing the LET model is

three for each phase. The LET model is represented with the following rational expression:

$$\kappa_{rw} = \kappa_w^0 \frac{S_{we}^{L_w}}{S_{we}^{L_w} + E_w(1 - S_{we})^{T_w}}, \quad \kappa_{rn} = \kappa_n^0 \frac{(1 - S_{we})^{L_n}}{(1 - S_{we})^{L_n} + E_n S_{we}^{T_n}}, \quad (2.24)$$

where L_w , E_w , T_w , L_n , E_n , and T_n are the parameters of the model. In addition to this, it is important to mention that the LET model is flexible enough to recover Corey's model under certain hypotheses. The LET model can be considered an extension and improvement of Corey's relative permeability relations.

2.5 Comparing the relative permeability models

A comparison of the relative permeability models is shown in Figure 9, which highlights how different can be the conclusions drafted employing the Corey's [32] model, Chierici's [25] model or the LET [92] model. Figure 9 shows a considerable mismatch in the models' calibration focusing on Corey's model where the oil relative permeability curve is poorly captured if comparing with the calibration of the Chierici's and LET models. We note that both Chierici's and LET models present an acceptable fitting. However, the LET model captures all the experimental data with higher fidelity. In addition to this, we show the discrepancies between the relative permeability models evaluating several quantities of interest. On the one hand, we have characteristics used to compute the solution to the Buckley–Leverett equation (2.12), such as water fractional flow function vs. water saturation, water fractional flow derivative function vs. water saturation. On the other hand, we show different physical evaluations concerning the properties of the waterflood in the core-sample, such as oil recovery factor vs. simulation time, water cut function vs. simulation time, and the water saturation profile at a fixed time. Analyzing the physical quantities like oil-recovery, water cuts, and water saturation profiles, we can notice that the distance between the evaluations adopting the Chierici's and LET models are more proximal than the model evaluations obtained adopting the Corey's. In any case, discrepancies exist between the Chierici's and LET model predictions. In summary, we verified that the model selection has significant consequences on the posterior analysis of the Buckley–Leverett equation, even if the model calibration presented minor discrepancies. The Corey's model parameters are $\{N_w = 3.16, N_o = 1.55\}$, the Chierici's mode parameters are $\{B = 2.29, M = 0.86, A = 2.73, L = 3.72\}$, and the LET model parameters are $\{L_w = 2.42, E_w = 3.13, T_w = 1.03, L_o = 6.11, E_o = 1.79, T_o = 4.11\}$. The water and oil viscosity are 4.7×10^{-4} (Pa s), and 2.7×10^{-2} (Pa s), respectively.

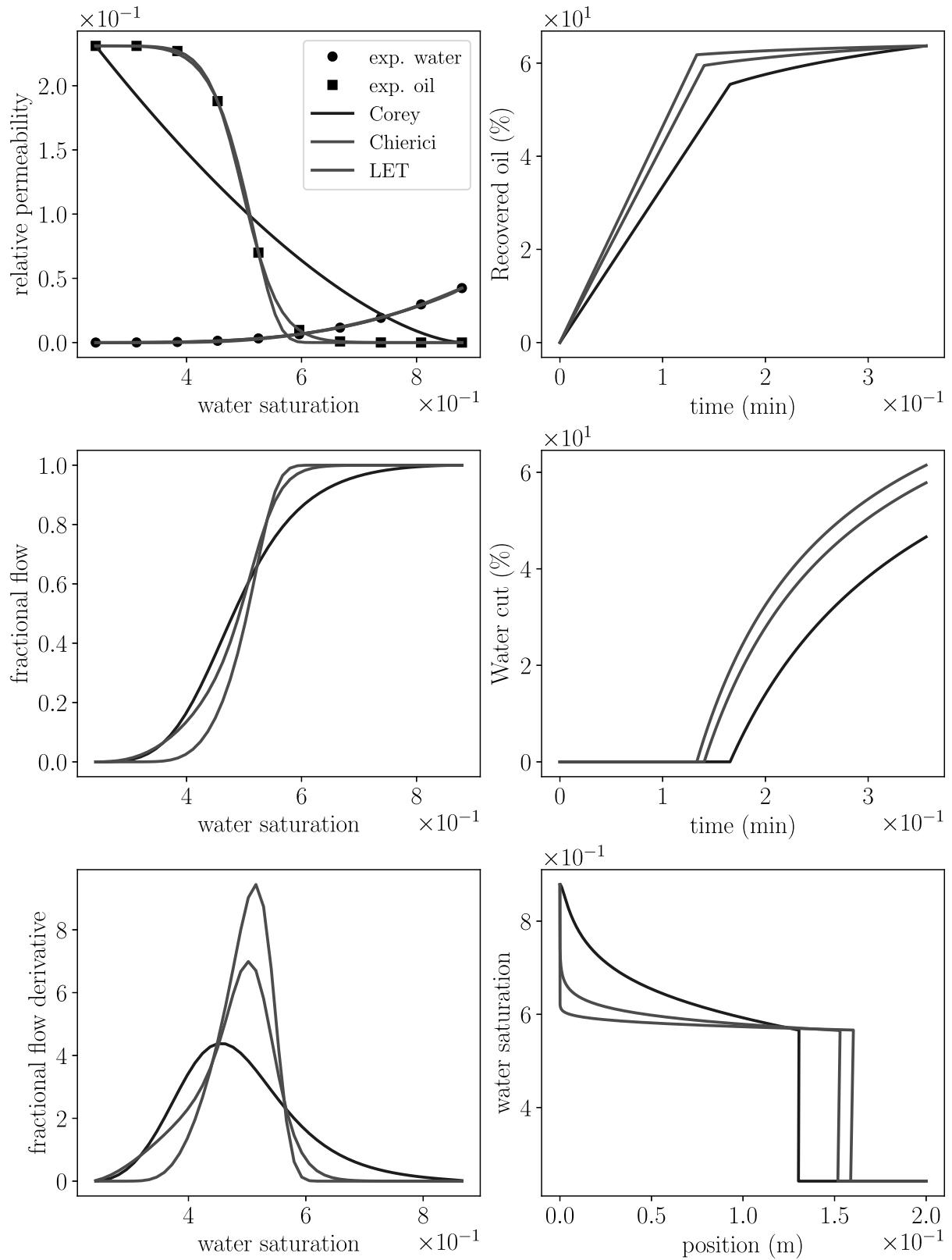


Figure 9 – Relative permeability models vs. model evaluations.

The characteristic speed depicted in Equation (2.15) transports saturation from boundary and initial conditions through the rectilinear domain $x \in [0, L]$. Figure 9 shows

discrepancies in fractional flow functions (and fractional flows' derivatives) when employing the relative permeability models. These discrepancies had origin in the adjustment of the relative permeability models. It is possible to observe how the solutions of the Buckley-Leverett equation are affected by such model mismatch, altering the predictions of recovered oil and water cut functions. The experimental observations of oil and water relative permeability values were chosen to highlight the flexibility of the Chierici's and LET models in contrast to Corey's model. Ignoring Corey's model, a "single" misfit on Chierici's oil–relative permeability evaluation affects all the forward results.

Different reservoir properties were evaluated considering the three relative permeability models. Table 1 displays the values of water–breakthrough instant (WBT), the saturation of the shock front (RK–H), mobility ratios at shock saturation (MRT), and relative permeability crossing point (CPT). Each of these evaluations can be used to characterize the flowing regime of the core sample.

Table 1 – Evaluation of water–breakthrough instant, saturation of the shock front, mobility ratio at shock front saturation, and relative permeability crossing point, using different relative permeability models.

Petrophysical feature	Corey	Chierici	LET
WBT [min]	1.78	1.46	1.70
RK–H [–]	0.57	0.57	0.56
MRT [–]	3.77	26.7	11.4
CPT [–]	0.74	0.57	0.60

With this example, we remark how the choice of the model affects the predictions and conclusions one may bring out solving the Buckley–Leverett equation, adopting the same experimental dataset and boundary conditions. Similar conclusions were communicated by Berg *et al.* [8, 9], Moghadasi *et al.* [101] as well as in [138].

2.6 Foam flow in porous media

In this section, the fundamental concepts of foam flow in porous media are described, and then the governing equations are discussed.

Modeling foam displacement at pore scale

Foam is defined as a dispersion of gas in a liquid such that the liquid phase is continuous (i.e., one gas region is connected to other gas regions by a liquid film) [41]. The liquid films are called lamellae, and the boundary between two contiguous gas regions are the Plateau borders.

Saye & Sethian [123] presented numerical simulations of different scenarios involving foam dynamics. The authors proved numerically that foam dynamics is a cumbersome problem that should be tackled considering different spatio-temporal scales. Based on their numerical evidence and experimental observations, the authors highlighted three main events:

- Drain. While foam seems to be in *macroscopic equilibrium*, liquid drains from the lamellae to the Plateau borders,
- Rupture. When the lamellae thickness approximates to a small value, (i.e., the foam bubble reaches the limiting disjoining pressure), the foam bubble will collapse,
- Restore. Rearrangement of the fluids due to surface tension and gas dynamics in order to recover a new macroscopic equilibrium, following the Plateau law.

According to [123], these three events happen in six different scales involving different spatial-temporal orders of magnitudes, and each of them may be modeled by non-linear partial differential equations.

As time evolves, liquid drains from the lamellae to Plateau borders, reducing the thickness of the lamellae. Immediately before the collapse of a foam bubble, the difference in pressure between the gas and liquid phases achieves a maximum value. This critical value is often known as critical disjoining pressure. The works of Bergeron & Radke [10] and Aronson *et al.* [4], conducted experiments with synthetic glass devices revealing that positive increments of disjoining pressure are proportionally correlated to significant reductions of the flowing rate (i.e., the flow gets slower as long as the disjoining pressure increases). While proximal foam bubbles will experience high values for the disjoining pressure, distant foam bubbles will experience small values of disjoining pressure. Foam flow with small values of disjoining pressure will also reduce the speed of the flow, yet in a smaller proportion than flow with higher disjoining pressure values. This behavior is because dryer foams are tempted to block the flow, while wet foams are responsible for maintaining a reduced flow rate.

Modeling foam displacement at Darcy's scale

Motivated by experimental observations, Falls *et al.* [41, 42], reported that the behavior of foam displacement in a porous medium satisfies the following statements:

- Foam does not alter the mobility of the water (i.e., wetting) phase,
- No conclusive results expressed that foams affect the gas relative permeability.

- The mobility of the gas is controlled by adjusting the viscosity of the gas. This behavior can be described by employing experimental information like pressure gradient and gas velocity, resulting in an *effective gas viscosity*.

The validity of these experimental observations was confirmed by Eftekhari & Farajzadeh [40]. The authors proved that foam affects gas mobility by modifying its viscosity. In addition to this, the authors exposed the relations between pore scale physics and Darcy's-scale physics. Hanssen [57, 58] and Heller & Kuntamukkula [61] listed the most relevant factors that affect the foam dynamics at pore scale, for completeness we mention them:

1. ratio between the bubble size and the size of the pore,
2. size distribution of bubbles,
3. flow-induced anisotropy of bubble distribution,
4. foamer-channel interactions,
5. pore-throat geometry,
6. foam quality,
7. fluid's properties,
8. pressure drop,
9. time dependent properties of foam bubbles.

In particular, Heller & Kuntamukkula [61] validated the models developed by Falls *et al.* [42] and Hirasaki & Lawson [64], supporting the concept of foam texture, which relates to the number of foam bubbles per volume. Following Hirasaki & Lawson [64] the effective gas viscosity relies on the geometry of the slugs between two bubbles, resistance to deform the bubble, and the surface tension gradients. Moreover, Khatib *et al.* [82] exposed dynamic aspects of the generation and coalescence of foam bubbles, developing the Darcy's-scale concept for limiting capillary pressure (arising as a counterpart to the pore scale disjoining limiting pressure).

The modeling of foam dynamics at Darcy's scale inherits several concepts from the modeling at pore scale. At pore scale the foam stability is determined by the disjoining pressure between two different bubbles. Similarly, in Darcy's scale the stability of foam bubbles is governed by the concept of limiting capillary pressure. Dryer foam bubbles can reduce the flow motion, although they are suitable to face massive collapse due to the liquid film drainage phenomena. Dry foams are often known as strong foams due to the high values of disjoining pressure they are subjected to. Analogously, wet foams are known as weak foams due to their poor capability to slow down the fluid motion. Figure 10 presents a schematic representation extending the explanation observed in the work of Khatib *et al.* [82]. In particular, we link the critical capillary pressure with the concept of

limiting water saturation and critical foam quality. The two flowing regimes are known as low-quality regime (LQR) and high-quality regime (HQR). From Figure 10 we can notice that the events happening in the HQR are in the presence of dryer and unstable foam formulations. Whereas the events happening in the LQR count with the presence of wet and stable foam formulations.

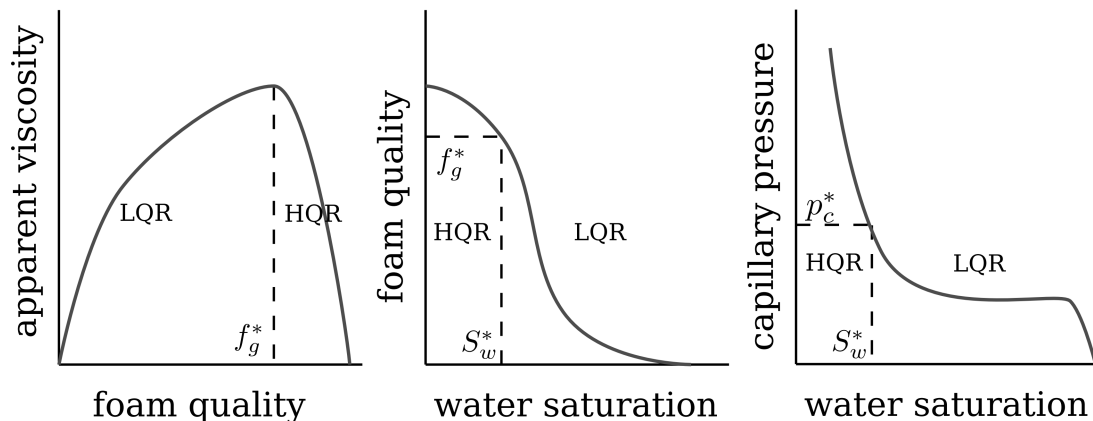


Figure 10 – Schematic representation of the LQR–HQR regimes.

As appointed by Aronson *et al.* [4] if the capillary pressure in the porous medium is above a threshold value, the lifetime of the foam lamellae will be shortened significantly, reducing the number of foam bubbles per volume not collaborating to slow the flow motion.

With the experimental evidence and mathematical developments, there is an agreement to model foam dynamics at the Darcy's scale altering the gas mobility by redefining the gas viscosity. The effects of adding foam bubbles to the water–gas system presents two different regimes. On the one side, the low-quality regime (LQR) and on the other side the high-quality regime (HQR). The transition between regimes corresponds to the abrupt collapse of foam bubbles due to higher values of capillary pressure, as depicted in Figure 10.

Mathematical models to simulate foam displacement at Darcy's scale

The modeling of foam dynamics at Darcy's scale is done incorporating the gas mobility reduction factor (MRF) concept. This mobility reduction factor changes the total relative mobility (of the mixture water and foamed gas) and allows to define the apparent viscosity of the system; these changes are addressed as follows. First the total relative mobility,

$$\lambda_T = \lambda_w + \frac{\lambda_g}{MRF}, \quad (2.25)$$

and secondly for the apparent viscosity,

$$\mu_{app} = \left(\lambda_w + \frac{\lambda_g}{MRF} \right)^{-1}. \quad (2.26)$$

The fractional flow for the gas phase (known as foam quality) takes into account these modifications showing the next functional dependency with the MRF,

$$f_g = \frac{\lambda_g}{MRF \left(\lambda_w + \frac{\lambda_g}{MRF} \right)} = \frac{\lambda_g}{MRF} \mu_{app}. \quad (2.27)$$

From the literature, we can recognize two main groups for labeling models to simulate the displacement of foam in porous media, briefly they are introduced as follows:

- Population Balance (PB) models. They are based on partial differential equations to characterize foam dynamics in a porous medium. The displacement of water and foamed gas in a porous medium is based on the mass conservation principle for the two phases (water and gas) and a population balance equation for the foam texture variable. The latter describes the lamellae creation and coalescence rates to calculate the foam texture. The following system of equations gives the typical structure of a PB model:

$$\begin{cases} \frac{\partial S_w}{\partial t} + \frac{Q}{\varphi a} \frac{\partial}{\partial x} (f_w) = 0, & \text{in } [0, L] \times [0, T], \\ \varphi \frac{\partial S_g n_D}{\partial t} + \frac{\partial}{\partial x} (u_g n_D) = \varphi S_g (r_g - r_c), & \text{in } [0, L] \times [0, T]. \end{cases} \quad (2.28)$$

where n_D is the normalized foam texture (related to the number of bubbles per volume). Most of the PB models make use of the Hirasaki & Lawson expression [64] for effective gas viscosity (μ_g^f), yielding the following definition:

$$\mu_g^f = \mu_g \left(1 + \alpha \frac{n_D}{\mu_g v_g^\beta} \right), \quad (2.29)$$

where (α, β) are parameters to be determined, and $v_g = u_g / (\varphi S_g)$ is the gas effective velocity. The physical interpretation of the Equation (2.29) has been described in [22, 149], where shear–thinning and shear–thickening behavior are discussed. Because of the nonlinearities presented in Equations (2.28) and (2.29) most of the PB models poses numerical challenges. PB models that used the Hirasaki & Lawson expression will produce the next closed equation for the MRF function,

$$MRF = \left(1 + \alpha \frac{n_D}{\mu_g v_g^\beta} \right). \quad (2.30)$$

- Semi–Empirical (SE) models. They are primarily used in commercial simulators like CMG–STARS [31] or UT–CHEM [24] due to their capacity to perform fast computations. These models use algebraic expressions to calculate the mobility reduction factor rather than solving the partial differential equation to obtain the foam texture and MRF values. Therefore, SE models should not be trusted to describe the transient regimes of creation and coalescence of foam bubbles in a porous medium. However, they assess numerical solutions accurately enough compared with the PB models at steady–states’ flowing regimes.

Assuming local–equilibrium (LE), it can be shown that the PB and SE models foam flow responses agree with each other. Gassara *et al.* [51, 52] compared CMG–STARS [31] with the Kam and Rossen model [76, 75], while Cavalcante *et al.* [48] studied the PB model proposed by Chen *et al.* [23] and the SE implementation found in UT–CHEM [24], in a similar approach Lotfollahi *et al.* [95] compared the mentioned foam models and others that were omitted employing two datasets.

2.6.1 Foam models

This thesis presents a detailed comparison of two different foam flood models. The CMG–STARS model [31] and the Linear Kinetic (LK) model developed by Ashoori *et al.* [5].

CMG–STARS model [31]. Due to its versatility, the CMG–STARS model can simulate the effects of foam in a reasonable computational time considering different effects like surfactant concentration, water saturation, oil saturation, gas velocity, capillary number, critical capillary number. In this thesis, we will expose the main features of the CMG–STARS model analyzing the water saturation and the capillary number effects. The CMG–STARS’ mobility reduction factor reads the following expression:

$$\begin{aligned} MRF &= 1 + fmmob F_{water} F_{shear}, \\ F_{water} &= \frac{1}{2} + \frac{1}{\pi} \arctg(sfbet(S_w - SF)), \\ F_{shear} &= \begin{cases} \left(\frac{fmcap}{N_{ca}}\right)^{epcap} & , \text{ if } N_{ca} \geq fmcap, \\ 1 & , \text{ if } N_{ca} < fmcap. \end{cases} \end{aligned} \quad (2.31)$$

The model parameters are $fmmob$, $sfbet$, SF , and $epcap$. Where $fmmob$ represents the maximum mobility reduction that can be achieved considering the effects of foam, $sfbet$ is a transition coefficient associated to the LQR–HQR flowing regime passage (higher values of $sfbet$ represent a sharp transition, while smaller values of $sfbet$ will produce a smooth transition), SF corresponds to the water saturation where the capillary pressure meets its critical value collapsing the foam bubbles. After fixing the parameter $fmcap$ in the lowest capillary number (as suggested by Farajzadeh *et al.* [45], and Kapetas *et al.* [79]) it is recommended to use the calibrated value of $epcap$ to characterize the foam rheology as Newtonian or non–Newtonian. The Capillary number written in Equation (2.31) is evaluated using the definition:

$$N_{ca} = \frac{\mu_{app} u}{\sigma}, \quad (2.32)$$

where u and σ are the inflow velocity (Darcy’s velocity) and the water–gas surface tension, respectively. From here two different models can be used independently. On the one hand,

foam model with Newtonian behavior

$$MRF = 1 + fmmob F_{water}. \quad (2.33)$$

And on the other hand, a model with non-Newtonian rheology,

$$MRF = 1 + fmmob F_{water} F_{shear}. \quad (2.34)$$

Linear Kinetic (LK) model [5]. The LK model is a population balance model that satisfies the structure of Equation (2.28), where the source term associated with the foam texture equation is given by a first-order kinetic expression based on the works of Zitha [150] as well as Zitha & Du [149], yielding the following equation:

$$r_g - r_c = k_c (n_D^{LE} - n_D), \quad (2.35)$$

where k_c estimates the frequency of creation and coalescence of foam bubbles, n_D^{LE} stands for the foam texture at local equilibrium state. Here the authors proposed the next expression for the n_D^{LE} variable:

$$n_D^{LE} = \begin{cases} \tanh(A(S_w - S_w^*)), & S_w > S_w^*, \\ 0, & S_w \leq S_w^*. \end{cases} \quad (2.36)$$

The mobility reduction factor reads the next definition, revealing functional discrepancies with the Hirasaki & Lawson's Equation (2.30) returning a Newtonian constitutive law,

$$MRF(n_D) = 1 + C_{mrf} n_D, \quad (2.37)$$

where C_{mrf} , A and S_w^* are the parameters of the model. The parameter C_{mrf} is the maximum mobility reduction that can be achieved by the model, A quantifies how sharp or smooth is the LQR-HQR transition, and S_w^* is the water saturation where the capillary pressure meets the critical value, above which foam bubbles will massively collapse.

2.7 Comparing the LK and the CMG-STARS models

Comparisons between the CMG-STARS models and the LK model were reported in the literature; for instance, the work of Kapetas *et al.* [80] exploits the capabilities of the CMG-STARS model's F_{water} to rewrite the local equilibrium expression for the LK's mobility reduction factor. In particular, [80] proposes a transient extension in the CMG-STARS model. In a different study, we exposed in [137] the similarities using the Bayesian calibration considering the Newtonian variant of CMG-STARS and the LK model, with a Newtonian experimental dataset.

The following example takes a dataset from the literature [3], in particular, we highlight the discrepancies between the Newtonian and non-Newtonian variants from

CMG–STARS with the Linear kinetic (LK) approach. Initially, we show in Figure 11 the discrepancies between the three models, highlighting their apparent similar fitting capabilities and their notorious rheological differences. Analyzing the mobility reduction at the LQR, we can notice the shear–thinning effects on the non–Newtonian CMG–STARS’ variant. In this context, Newtonian models achieve uniform stagnation of their MRF values in the entire LQR. The three models revealed the same foam bubbles’ collapse pattern reducing the MRF monotonically at the HQR.

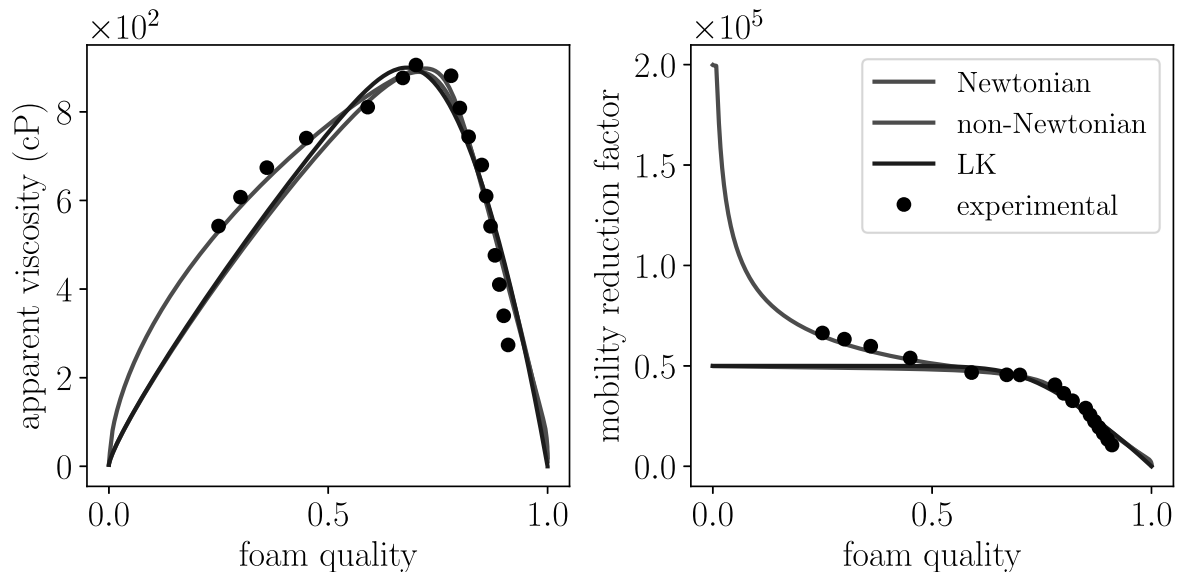


Figure 11 – LK and CMG–STARS models evaluation vs foam quality.

The model comparison is completed by analyzing different quantities like apparent viscosity, total relative mobility, mobility reduction factor, and foam quality as functions of the water saturation. The analysis depicted in Figure 12 shows that the three models capture the same limiting water saturation (i.e., same limiting capillary pressure). The non–Newtonian variant of CMG–STARS reports differences with the other models only on the mobility reduction factor for higher water saturation values. At lower water saturation values (i.e., dryer foams), the collapse of foam bubbles shows the same trend in the three models analyzing the four quantities of interest. However, the LK model experiences the LQR–HQR transition with remarkable sharpness, whereas both CMG–STARS’ variants present smooth transitions.

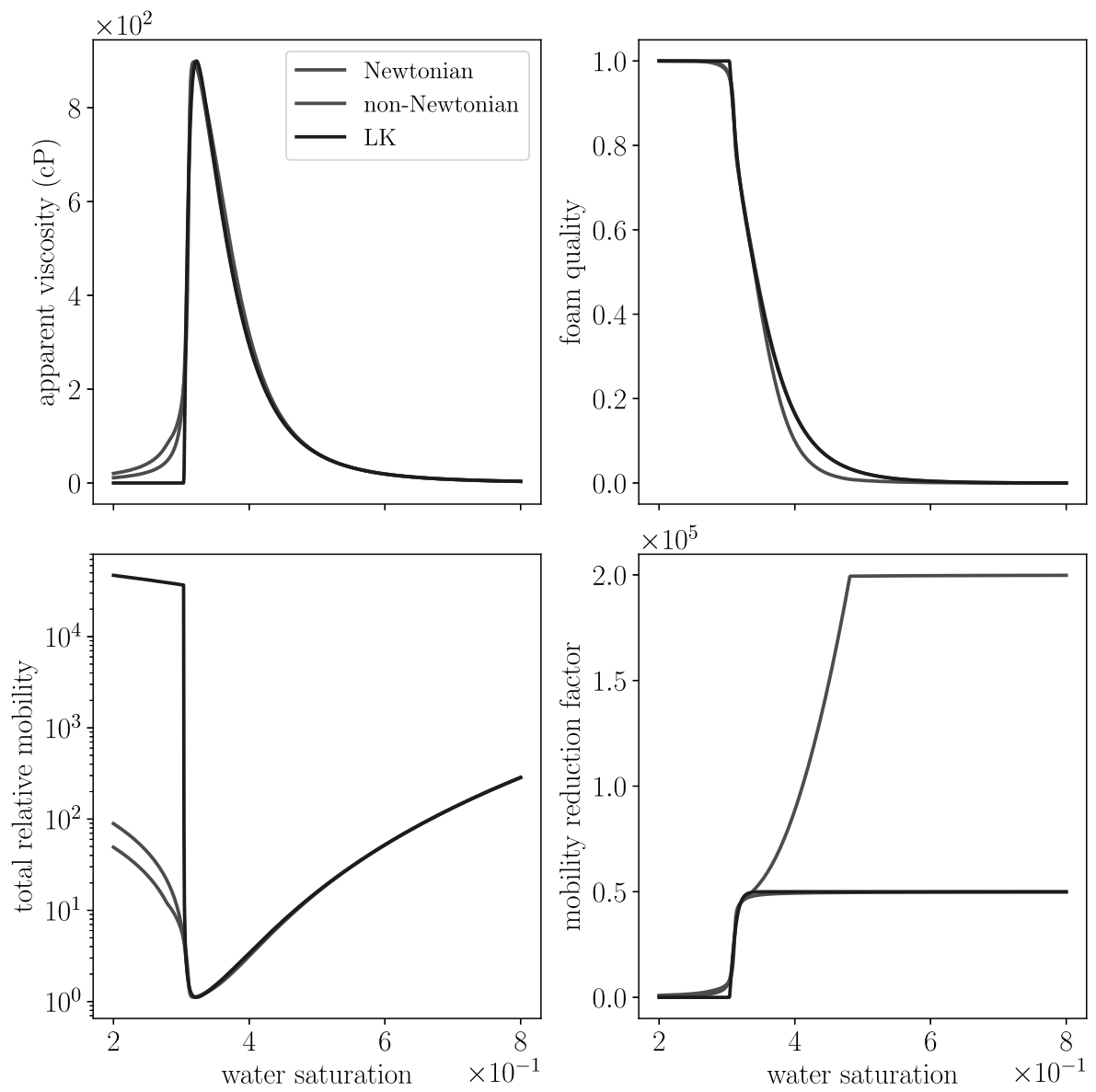


Figure 12 – LK and CMG-STARS models' evaluation vs water saturation.

3 Uncertainty quantification and sensitivity analysis techniques

One of the challenges in the application of foam flow models for EOR is the adaptation of model parameters (inputs) to characterize core, reservoir or fluid flow conditions. In particular, the inputs to be characterized in the context of foam-assisted EOR include relative permeability models, physical parameters (describing for instance foam dynamics such as effects of water saturation, shear-thinning effect, creation and destruction of bubbles and others), initial and boundary conditions (describing, for instance, injection and recovery). Experimental data of these properties are usually hindered by measurement uncertainty, which in turn translates into uncertainty of these input parameters. The identification of these parameters and its uncertainties, and the quantification of the uncertainty in the model predictions that results from uncertainties in model inputs are crucial for robust and reliable simulations. In addition, the determination of which model parameters have the major impact on the outputs through a sensitivity analysis is also important to improve measurements accuracy or to fix these parameters at their baseline values.

This chapter introduces the methods used to perform inverse uncertainty quantification, forward uncertainty quantification, and sensitivity analysis. In particular, we will introduce the following methods for uncertainty quantification: the Markov Chain Monte Carlo method, the classical Monte Carlo, and Polynomial Chaos Expansions. A detailed introduction to UQ methods is available in the literature [35, 39, 46, 145] as well as for SA methods [128, 59, 36, 125, 112, 21].

3.1 Uncertainty Quantification

Uncertainty quantification (UQ) aims to estimate the variability that a model can propagate in the presence of unpredictable inputs [100]. Every model is subjected to a certain degree of uncertainty due to manufacturing tolerances, constitutive properties of materials, or insufficient knowledge related to operational conditions. Propagating these uncertainties to the models' output is one aspect of UQ, which is often referred to as to *forward uncertainty quantification*. The other aspect that UQ pursues is the characterization of the input parameters of a model given experimental data, which is known as *inverse uncertainty quantification*.

The general framework to perform UQ studies, as described by Eck *et al.* [39], McClarren [100], and Sudret [129], consists of a series of steps to assess the uncertainty in a model. The following steps summarize an UQ study:

1. Identify Quantities of Interest (QoIs);
2. Model uncertainties in the system's inputs;

3. Propagate uncertain inputs through simulations to the outputs;
4. Determine how uncertainties affect the model predictions.

Each of the previous steps should be carefully designed by the user. Different kinds of problems (for instance, elasticity, fluid mechanics, or reservoir engineering) will have different kinds of QoIs and different kinds of model inputs. Figure 13 shows a scheme exposing the interaction between the main parts of the UQ–SA workflow. In particular, it is possible to recognize the cyclic nature of the UQ–SA study, starting from parametric uncertainty and concluding on parameters' influences on several QoIs.

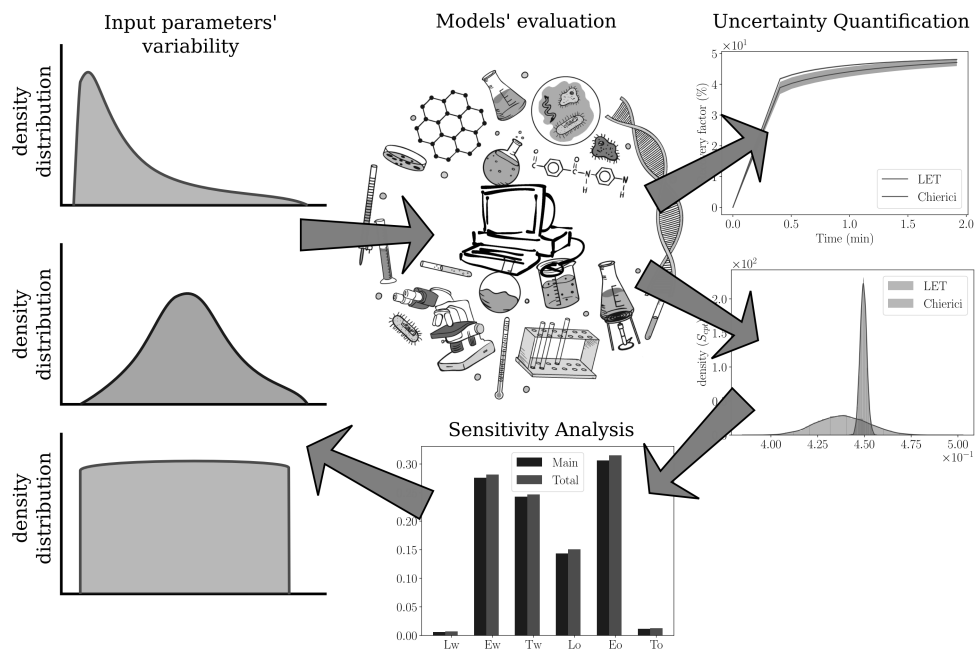


Figure 13 – Main parts of the UQ–SA workflow and its interactions.

Identifying QoIs

Computational models generally return the solution of a problem defined over a specific domain with a fixed set of boundary/initial conditions. In this work, the two–phase flow in a porous medium is considered. Under specific hypotheses, the solution to this problem is wetting and non–wetting saturation through time and space. However, a QoI should be a single scalar function.

3.2 Modeling of uncertainties in the system's inputs

Theoretical models are conceived to extend and better explain experimental outcomes. Under particular constraints/hypotheses, the model should recover the experimental setting and extend the experiment to different scenarios. In this context, the limitations of the developed model rely (mostly) on the hypothesis. By adjusting the model

to the experimental setting, the user should explain the experiment with the theoretical model. Two sources of uncertainties are recognized [100, 129] aleatory uncertainty and epistemic uncertainty. Aleatory uncertainty concerns the system's inherent randomness (for example, predicting the position and momentum of an electron that orbits the core of an atomic model). Epistemic uncertainty refers to the limited knowledge about the system. An example of epistemic uncertainty could be a tolerance related to experimental measuring. At the end of this stage, the system inputs should be identified, and their uncertainty should be described, for example, with a probability density function (PDF).

3.2.1 Estimating input uncertainties

The Bayes' rule relates the probability of an event employing prior information; the following expression gives it:

$$\mathbb{P}(A|B) = \frac{\mathbb{P}(B|A) \mathbb{P}(A)}{\mathbb{P}(B)}, \quad (3.1)$$

where $\mathbb{P}(m|z)$ is the probability of the event m constrained to the probability of the event z , and $\mathbb{P}(m)$ is the probability of the event m . In this thesis, the Bayes' rule is used to estimate the variability of the model's parameters considering errors on the observed data. For a finite set of input parameters $\mathbf{x} \in \mathbb{R}^{Np}$ the Bayes' rule is applied straightforwardly considering experimental data D as follows:

$$\pi(\mathbf{x}|D) = \frac{\pi(D|\mathbf{x}) \pi(\mathbf{x})}{\pi(D)}, \quad (3.2)$$

where $\pi(D)$ is the probability distribution associated with the experimental observations. $\pi(\mathbf{x})$ is the prior knowledge associated with the uncertain parameters \mathbf{x} . $\pi(D|\mathbf{x})$ is the probability of the observed data conditioned to the parameters' \mathbf{x} probability. The conditional probability term $\pi(D|\mathbf{x})$ is materialized by the likelihood function. Assuming that the experimental observations' variability does not change, the following relation holds true

$$\pi(\mathbf{x}|D) \propto \pi(D|\mathbf{x}) \pi(\mathbf{x}).$$

The Markov Chain Monte Carlo (MCMC) method is a class of algorithms that benefits from successive evaluations of the Bayes' rule by storing samples in a Markov chain. After many evaluations, the Markov chain converges asymptotically to the kernel of the posterior distributions associated with each model, parameter [17, 18].

In this work, the execution of the MCMC method was carried out using different implementations available as Python libraries [54, 49, 121].

An example of the MCMC method

An academic example is used next to illustrate how the MCMC method results are presented. Given a finite collection of data-points (x_i, y_i) , we estimate the parameters

of the function $y = (\alpha + \beta \sin(x)) \exp(-0.05x)$ using the MCMC method. The dataset was generated adding a 20% Gaussian noise relative to the values of the known function $y = (2 + \sin(x)) \exp(-0.05x)$.

Figure 14 (left) is used to explain how the synthetic dataset was created. Gaussian noise was added to the model evaluations. In this example, we employ the perturbed data to recover the original noise-free function. Figure 14 (right) displays different posterior model evaluations in shaded green, and the model evaluation corresponding to the maximum a posteriori (MAP), that equals the mode of the posterior distribution, in dashed red.

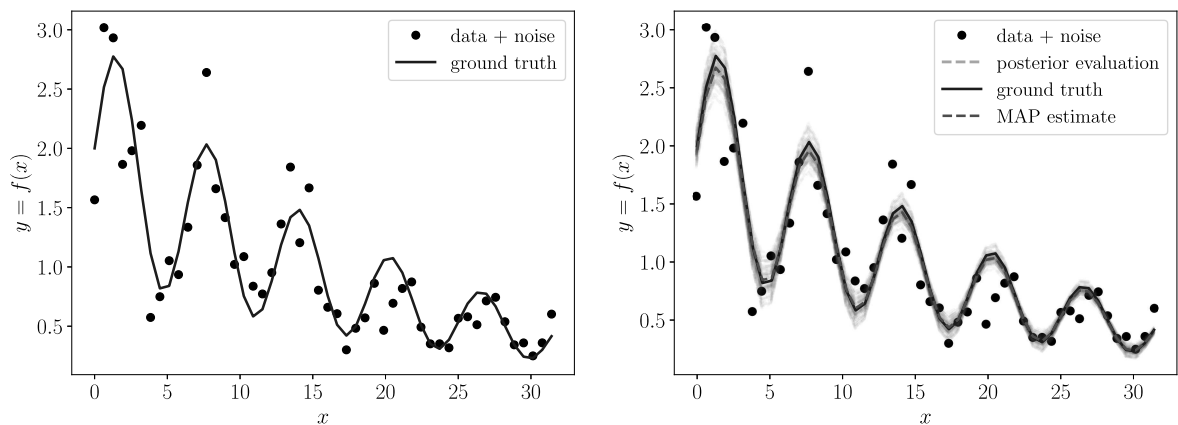


Figure 14 – Inverse modeling calibration results and the MAP estimate.

The MCMC method was executed adopting the following prior distributions for the uncertain coefficients α and β :

$$\alpha \sim \mathcal{U}(0, 15), \quad \beta \sim \mathcal{N}(0, 10).$$

That is, an uniform prior distribution ranging from 0 to 15 was assumed for α , whereas a normal prior distribution was assumed for β with mean and standard deviation given by 0 and 10, respectively.

The posterior distribution for each model parameter α and β obtained by the MCMC method is depicted in Figure 15. One can observe that the posteriors have a symmetric shape resembling normal distributions, whereas the mean values for α and β are close to 2 and 1, respectively.

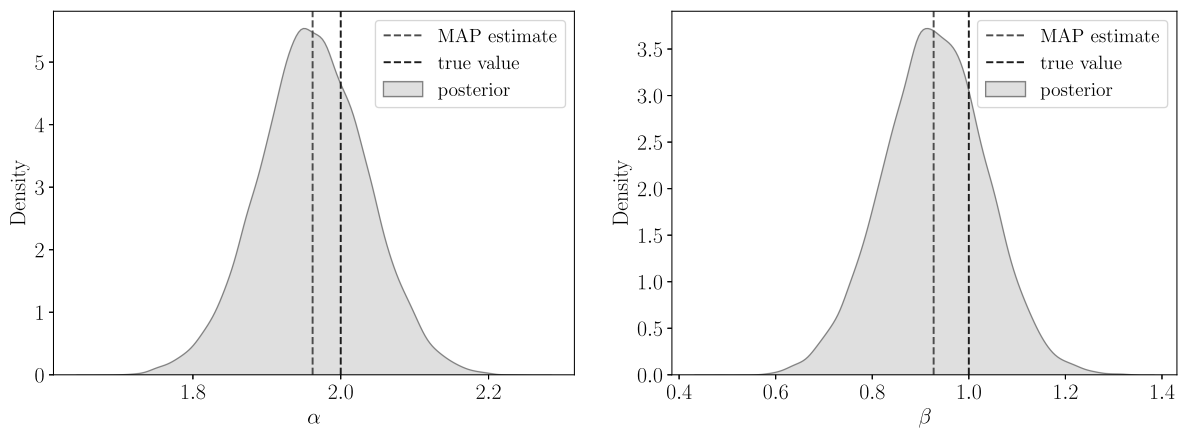


Figure 15 – Posterior distributions obtained the parameters α (left) and β (right).

In this example, we used the MCMC method to perform the model calibration and estimate the variability of the parameters. The example shows the robustness and versatility to solve inverse problems associated to non-linear models and considering experimental data hampered by measurement errors, and how to characterize parametric uncertainty.

3.2.1.1 Identifiability analysis

The MCMC method is a robust alternative to estimate the variability of parameters when performing the model calibration to a finite dataset. Yet, the MCMC is not fully protected against over-parametrized models and/or non-adequate experimental observations. Identifiability studies are employed to determine if the model's complexity matches the information contained within the experimental records. Therein, identifiability analysis returns alternatives to improve the model and/or add different experimental observations to constrain better the posterior density distributions.

A common approach used to screen identifiability is the analysis based on the profile likelihood [77, 115]. For any model parameter $x_i \in \mathbf{x}$ the associated profile likelihood is defined as:

$$\mathcal{X}_{PL}^2(x_i) = \min \left[\mathcal{X}^2(\mathbf{x}) \right]_{\mathbf{x} \setminus \{x_i\}}, \quad (3.3)$$

where $\mathcal{X}_{PL}(x_i)$ stores the residual values after fixing $x_i \in [\min(x_i), \max(x_i)]$ and fitting the remaining model parameters $\mathbf{x} \setminus \{x_i\}$.

The estimation of a model parameter can be classified as (i) identifiable, (ii) practically non-identifiable, and (iii) structurally non-identifiable [115, 116, 77]. Structural non-identifiability is related to the mathematical structure of the model, whereas practical non-identifiability is related to the quality of observed data. In practical terms, a model parameter is identifiable if the profile likelihood function depicted in Equation (3.3) presents

a single minimal value. In a similar take, a model parameter is identifiable if its confident interval (estimated with the profile likelihood function) is finite [115]. A model parameter x_i is structural non-identifiable if the associated profile likelihood remains flat or shallow in the entire search range $[\min(x_i), \max(x_i)]$. Practical non-identifiable parameters have profile likelihood functions that contain a minimal value, yet it is not necessarily unique.

Practical non-identifiability problems associated to the model parameter x_i may be corrected restricting the range $[\min(x_i), \max(x_i)]$ where the best fit value is being explored. Alternatively, practical non-identifiability issues are suitable to be reduced if the quality of the experimental data is improved. Another different solution to mitigate practical non-identifiability issues is to fix redundant model parameters.

3.3 Propagation of uncertainties

Once the (posterior) distributions of the parameters have been characterized by the MCMC method (or any other alternative), we assess the models' variability via forwarding UQ. The estimated uncertainty in the model parameters can be propagated to the model's outputs and be quantified in terms of expected value, variance, and other statistical information.

Models are described as functions like $\mathcal{M} : \mathbf{x} \mapsto \mathcal{Y} = \mathcal{M}(\mathbf{x})$ where $\mathbf{x} \in \mathbb{R}^{N_p}$, here N_p represent the number of input parameters. The response \mathcal{Y} is the result of the process \mathcal{M} (usually considered as a *black box*) applied to the input vector \mathbf{x} . For a fixed input vector \mathbf{x} , the response \mathcal{Y} given by the model remains the same (deterministic). This thesis employed the Monte Carlo method and emulators based on polynomial regressions like the Polynomial Chaos Expansion (PCE) method to perform forward UQ studies.

The result of UQ studies should be knowledge of the QoI and its uncertainty. Expected value, variance, and prediction intervals are used as metrics to characterize the variability in the output. Prediction intervals are evaluated using the percentile estimation for any QoI distribution, as reported by Eck *et al.* [39].

3.4 Sensitivity Analysis

Sensitivity analysis (SA) arises as a tool that can contribute to the process of evaluating a model. A SA study evaluates how sensitive the outputs of a given model are to uncertainties at the inputs. Two primary SA methods can be identified [120]:

- Local methods: varies each parameter one by one while keeping the others fixed and explore the model's output dependency with the variation of each parameter, for example, methods based on derivatives.

- Global methods: varies all the parameters simultaneously, exploring the input space of the model, for example, Sobol's method.

Differently from local techniques like derivatives or adjoint methods, global approaches usually require more computational efforts. However, they can easily identify interactions between input parameters [130, 119].

In this work, a global SA approach based on Sobol's indices is used to classify the input parameters in terms of their influence on the model's output. With this input parameter ranking, two different groups of parameters will be distinguished: parameters that can be fixed (without compromising the model's output) and parameters that can not be fixed and should be worth improving its estimation.

3.5 Emulators, surrogate models

UQ and SA studies usually require several evaluations of the computational model. Eventually, when the cost of one model evaluation is high, or the number of model evaluations required to carry out the UQ and SA study is very high because many parameters are involved, the study may be impractical. When the number of model evaluations or the total cost becomes impractical, the analysis can be carried out by constructing approximations of the model evaluations. These approximations are often known as surrogate models or emulators. In this work, emulators based on the Polynomial Chaos Expansion (PCE) are also explored.

3.5.1 Polynomial Chaos Expansion (PCE)

The posterior density distributions obtained after the MCMC execution are used to define the joint probability distribution yielding the following expression,

$$\boldsymbol{\pi}(\mathbf{x}) = \prod_i^{N_p} \pi_i(x_i), \quad (3.4)$$

where $\{x_i\}_{i=1}^{N_p} = \mathbf{x} \in \mathbb{R}^{N_p}$. Each marginal distribution $\pi_i(x)$ span a subspace \mathcal{U}_i with the following inner product operation,

$$(u; v)_{\mathcal{U}_i} = \int_{\mathbb{R}} u v \pi_i(x) dx. \quad (3.5)$$

By taking an orthonormal basis of the subspace \mathcal{U}_i , we extend the inner product operation to N_p dimensions as follows:

$$(u; v)_{\mathcal{U}} = \int_{\mathbb{R}^{N_p}} u v \boldsymbol{\pi}(\mathbf{x}) d\mathbf{x}. \quad (3.6)$$

PCE emulators benefit from the orthonormal basis returning the following linear combination,

$$\mathcal{Y}^{PC} = \sum_{i=0}^{N-1} \psi_i(\mathbf{x}) y_i. \quad (3.7)$$

The number of terms N considered in the expansion is a function of the number of uncertain inputs Np and the polynomial degree P_d given by [39, 131]:

$$N = \frac{(Np + P_d)!}{Np!P_d!}. \quad (3.8)$$

The coordinates $\mathbf{y} = \{y_i\}_{i=0}^{N-1}$ are determined using the properties of each inner product subspace \mathcal{U}_i . On the one hand, we have the projection method [129] based on the orthogonality of the basis. For example, the coordinate y_i is defined as the next projection

$$y_i = (\mathcal{Y}; \psi_i(\mathbf{x}))_{\mathcal{U}} = \int_{\mathcal{D}} \mathcal{Y} \psi_i(\mathbf{x}) \boldsymbol{\pi}(\mathbf{x}) \, d\mathbf{x}. \quad (3.9)$$

And on the other hand, we have the regression method based on minimizing the distance between the PCE emulator \mathcal{Y}^{PC} and the model \mathcal{Y} . The functional to be minimized reads the next definition:

$$\mathcal{J}(\mathbf{b}) = \left[\int_{\mathcal{D}} (\mathcal{Y} - \boldsymbol{\Psi}(\mathbf{x}) \mathbf{b}) \boldsymbol{\pi}(\mathbf{x}) \, d\mathbf{x} \right]^2, \quad (3.10)$$

where $\mathbf{b} \in \mathbb{R}^N$ are any possible coordinates (including the unknown PCE coordinates), and $\boldsymbol{\Psi}(\mathbf{x}) = \{\psi_i(\mathbf{x})\}_{i=0}^{N-1}$. Consequently the PCE coordinates are feasible to be obtained as:

$$\mathbf{y} = \arg \min_{\mathbf{b} \in \mathbb{R}^N} \mathcal{J}(\mathbf{b}). \quad (3.11)$$

The minimization scheme has an algebraic equivalent problem which is obtained setting null the first variation of the functional \mathcal{J} evaluated in the unknown coordinates \mathbf{y} towards any possible change of such coordinates. We write the variational equation as follows:

$$\frac{d}{d\varepsilon} \mathcal{J}(\mathbf{y} + \varepsilon \hat{\mathbf{y}})|_{\varepsilon=0} = 0, \quad \forall \hat{\mathbf{y}} \in \mathbb{R}^N, \quad \text{for any } \varepsilon \in \mathbb{R}, \quad (3.12)$$

after some manipulations, the next equation is obtained,

$$\int_{\mathcal{D}} \boldsymbol{\Psi}(\mathbf{x}) \mathbf{y} \boldsymbol{\Psi}(\mathbf{x}) \hat{\mathbf{y}} \boldsymbol{\pi}(\mathbf{x}) \, d\mathbf{x} - \int_{\mathcal{D}} \mathcal{Y} \boldsymbol{\Psi}(\mathbf{x}) \hat{\mathbf{y}} \boldsymbol{\pi}(\mathbf{x}) \, d\mathbf{x} = 0, \quad \forall \hat{\mathbf{y}} \in \mathbb{R}^N. \quad (3.13)$$

By setting $\boldsymbol{\Psi}(\mathbf{x}) \hat{\mathbf{y}} = \delta(\mathbf{x} - \mathbf{x}_i)$, with $\delta(\cdot)$ being the Dirac delta function with $i = \{0, 1, \dots, N-1\}$, we obtain the following linear algebra problem,

$$\boldsymbol{\Psi}(\mathbf{x}) \delta(\mathbf{x} - \mathbf{x}_i) \mathbf{y} = \mathcal{Y} \delta(\mathbf{x} - \mathbf{x}_i). \quad (3.14)$$

The system of linear equations whose solution determines the coordinates of the PCE expansion reads the next matrix vector representation:

$$\begin{bmatrix} \boldsymbol{\Psi}_0(\mathbf{x}_{(0)}) & \boldsymbol{\Psi}_1(\mathbf{x}_{(0)}) & \dots & \boldsymbol{\Psi}_{N-1}(\mathbf{x}_{(0)}) \\ \boldsymbol{\Psi}_0(\mathbf{x}_{(1)}) & \boldsymbol{\Psi}_1(\mathbf{x}_{(1)}) & \dots & \boldsymbol{\Psi}_{N-1}(\mathbf{x}_{(1)}) \\ \vdots & \vdots & \ddots & \vdots \\ \boldsymbol{\Psi}_0(\mathbf{x}_{(N-1)}) & \boldsymbol{\Psi}_1(\mathbf{x}_{(N-1)}) & \dots & \boldsymbol{\Psi}_{N-1}(\mathbf{x}_{(N-1)}) \end{bmatrix} \begin{bmatrix} y_0 \\ y_1 \\ \vdots \\ y_{N-1} \end{bmatrix} = \begin{bmatrix} \mathcal{Y}(\mathbf{x}_{(0)}) \\ \mathcal{Y}(\mathbf{x}_{(1)}) \\ \vdots \\ \mathcal{Y}(\mathbf{x}_{(N-1)}) \end{bmatrix}. \quad (3.15)$$

Increasing the polynomial order P_d can improve the surrogate model's performance but at the expense of high computational cost. A typical procedure to improve the accuracy of the polynomial surrogate model obtained with PCE is to consider several samples N_s larger than the minimum N required to determine the coefficients of the polynomial [68]. Typically a number of samples $N_s = k N$ with k is a positive integer factor. This procedure results in an over determined system that is solved using linear least-squares methods [47].

$$\mathbb{E}[\mathcal{Y}] = \int_{\mathcal{D}} \mathcal{Y}^{PC} \boldsymbol{\pi}(\mathbf{x}) \, d\mathbf{x} = y_0, \quad (3.16)$$

$$\mathbb{V}[\mathcal{Y}] = \int_{\mathcal{D}} (\mathcal{Y}^{PC} - \mathbb{E}[\mathcal{Y}])^2 \boldsymbol{\pi}(\mathbf{x}) \, d\mathbf{x} = \sum_{j=1}^{N-1} y_j^2. \quad (3.17)$$

Another useful metric to study the QoI's uncertainty is the coefficient of variation (CoV), which is defined as the ratio of standard deviation and expected value $\text{CoV}(\mathcal{Y}) = 100\% \times \sqrt{\mathbb{V}[\mathcal{Y}]/\mathbb{E}[\mathcal{Y}]}$; as well as the prediction intervals evaluated from the QoIs' distributions.

3.5.2 Accuracy of the surrogate model

The PCE surrogate model's performance for each output quantity \mathcal{Y} depends on the chosen polynomial degree P_d and the number of samples N_s used. One approach to verify the surrogate model performance is the leave-one-out (LOO) cross-validation test [55], which was employed in this work to check if a specific combination of polynomial degree and the number of samples results in an accurate approximation. The LOO test can be summarized in the following steps:

1. From the N_s samples, take one sample \mathbf{x}_k , evaluate $\mathcal{Y}^{PC}(\mathbf{x}_k)$ and $\mathbb{V}[\mathcal{Y}^{PC}]$;
2. With the remaining $N_s - 1$ samples adjust a new PCE emulator \mathcal{Y}_k^{PC} ;
3. Compute the error between $\mathcal{Y}^{PC}(\mathbf{x}_k)$ and $\mathcal{Y}_k^{PC}(\mathbf{x}_k)$;
4. Restore the removed sample \mathbf{x}_k and take a different sample;
5. Repeat the previous steps N_s times and store the computed values;

The LOO test allows to compute the Q^2 coefficient, which is defined as:

$$Q^2 = 1 - \frac{Err_{LOO}}{\mathbb{V}[\mathcal{Y}^{PC}]}, \quad \text{with} \quad Err_{LOO} = \frac{1}{N_s} \sum_{k=1}^{N_s} (\mathcal{Y}^{PC}(\mathbf{x}_k) - \mathcal{Y}_k^{PC}(\mathbf{x}_k))^2, \quad (3.18)$$

and represents a normalized measure to check the accuracy of the surrogate model. The closest Q^2 is to the value of 1, the better agreement between the simulator and emulator.

An illustrative example: emulators vs. simulators

The next example compares the performances of emulators and the classical Monte Carlo method to perform forward UQ. Considering the model as the solution $u : [0, T] \rightarrow \mathbb{R}$ of the following differential equation:

$$\begin{aligned} \dot{u}(t) &= -a u(t), \quad \forall t \in [0, T], \\ u(0) &= l. \end{aligned}$$

Here we assumed that $\mathbf{x} = \{a, l\}$ are input parameters subjected to uncertainties characterized by $a \sim \mathcal{U}(0.1, 0.2)$ and $l \sim \mathcal{U}(1, 2)$. The UQ study was done using the classical Monte Carlo (MC) and a third-order PCE emulator. The UQ results presented in terms of expected value and standard deviation are shown in Figure 16.

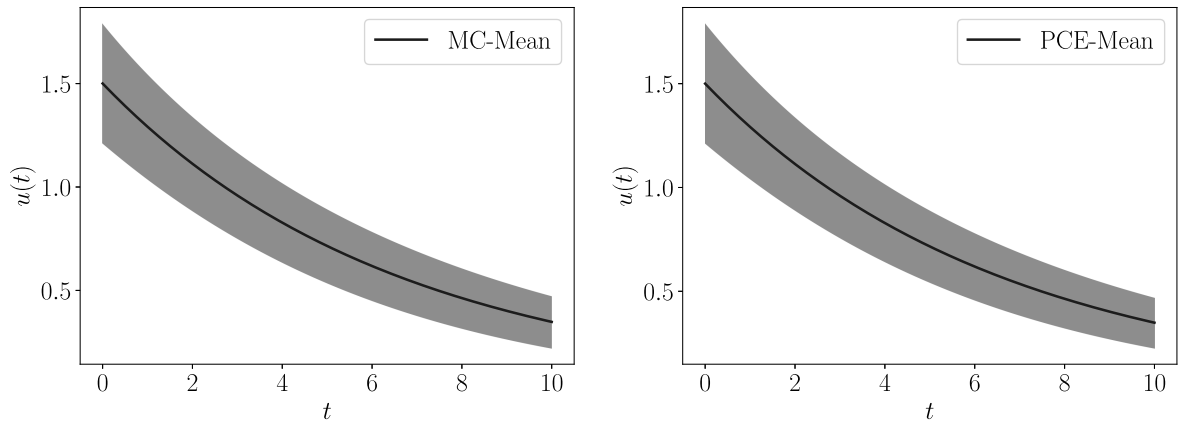


Figure 16 – Parametric uncertainty propagation study MC evaluations vs PCE. Solid lines represent the expected values and shaded regions represent the \pm standard deviation.

The PCE emulator associated to this problem is given by:

$$\begin{aligned} \mathcal{Y}^{PC} &= y_1 x_2^3 + y_2 x_1^3 + y_3 x_1 \cdot x_2^2 + y_4 x_1^2 \cdot x_2 + y_5 x_2^2 + \\ &\quad y_6 x_1^2 + y_7 x_1 \cdot x_2 + y_8 x_1 + y_9 x_2 + y_{10}, \quad \text{for a fixed } t \in [0, T]. \end{aligned}$$

The coordinates $\{y_i\}_{i=1}^{10}$, were determined solving the linear system from Equation (3.15). For this example, we performed 1000 forward evaluations of the model simulations, oversampling the corresponding minimal number of evaluations required to fit the PCE regression.

Both methods, MC and PCE, returns equivalent results in terms of propagated uncertainty. Figure 17 shows for each UQ method (MC and PCE) the relative error of expected value and standard deviations as functions of the total number of model evaluations. The fast convergence of the PCE emulator towards variations of the number of samples justifies the use of a surrogate instead of the model evaluation.

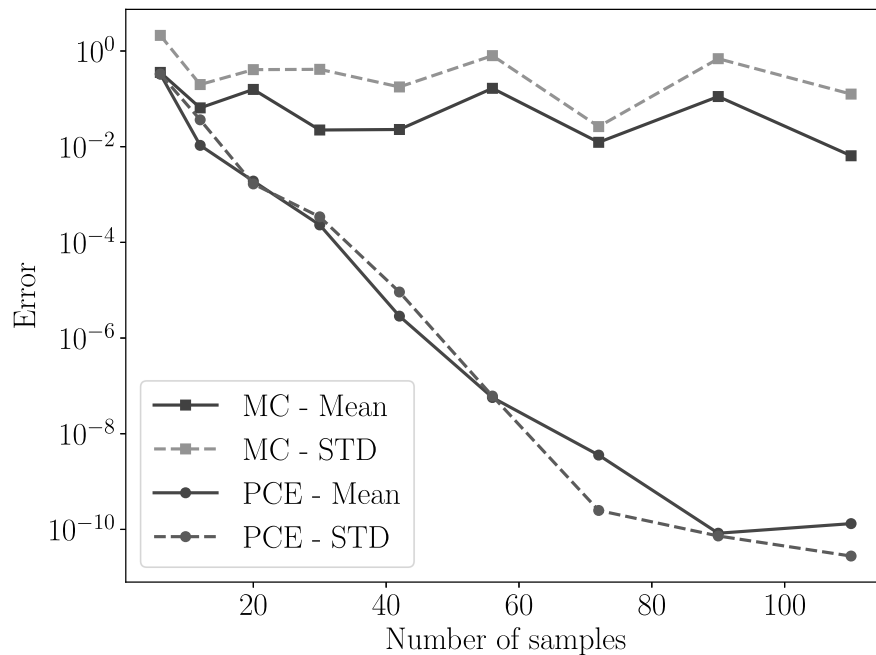


Figure 17 – Comparison between MC and PCE concerning the number of samples.

With the same number of evaluations, the PCE emulator always had minor variations in expected value and standard deviation than the MC method. In other words, PCE emulators require fewer model evaluations to obtain accurate results for UQ studies than the classical MC method. Further readings on the convergence of several methods for UQ studies can be found on [53, 144].

3.6 Computing Sobol' sensitivity indices

The variance $\mathbb{V}[\mathcal{Y}]$ of the output \mathcal{Y} is decomposed in the Sobol indices, as described in the work of Sobol [126, 127] and Saltelli [120]. It can be used to evaluate the influence of each uncertain parameter \mathbf{x} on the variance of \mathcal{Y} . We used variance-based SA in terms of the *main* and *total* Sobol indices, which are defined next.

The main Sobol index expresses how a specific uncertain input x_i directly contributes to the variance of the output \mathcal{Y} . The following expression gives it:

$$S_i = \frac{\mathbb{V}[\mathbb{E}[\mathcal{Y}|x_i]]}{\mathbb{V}[\mathcal{Y}]} \quad (3.19)$$

The total Sobol index estimates a decomposition of $\mathbb{V}[\mathcal{Y}]$ considering first and high-order interactions involving the i -*eth* uncertain input. The following expression gives it:

$$S_{Ti} = 1 - \frac{\mathbb{V}[\mathbb{E}[\mathcal{Y}|x_{-i}]]}{\mathbb{V}[\mathcal{Y}]}, \quad (3.20)$$

where x_{-i} denotes the set of all inputs except x_i .

The main Sobol index does not account for eventual interactions between two or more uncertain inputs. The total Sobol index captures these higher-order interactions. The execution of UQ and SA studies that were carried out employing PCE emulators are based on the `ChaosPy` library [47]. In some studies MC method was used based on the low computational cost to evaluate the model; there, we employed the Saltelli sampler implemented in the `SALib` library [63].

4 Uncertainty quantification and sensitivity analysis for relative permeability models

This chapter was first published in Journal of Petroleum Science and Engineering, 2020 by Elsevier. The content of this chapter is a reprint of the work of Valdez *et al.* [138], DOI: 0.1016/j.petrol.2020.107297. Reproduced with permission from Elsevier.

Computer simulations are usually employed for the prediction of oil reservoir performance under different extraction scenarios. Computational model parameters are adjusted to petrophysical properties of the reservoir and production data to forecast production profiles. However, some key features of these models, such as relative permeabilities of water and oil, are difficult to measure experimentally. As a consequence they can be considered a source of uncertainties, affecting the reliability of predictions. This work presents a study of uncertainty quantification and sensitivity analysis of different relative permeability models to assess the effects of input uncertainty on quantities of interest computed from a model of two-phase flow of water and oil. To explore different wettability regimes two different datasets were used, and two permeability models were employed. The probability distributions of parameters were estimated via the Markov Chain Monte Carlo method. Uncertainty propagation and sensitivity analyses were performed using the polynomial chaos expansion. The paper highlights output quantities that were most impacted by uncertain input data, and also the parameters which most contribute to the output variances.

4.1 Introduction

Mathematical and computational models are key tools to predict the effectiveness of enhanced oil recovery (EOR) techniques, including the reservoir performance and the production of hydrocarbons. The validation and reliability of these simulations depend on a set of rock-fluid properties required for tuning the computer model. Among all the model parameters, the relative permeabilities of the flowing phases (*e.g.* water and oil) are of utmost importance and play a central role in the physics of the reservoir. These functions are obtained experimentally by measuring the pressure drop at different points inside the sample for different physical conditions and then applying Darcy's law. Typically, the relative permeability curves are represented as functions of the wetting phase saturation.

Acquisition of accurate relative permeabilities data is critical and has been of interest in the petroleum industry and scientific community [101]. The inherent difficulty to experimentally determine water and oil relative permeabilities have been extensively reported in the literature [101, 14, 124]. Laboratory experiments to obtain relative permeabilities are complicated and time consuming [124]. Three methods are commonly used for measuring the relative permeability data: unsteady-state, steady-state and

centrifuge. These methods are discussed in terms of their disadvantages and limitations in [14]. The authors highlight the fact that these data are subject to errors and uncertainties. The errors in relative permeabilities estimated from displacement experiments under different operating conditions using the Johnson, Bossler and Naumann (JBN) method [71] were studied in [134, 135]. Their results indicate that errors were in the range of 0.2% to 15%. In most of the cases, errors were below 5%, except near the residual water saturation where they were higher. Also, the relative permeabilities are functions of the phase saturations and are affected by several other parameters, that may contain uncertainties as well [67].

Uncertainty quantification analysis can be used to study how the measurement errors propagate from input parameters to the model predictions. Recent works have investigated models for relative permeability, considering uncertainty in the experimental data. In particular, Moghadasi *et al.* [101] applied model identification criteria to rank and to assess relative permeability models for laboratory-scale experiments. Together with parameter estimation and model comparison, uncertainties of the estimated parameters are also considered in their analysis. Moreira *et al.* [125] applied the Markov Chain Monte Carlo (MCMC) method to estimate the parameters of the Corey relative permeability model [32] from laboratory scale data of a coreflood experiment. The mean values of the parameter distributions obtained by the MCMC method were used to estimate the pressure drop and oil production. In addition, the investigation can be improved by the sensitivity analysis (SA), which studies the effects of input parameters on the variance of the output quantities. For example, Yoshida *et al.* [147] performed a sensitivity analysis with Monte Carlo simulations of a Corey-type relative permeability model in the context of CO₂ injection in reservoirs. Other studies have applied sensitivity analysis for EOR techniques [103, 108].

The main contribution of this work is the investigation of a new method for performing uncertainty quantification (UQ) and sensitivity analysis (SA) of a model of two-phase flow in porous media based on a polynomial surrogate model. The Buckley-Leverett equation is used as the prototype model for studies of water-oil displacement at the core-scale. The proposed scheme determines the probability distribution functions for the parameters required in the UQ and SA analyses using the Markov chain Monte Carlo method. We demonstrate the method in a detailed UQ and SA study of two relative permeability models [25, 92] commonly used for two-phase flow in a porous medium. Given the input parameter distributions, UQ is performed using polynomial chaos expansions (PCE) [145, 55], whereas SA is achieved using variance-based Sobol indices [127, 120]. The scheme is computationally efficient and requires fewer model evaluations than the classical Monte Carlo method, and to the best of our knowledge has not been applied in this context.

The remainder of this text is organized as follows. In Section 4.2 the model for

two-phase flow in porous media, the methods for UQ and SA, input parameters and quantities of interest are described. In Section 4.3 the results of the analyses are presented, followed by discussion and conclusions in sections 4.4 and 4.5, respectively.

4.2 Methods

4.2.1 Two-phase flow model

The water-oil displacement in a petroleum reservoir can be approximated with the Buckley-Leverett (BL) model [19]. This model assumes the following hypothesis: the porous medium is fully saturated with immiscible and incompressible fluids. The interface between the fluids remains chemically inactive, the flow is horizontal and capillary effects are neglected. Following [7] the two-phase transport in a porous medium using the BL model can be described by:

$$\frac{\partial S_w}{\partial t} + \frac{q}{\phi a} \frac{\partial}{\partial x} (f) = 0, \quad \text{in } \Omega \times [0, T], \quad (4.1)$$

where q is the total influx, a is the core sample cross section area, ϕ matrix porosity, $S_w = S_w(x, t)$ denotes the water saturation and f expresses the fractional flow function. The fractional flow function is defined as:

$$f = \frac{\kappa_{rw}}{\kappa_{rw} + \left(\frac{\mu_w}{\mu_o}\right) \kappa_{ro}}, \quad (4.2)$$

where $\kappa_{rw} = \kappa_{rw}(S_w)$ and $\kappa_{ro} = \kappa_{ro}(S_w)$ are the water- and oil-phase relative permeabilities, respectively. Here, μ_w and μ_o denote the water and oil viscosities, respectively. Finally, equation (4.1) is supplemented with the following initial conditions:

$$S_w(x, 0) = S_{w0}, \quad (4.3)$$

whereas the following boundary conditions are assumed:

$$S_w(0, t) = 1.0 - S_{o0}, \quad (4.4)$$

that is, the maximum of water is injected at a constant flow rate of q . Within this context semi-analytic solutions are obtained for equation (4.1) employing the method of characteristics following Marle [99] and Welge [139].

4.2.2 Relative permeability models

Two widely used relative permeability models were considered for the Buckley-Leverett equation (4.1): Chierici's model [25] and the LET model [92].

The Chierici's relative permeability model was proposed by [25, 26] and is represented with the following expressions:

$$\kappa_{rw} = \kappa_w^0 e^{-B \left(\frac{S_w - S_{w0}}{1 - S_w - S_{o0}} \right)^{-M}}, \quad \kappa_{ro} = \kappa_o^0 e^{-A \left(\frac{S_w - S_{w0}}{1 - S_w - S_{o0}} \right)^L} \quad (4.5)$$

where A , L , B and M are parameters for the relative permeabilities.

The LET relative permeability model was proposed by Lomeland, Ebeltoft and Thomas [92] and was extensively studied [93, 91, 37, 38]. The relative permeabilities in this model are given by:

$$\kappa_{rw} = \kappa_w^0 \frac{S_{we}^{L_w}}{S_{we}^{L_w} + E_w (1 - S_{we})^{T_w}}, \quad \kappa_{ro} = \kappa_o^0 \frac{(1 - S_{we})^{L_o}}{(1 - S_{we})^{L_o} + E_o S_{we}^{T_o}}, \quad (4.6)$$

where L_w , E_w , T_w , L_o , E_o , and T_o are parameters of the model where w indicates the water phase and o indicates the oil phase. Here S_{we} is the effective water saturation given by

$$S_{we} = \frac{S_w - S_{w0}}{1 - S_{w0} - S_{o0}}, \quad (4.7)$$

where S_{w0} denotes the connate water saturation and S_{o0} the residual oil saturation. In addition to this, κ_o^0 is the oil relative permeability at the connate water saturation and κ_w^0 is the water relative permeability at the residual oil saturation.

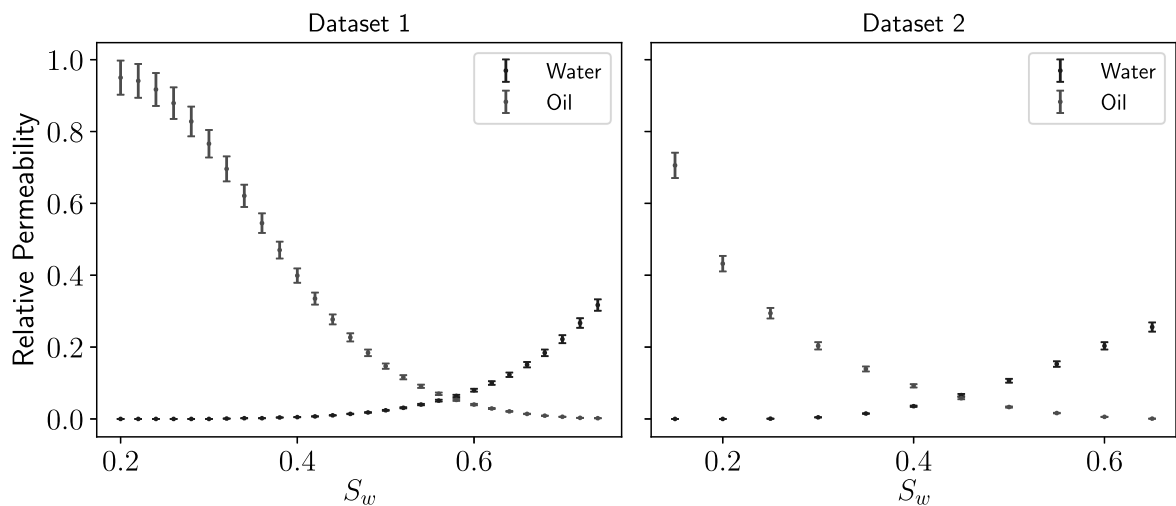
4.2.3 Datasets

The uncertainty quantification and sensitivity analyses were carried out with data calibrated from two different datasets. In this work, we considered experimental and synthetical core flooding data for water and oil available in the literature [90, 56]. The physical and wettability properties of each dataset, referred hereto as dataset 1 and 2 are summarized in Table 2.

Dataset 1 was obtained from core flooding experiments [94] and is freely available at [90]. Dataset 2 was extracted from specialized literature [56]. Figure 18 shows the water and oil relative permeability as a function of water saturation for each dataset. The error analysis of relative permeability presented in [134] showed that most of the errors were below 5%. Therefore, for the analyses presented in this work, error measurements were assumed as normal distributions with 5% of the coefficient of variation (CoV).

Table 2 – Petrophysical properties of the two core samples [90, 56].

Property	Dataset 1	Dataset 2
Porosity	0.27	0.2062
Oil absolute permeability (mD)	1042	303
Water viscosity (cp)	0.306	0.65
Oil viscosity (cp)	0.670	1.25
Core length (m)	0.1174	1.22
Core diameter (m)	0.0377	0.05
Inflow rate (ml/min)	0.1	1
Wettability regime	water-wet	oil-wet
Connate water saturation (S_{w0})	0.20	0.15
Residual oil saturation (S_{o0})	0.26	0.35

Figure 18 – Relative permeability values for water κ_{rw} and oil κ_{ro} as a function of water saturation S_w for the two datasets from the literature [90, 56].

4.2.4 Input Parameters and Quantities of Interest

To perform uncertainty quantification and sensitivity analyses studies we must define a set of input parameters θ and relevant quantities of interest (QoIs). For Chierici's model we considered the following input parameters $\theta_C = \{B, M, A, L\}$, whereas the following input parameters $\theta_{LET} = \{L_w, E_w, T_w, L_o, E_o, T_o\}$ were considered for LET model. The following QoIs were considered in this study: relative permeability crossing point, shock front saturation and displaced oil at a fixed time, which are denoted by S_{cpt} , S_f and $V(t)$, respectively. These output quantities are defined next.

The *relative permeability crossing point* S_{cpt} corresponds to the water saturation

that satisfies the following equation:

$$\kappa_{rw}(S_{cpt}) - \kappa_{ro}(S_{cpt}) = 0. \quad (4.8)$$

The *shock front saturation* S_f is computed by Welge's method [139] as:

$$\frac{\partial f(S_f)}{\partial S_w} (S_f - S_{w0}) - f(S_f) = 0. \quad (4.9)$$

The *produced oil at a fixed time* $V(t)$, as defined in [7], is the result of evaluating the following integral:

$$V(t) = a \int_0^t q (1 - f(S_w(L, \tau))) d\tau, \quad (4.10)$$

where $f(S_w(L, \tau))$ represents the fractional flow function evaluated at any time instant τ and at the position $x = L$ which, corresponds to the size of the core sample.

The datasets and the simulations performed in this work focus on core-scale experiments. QoIs used in this work were chosen considering their relevance to both core-scale and field-scale experiments. For instance, the crossing point saturation S_{cpt} and the shock front saturation S_f are essential indicators of the performance for both mature or new reservoirs.

4.2.5 Parameter and distribution estimation

For each relative permeability model (Chierici and LET) we performed a parameter estimation based on the presented datasets using the Markov Chain Monte Carlo (MCMC) method [17]. The MCMC method attempts to find the most probable parameter set to fit the model to a given dataset, as well as a characterization of the parameter uncertainty by means of a posterior distribution of parameters.

This step was carried out using the MCMC method implemented in `emcee` library [54]. The Levenberg-Marquardt method, implemented in the `lmfit` [107] package, was used to obtain an initial guess for the relative permeability model parameters required for the MCMC.

Assuming $\boldsymbol{\theta}$ as the relative permeability model parameters and D as the dataset, MCMC tries to estimate:

$$\mathbb{P}(\boldsymbol{\theta}|D) = \frac{\mathbb{P}(D|\boldsymbol{\theta}) \mathbb{P}(\boldsymbol{\theta})}{\mathbb{P}(D)}, \quad (4.11)$$

where $\mathbb{P}(\boldsymbol{\theta})$ denotes the *prior* knowledge about the input parameters $\boldsymbol{\theta}$ as a joint probability distribution, $\mathbb{P}(D|\boldsymbol{\theta})$ is the likelihood function and $\mathbb{P}(D)$ is the evidence that the data was generated by this model. In equation (4.11) we adopted the following likelihood function:

$$\ln(\mathbb{P}(D|\boldsymbol{\theta})) = -0.5 \sum_i^{N_d} \left[\left(\frac{D^i - y^i(\boldsymbol{\theta})}{\sigma^i} \right)^2 + 2 \log(\sigma^i) \right], \quad (4.12)$$

where N_d represents the size of the dataset, σ^i represents the error values, and $y^i(\boldsymbol{\theta})$ is an entry of the vector representing the relative permeability model evaluated at the sample parameters $\boldsymbol{\theta}$.

The MCMC method requires the definition of a prior distribution, which in this work was considered as a flat prior distributions [66]:

$$\ln(\mathbb{P}(\boldsymbol{\theta})) = \begin{cases} 0 & \text{if all entries of } \boldsymbol{\theta} \in \mathbb{R} > 0, \\ -\infty & \text{elsewhere.} \end{cases} \quad (4.13)$$

4.2.6 Uncertainty quantification

The method used to carry out the forward UQ study was based on the Polynomial Chaos Expansion (PCE), which expresses any output quantity as an orthogonal polynomial regression that depends on the uncertain input model parameters.

The uncertain input vector $\boldsymbol{\theta} = [\theta_1, \dots, \theta_{N_p}]$ is a multivariate random variable defined on the sample space Δ . In addition, we assume that the inputs θ_i are independent and identically distributed. The joint probability distribution function is given by $\pi(\boldsymbol{\theta}) = \prod_i^{N_p} \pi_i(\theta_i)$, where N_p represents the number of uncertain parameters and $\pi_i(\theta_i)$ the marginal probability distribution functions.

For any output quantity $\mathcal{Y} = \{S_{cpt}, S_f, V(t)\}$ the associated PCE emulator is written in terms of a truncated polynomial expansion. Following [106, 55] the basis used to perform the expansion is an orthonormal basis that yields the next expression:

$$\mathcal{Y}^{PC} = \sum_{i=0}^{N-1} \psi_i(\boldsymbol{\theta}) y_i = \sum_{\boldsymbol{\alpha} \in \mathcal{A}} \psi_{\boldsymbol{\alpha}}(\boldsymbol{\theta}) y_{\boldsymbol{\alpha}}, \quad (4.14)$$

where $\psi_i(\boldsymbol{\theta})$ or $\psi_{\boldsymbol{\alpha}}(\boldsymbol{\theta})$ represents the orthonormal basis and \mathcal{Y}^{PC} is the approximation of the random response of the QoI. Equation (4.14) shows two representations of the same polynomial expansion, where \mathcal{A} features the set of multi-indices $\boldsymbol{\alpha} = \{\alpha_1, \alpha_2, \dots, \alpha_{N_p}\}$. The number of terms N considered in the expansion is a function of the number of uncertain inputs and the polynomial degree P_d given by $N = \frac{(N_p + P_d)!}{P_d! N_p!}$.

The coordinates y_i or $y_{\boldsymbol{\alpha}}$ that determine the polynomial expansion written in equation (4.14) are obtained minimizing the difference between \mathcal{Y} and \mathcal{Y}^{PC} . This is achieved by solving the following least squares minimization problem:

$$y_{\boldsymbol{\alpha}} = \arg \min_{y_{\boldsymbol{\alpha}}} \left(\mathcal{Y} - \sum_{\boldsymbol{\alpha} \in \mathcal{A}} \psi_{\boldsymbol{\alpha}}(\boldsymbol{\theta}) y_{\boldsymbol{\alpha}} \right)^2. \quad (4.15)$$

The size N_s of this problem should be equal to or greater than the number of coefficients N of the polynomial chaos expansion.

Increasing the polynomial order P_d can improve the performance of the surrogate model but at the expense of high computational cost. A typical procedure to improve the

accuracy of the polynomial surrogate model obtained with PCE is to consider a number of samples N_s larger than the minimum N required for determining the coefficients of the polynomial [68]. Typically a number of samples $N_s = kN$ with k is a positive integer factor is used.

After the coordinates y_{α} are determined, they are used to construct the PCE emulator. Then, the evaluation of statistical moments like the expected value and variance of \mathcal{Y} are computed as:

$$\mathbb{E}[\mathcal{Y}] = \int_{\Delta} \mathcal{Y} \pi(\boldsymbol{\theta}) d\Delta = y_0, \quad (4.16)$$

$$\mathbb{V}[\mathcal{Y}] = \int_{\Delta} (\mathcal{Y} - \mathbb{E}[\mathcal{Y}])^2 \pi(\boldsymbol{\theta}) d\Delta = \sum_{\substack{\alpha \in A \\ \alpha \neq 0}} y_{\alpha}^2. \quad (4.17)$$

The coefficient of variations (CoV) defined as the ratio of standard deviation and expected value $\text{CoV}(\mathcal{Y}) = 100\% \times \sqrt{\mathbb{V}[\mathcal{Y}]/\mathbb{E}[\mathcal{Y}]}$, was also used as a metric of variability.

4.2.7 Sensitivity analysis

Sensitivity analysis is used to assess how the input parameters $\theta_i \in \boldsymbol{\theta}$ and also interactions between them contribute to a particular output quantity \mathcal{Y} . This type of analysis allows recognizing input parameters that do not affect the variability of a chosen QoI, and input parameters that significantly contribute to variations of the QoI.

Global sensitivity analysis was performed using variance based Sobol sensitivity indices [127, 120]. The first order Sobol index (also known as main Sobol index), expresses how a certain uncertain input θ_i directly contributes to the variance of the output \mathcal{Y} . It is given by the following expression:

$$S_i = \frac{\mathbb{V}[\mathbb{E}[\mathcal{Y}|\theta_i]]}{\mathbb{V}[\mathcal{Y}]}. \quad (4.18)$$

The first order Sobol index neglects eventual interactions between two or more different uncertain inputs. To estimate the changes on $\mathbb{V}[\mathcal{Y}]$ considering first and high-order interactions of the i -th uncertain input, the total Sobol index [120] is used, which is given by:

$$S_{Ti} = 1 - \frac{\mathbb{V}[\mathbb{E}[\mathcal{Y}|\theta_{-i}]]}{\mathbb{V}[\mathcal{Y}]}, \quad (4.19)$$

where θ_{-i} denotes the set of all inputs except θ_i .

4.2.8 Calibration of the surrogate model

The performance of the PCE surrogate model for each output quantity \mathcal{Y} depends on the chosen polynomial degree P_d as well as on the number of samples N_s used. To verify the surrogate model performance we employed the leave-one-out (LOO) cross validation

test [55] to check if a specific combination of polynomial degree and the number of samples results in an accurate model. The LOO test can be summarized in the following steps:

- From the N_s samples, take one sample $\boldsymbol{\theta}_k$, evaluate $\mathcal{Y}(\boldsymbol{\theta}_k)$ and $\mathbb{V}[\mathcal{Y}]$;
- With the other $N_s - 1$ samples adjust a new PCE emulator \mathcal{Y}_k ;
- Compute the error between $\mathcal{Y}(\boldsymbol{\theta}_k)$ and $\mathcal{Y}_k(\boldsymbol{\theta}_k)$;
- Restore the removed sample $\boldsymbol{\theta}_k$ and take a different sample;
- Repeat the previous steps N_s times and store the computed values;

Thus, the LOO error is defined as:

$$Err_{LOO} = \frac{1}{N_s} \sum_{k=1}^{N_s} (\mathcal{Y}(\boldsymbol{\theta}_k) - \mathcal{Y}_k(\boldsymbol{\theta}_k))^2, \quad (4.20)$$

while the Q^2 coefficient is given by:

$$Q^2 = 1 - \frac{Err_{LOO}}{\mathbb{V}[\mathcal{Y}]}, \quad (4.21)$$

which is a normalized measure to check the accuracy of the surrogate model. The closest Q^2 is to the value of 1, the better is the performance of the model.

4.2.9 Computational implementation

The UQ and SA studies were performed employing the open source library `ChaosPy` developed by [47]. The solution of the BL equation, as well as the computation of the QoIs were implemented in an *in-house* code.

To summarize, we present the computational workflow used for the numerical experiments carried out in this work. The procedure for performing the experiments with each dataset can be summarized as follows:

- Compute an initial estimate of Chierici's and LET model parameters for a given dataset using Levenberg-Marquardt method;
- With the given initial estimate, perform the MCMC analysis to obtain the parameter estimates and posterior distribution of the model parameters;
- Construct the PCE surrogate model to perform UQ and SA studies using the probability distributions obtained via MCMC;
- Check if the surrogate model is accurate enough; if not, increase the number of samples N_s or polynomial degree P_d in the previous step;

- Study the parametric uncertainty propagation analyzing the variability of the output quantities;
- Compute Sobol sensitivity indices for each output quantity.

4.3 Results

4.3.1 Parameter estimation using MCMC

The parameter estimation and determination of the posterior distribution of the parameters were obtained with the MCMC method with a chain of length 32000. The length of the chain summarizes the 250 number of iterations performed by the 128 random walkers for each model parameter, for both datasets. With this settings the MCMC estimated the parameters in a total of 8 hours of execution time.

Figures 19 and 20 present the histogram of the marginalized parameter distribution for each model, as well as projections of the posterior distributions for pairs of variables, for dataset 1 and 2, respectively. For dataset 1, the MCMC results presented Gaussian shapes for the posterior distributions of the parameters for both Chierici's and LET models. For dataset 2 the results indicated that Chierici's model parameters remain with Gaussian distributions as well as the LET model, with the exception of the E_w parameter which presented a log-normal distribution.

With respect to Chierici's model, no correlation between parameters B and M (water permeabilities) was observed, whereas small correlations between A and L for the oil permeabilities can be observed considering dataset 1. For the dataset 2, small correlations were observed for both pairs of variables $\{B, M\}$ and $\{A, L\}$ from Chierici's model. For the LET model strong correlations between the following pairs of parameters (E_w, L_w) , (E_w, T_w) , (E_o, L_o) and (E_o, T_o) were observed from the MCMC results for both datasets.

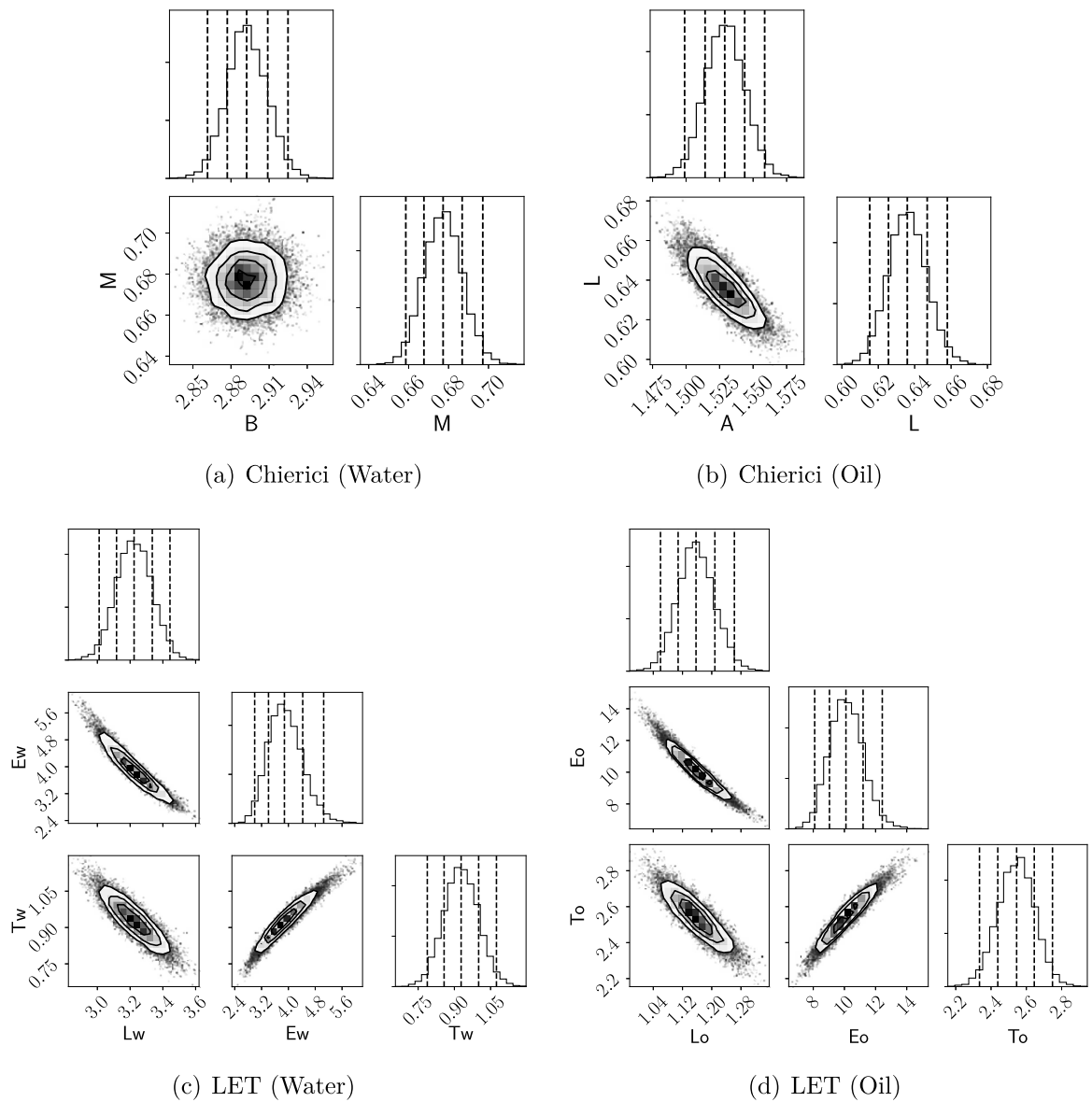


Figure 19 – Summary of parameter values from the results of MCMC for Chierici’s (panels (a) and (b)) and LET (panels (c) and (d)) models considering dataset 1. The panels on the diagonal show the histograms of each model parameter, with dashed vertical lines to indicate the 2th, 16th, 50th, 84th and 98th percentiles of the samples in the marginalized distributions. The off-diagonal panels show projections of the posterior probability distributions of each pair of parameters.

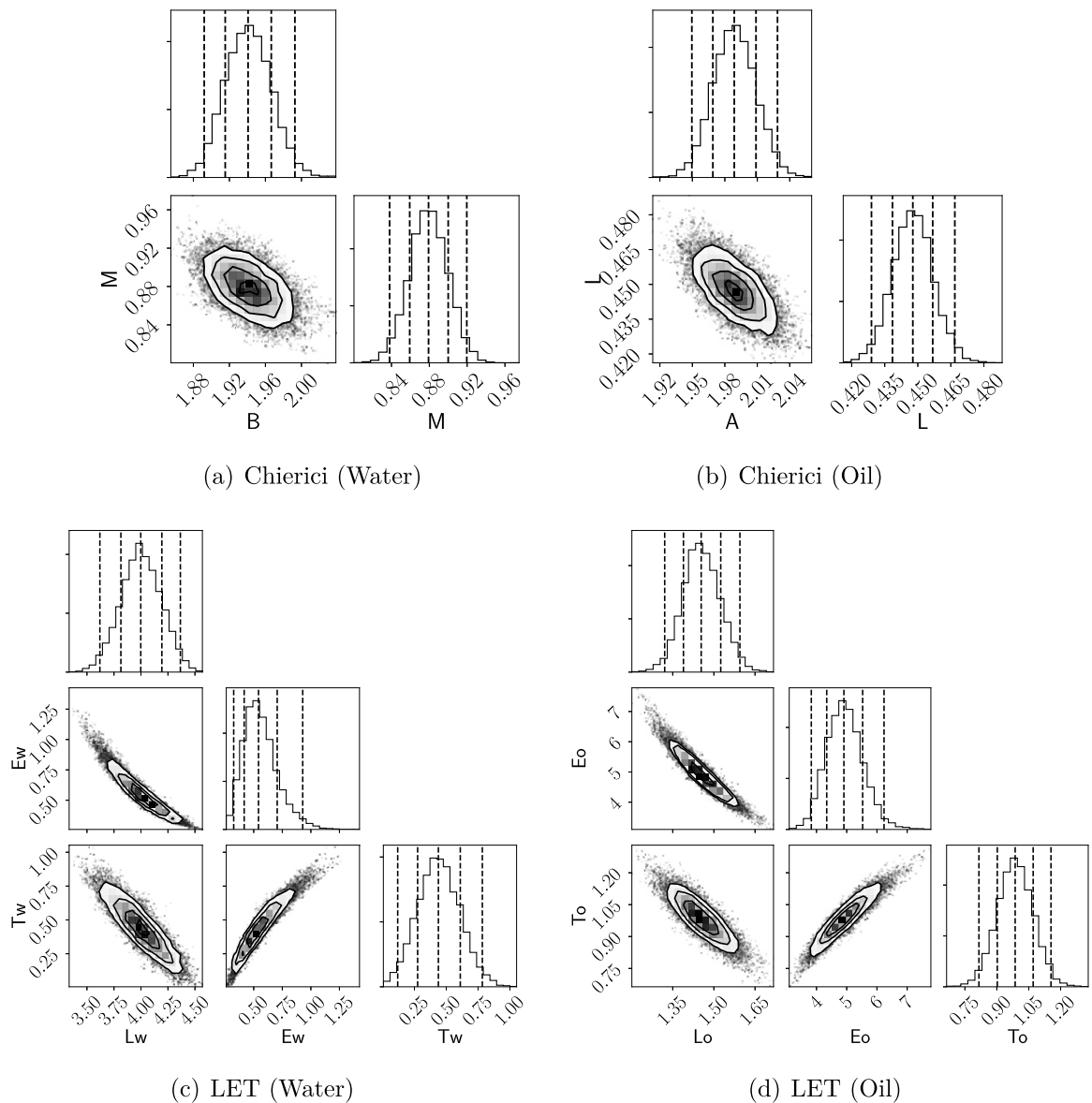


Figure 20 – Summary of parameter values from the results of MCMC for Chierici’s (panels (a) and (b)) and LET (panels (c) and (d)) models considering dataset 2. The panels on the diagonal show the histograms of each model parameter, with dashed vertical lines to indicate the 2th, 16th, 50th, 84th and 98th percentiles of the samples in the marginalized distributions. The off-diagonal panels show projections of the posterior probability distributions of each pair of parameters.

Table 3 presents a compilation of the posterior probability distribution functions for each permeability model considering the two datasets.

Dataset 1 contains a change of curvature for the oil relative permeability curve and is characterized by an oil-wet regime, whereas dataset 2 is characterized by a water-wet regime and does not present a change of curvature. As shown in Figures 19 and 20, and summarized in Table 3, the MCMC method results in similar-shaped posterior distributions for Chierici’s model using the two datasets. For the LET model, however, different posterior

distributions were obtained for the datasets, where for the dataset 2 the E_w parameter presented a log-normal distribution while the other parameters were characterized by normal distributions.

Table 3 – Calibrated posterior distribution of model parameters considering the different datasets. For each case, minimum, maximum and the corresponding normal (or log-normal) posterior probability distribution is presented in terms of mean μ and standard deviation σ as $\mathcal{N}(\mu, \sigma)$.

Dataset 1				
Model	Parameter	Minimum	Maximum	Posterior distribution
Chierici	A	1.47	1.59	$\mathcal{N}(1.529, 0.014)$
	L	0.60	0.68	$\mathcal{N}(0.637, 0.010)$
	B	2.83	2.96	$\mathcal{N}(2.891, 0.015)$
	M	0.64	0.72	$\mathcal{N}(0.678, 0.009)$
LET	L_w	2.82	3.62	$\mathcal{N}(3.225, 0.108)$
	E_w	2.32	6.21	$\mathcal{N}(3.919, 0.516)$
	T_w	0.66	1.20	$\mathcal{N}(0.928, 0.072)$
	L_o	0.98	1.36	$\mathcal{N}(1.158, 0.050)$
	E_o	6.43	15.38	$\mathcal{N}(10.13, 1.092)$
	T_o	2.16	2.95	$\mathcal{N}(2.542, 0.103)$
Dataset 2				
Model	Parameter	Minimum	Maximum	Posterior distribution
Chierici	A	1.91	2.06	$\mathcal{N}(1.987, 0.019)$
	L	0.42	0.49	$\mathcal{N}(0.447, 0.009)$
	B	1.86	2.04	$\mathcal{N}(1.941, 0.025)$
	M	0.80	0.97	$\mathcal{N}(0.879, 0.020)$
LET	L_w	3.34	4.57	$\mathcal{N}(4.000, 0.187)$
	E_w	0.26	1.43	$\ln E_w \sim \mathcal{N}(-0.736, 0.296)$
	T_w	0.01	1.05	$\mathcal{N}(0.441, 0.165)$
	L_o	1.20	1.72	$\mathcal{N}(1.455, 0.684)$
	E_o	3.10	7.78	$\mathcal{N}(4.938, 0.605)$
	T_o	0.66	1.33	$\mathcal{N}(0.986, 0.084)$

4.3.2 Surrogate model calibration

The parameter distributions presented before were used to perform UQ and SA studies using PCE surrogate models. The calibration of each PCE emulator was verified employing the LOO cross validation test. It was verified that PCE emulators characterized by second order polynomials adjusted with 2 times the minimal number of samples to perform the regressions were accurate enough. Using these settings a total of $N_s = 30$ and $N_s = 56$ samples for Chierici and LET models were generated. The Buckley-Leverett solver takes about 0.28 and 0.45 seconds to execute each sample for Chierici and LET

models, respectively. For both datasets and relative permeability models values of the Q^2 coefficient for the output quantities were: $Q_{S_{cpt}}^2 = 1.0$, $Q_{S_f}^2 = 1.0$ and $Q_{V(1)}^2 = 0.999$.

4.3.3 Forward uncertainty quantification

The emulators used in this study were PCE regressions calibrated as described in the previous section, where the uncertainties of the input parameters are those characterized in Table 3.

We evaluated the impact of input uncertainties on the behavior of the normalized oil-production and water-cut curves for both relative permeability models as shown in Figure 21. For both datasets the expected values for the oil-production and water-cut present some relevant differences between the relative permeability models. One can also observe that the 90% prediction interval estimated by the LET model is greater than the one for Chierici's model in both datasets.

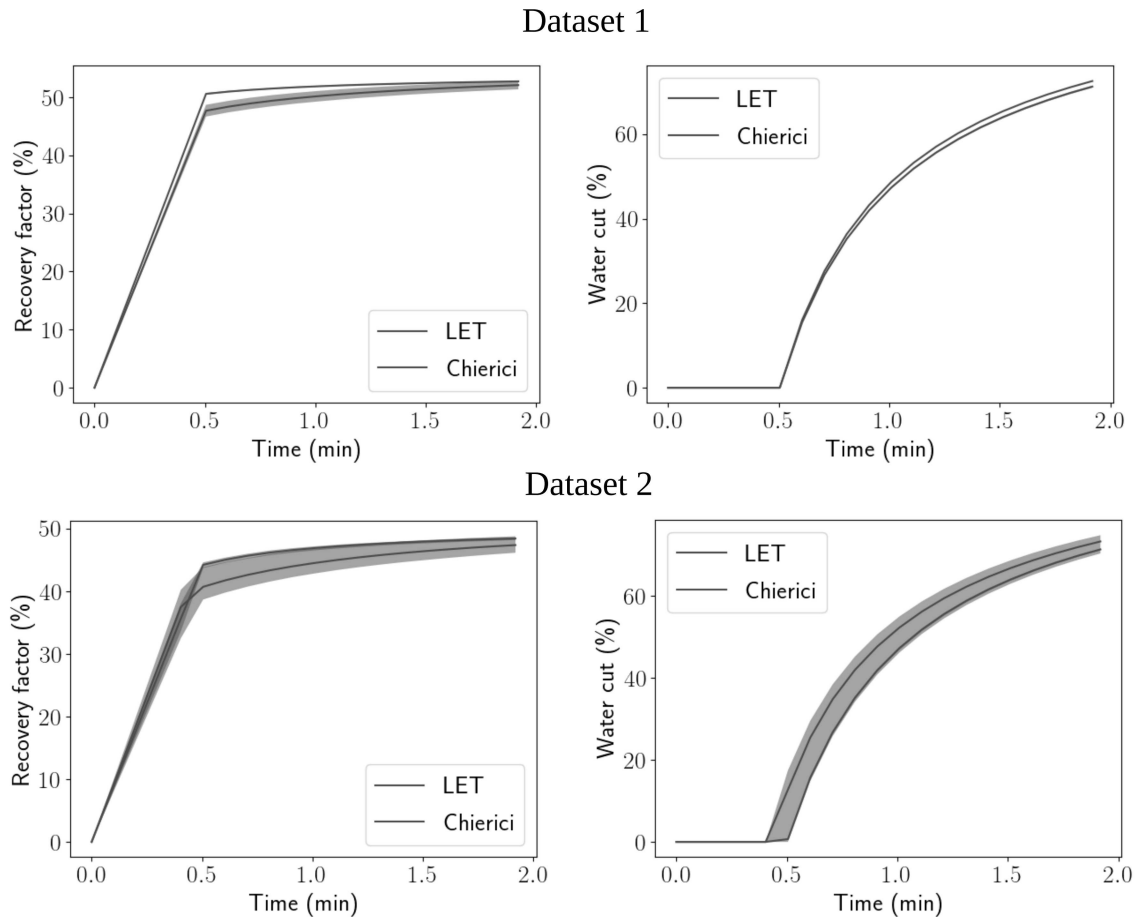


Figure 21 – Parametric uncertainty propagation study of recovery factors (oil and water cut). Solid lines represent the expected values and shaded regions represent the 90% prediction interval.

The impact of uncertainty on the selected QoIs (relative permeability crossing point S_{cpt} , produced oil V at time $t = 1$ and the shock front saturation S_f), in terms of

expected value (μ), standard deviation (σ) and coefficient of variation (CoV) are presented in Table 4 for all datasets considered.

Table 4 – Uncertainty propagation in terms of expected value (μ), standard deviation (σ) coefficient of variation (CoV) for the QoIs = $\{S_{cpt}, S_f, V(1)\}$.

Model	Dataset	S_{cpt}			S_f			$V(1)$		
		μ	σ	CoV (%)	μ	σ	CoV (%)	μ	σ	CoV (%)
Chierici	1	0.58	0.0016	0.27	0.65	0.0021	0.32	0.52	0.0007	0.13
	2	0.45	0.0018	0.39	0.50	0.0024	0.49	0.46	0.0012	0.25
LET	1	0.57	0.0074	1.29	0.63	0.0087	1.36	0.50	0.0053	1.05
	2	0.44	0.0135	3.09	0.48	0.0177	3.66	0.44	0.0095	2.16

First note that the range of variability for all the QoIs studied is upper bounded by 3.1% of CoV. As a matter of fact, the measurement errors were assumed to have 5% of CoV. In particular, we note that the crossing points between relative permeabilities S_{cpt} were not affected by the uncertainty propagation process. Indeed, for dataset 1 the mean value of S_{cpt} was greater than 0.5 which is consistent with a water-wet regime. For the dataset 2 the mean value of S_{cpt} was smaller than 0.5, indicating a oil-wet regime.

4.3.4 Sensitivity analysis

Figure 22 shows the Sobol indices for all QoIs considered when adopting both permeability models, where the uncertain parameters correspond to the distributions reported in Table 3 using dataset 1.

For all output quantities, parameters A and L of Chierici’s model have significant sensitivity indices. Concerning the produced oil at a fixed time, significant higher-order interactions between all parameters of Chierici’s model can be observed from the total Sobol indices.

The analysis for the LET model revealed that for S_{cpt} and S_f the E_o and E_w parameters had the highest Sobol indices, which conforms with the literature [38], since the E parameter of the LET model controls the intermediate height of the relative permeability curve. For the oil-production at $t = 1$ ($V(1)$) the parameter E_o achieved the highest main Sobol sensitivity index.

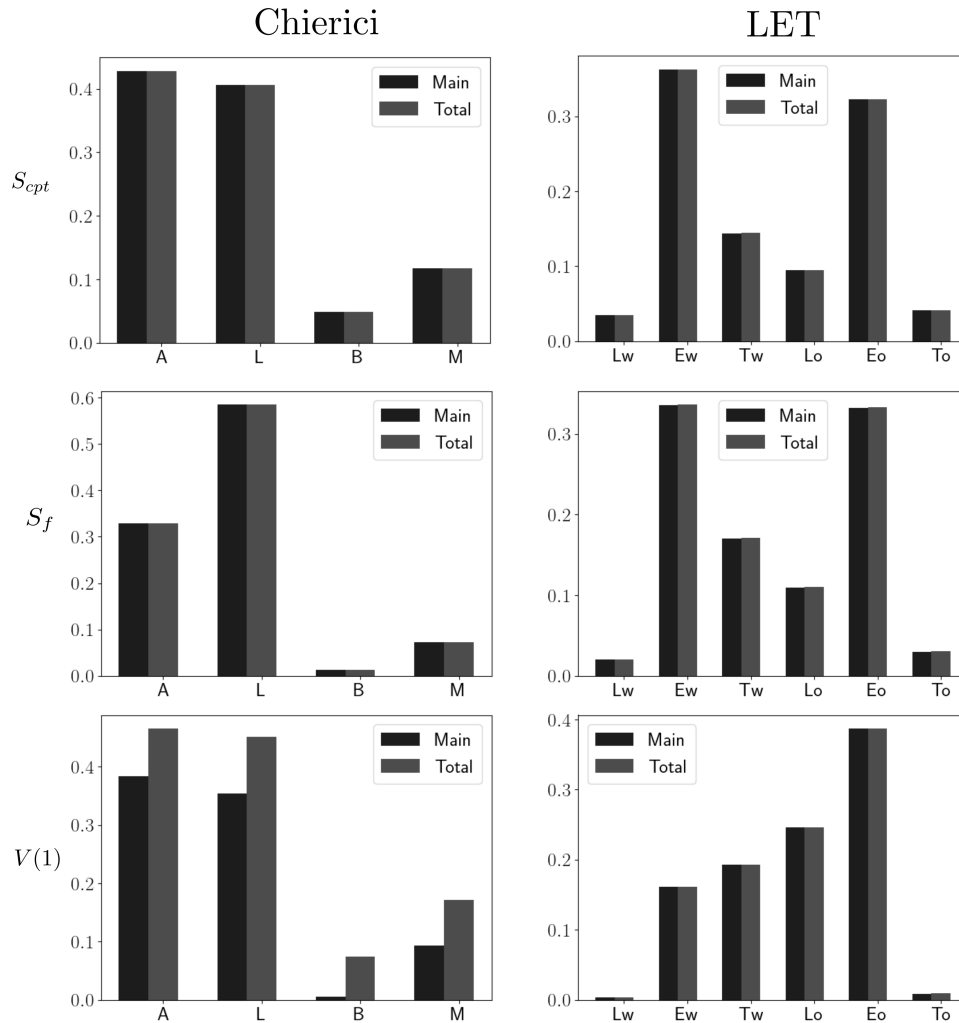


Figure 22 – Variance based SA results for all QoIs considering the dataset 1.

Next, we performed a sensitivity analysis for the oil-wet dataset 2. Figure 23 presents the Sobol indices for all output quantities considered. For Chierici’s model, the A parameter of the oil relative permeability curve clearly emerged as the one with the highest sensitivity index value for all QoIs. For the dataset 2 case, it is important to note that parameters B and M also significantly contributed to S_{cpt} and S_f , whereas the parameter L contributed significantly to $V(1)$.

For the LET model, parameters E_w , T_w , and E_o influence the outputs S_{cpt} and S_f , with a significant contribution from E_w . For the output $V(1)$, in addition to these three parameters, L_o has also some impact on the produced oil. For this QoI, we observe again some higher-order interactions between the parameters of the two relative permeability models.

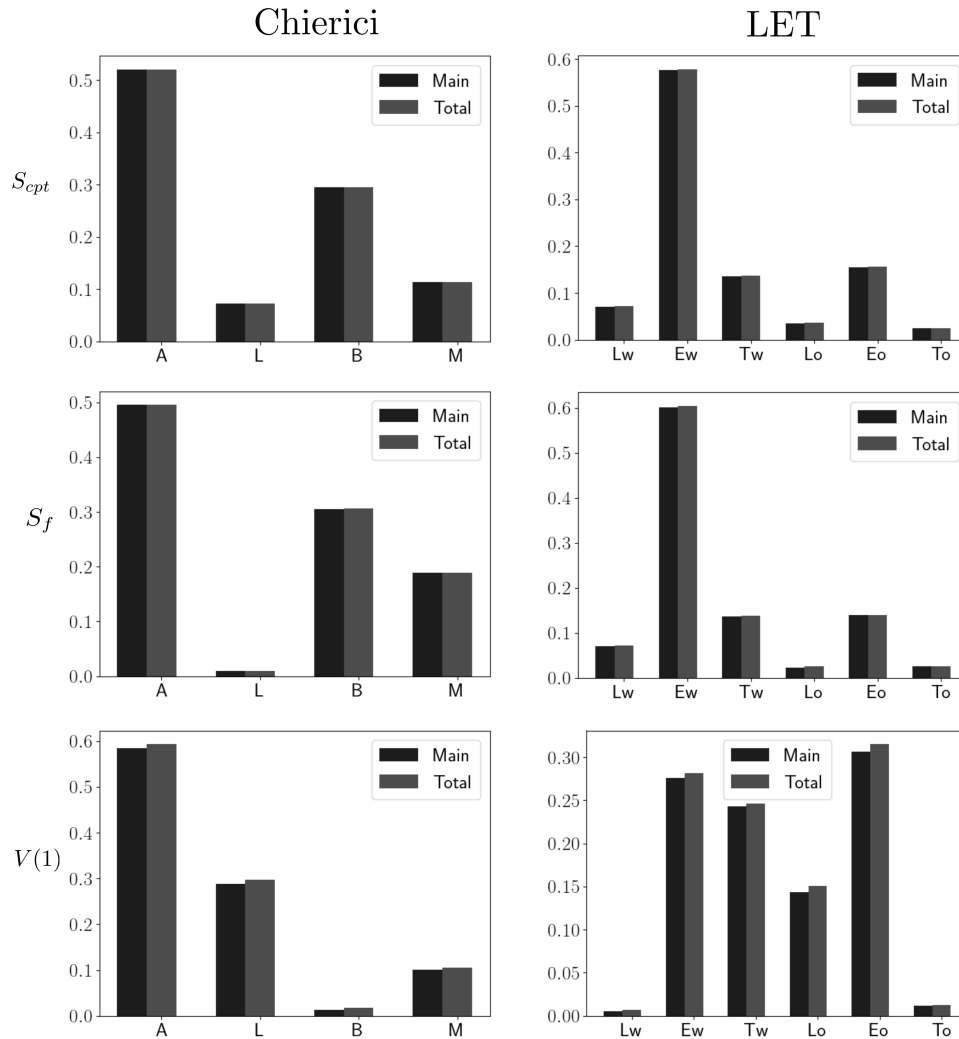


Figure 23 – Variance based SA results for all QoIs considering the dataset 2.

4.3.5 Effects of relative permeability endpoints

In the previous experiments relative permeability endpoints κ_w^0 and κ_o^0 which are also part of Chierici's and LET models, as well as physical parameters like the residual water and oil saturations S_{w0} and S_{o0} , respectively, were not considered for the UQ and SA analyses. To assess the effects of relative permeability endpoints we performed an experiment considering κ_w^0 , κ_o^0 , S_{w0} , and S_{o0} as uncertain input parameters. Due to the difficulty in estimating the posterior PDFs for these parameters using the MCMC method, a different approach was performed for this study. Normal distributions with mean values from Table 3 and 1% of CoV were assumed for all input parameters of the relative permeability models.

The results in terms of uncertainty propagation for all quantities of interest, recovered oil, and water cut profiles are qualitatively similar to the ones presented in Table 4 and Figure 21.

The sensitivity indices computed for this study revealed a much more clear impact

of the endpoint parameters on the QoIs for both datasets. For instance, in both models, the residual oil saturation S_{o0} is the parameter which most impacts all outputs, achieving sensitivity values greater than 0.5 in all cases. Specifically for the produced oil, the residual water saturation S_{w0} also appears as an important parameter for this output. Since the results for both datasets and models (Chierici and LET) are qualitatively similar in this study, we only report the sensitivity indices for the LET model and dataset 1, as shown in Figure 24. Nevertheless, the relative permeability endpoints parameters (κ_w^0 and κ_o^0) have small contributions to all outputs.

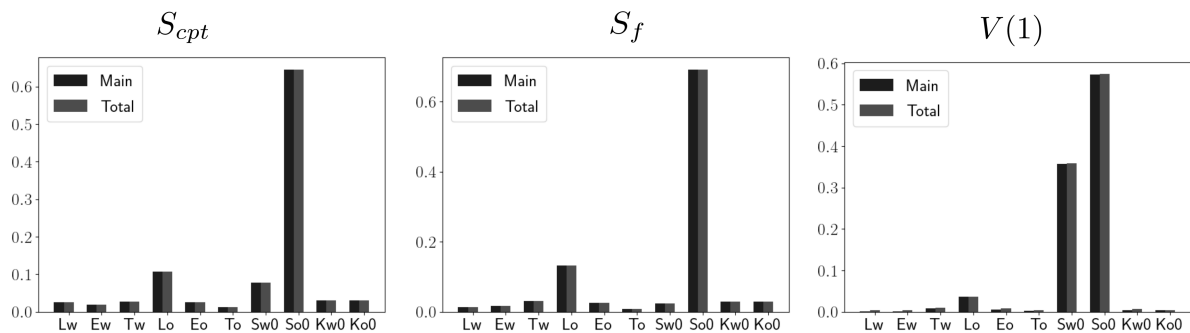


Figure 24 – SA results using the LET for dataset 1 considering the LET model parameters and the relative permeability endpoints (κ_w^0 , κ_o^0 , S_{w0} , and S_{o0}) for the analysis.

4.4 Discussion

The datasets present different petrophysical and phenomenological properties of core flooding experiments [90, 56]: dataset 1 had a wettability regime with a preference to displace more oil than water, while dataset 2 had the opposite behavior. The relative permeability crossing point S_{cpt} is the QoI that most closely characterizes this property. Figure 25 shows the density distribution estimated for S_{cpt} for the different models and datasets. Note that, for a given dataset (water-wet or oil-wet), the uncertainty propagation did not produce samples with S_{cpt} values that crossed the threshold of 0.5.

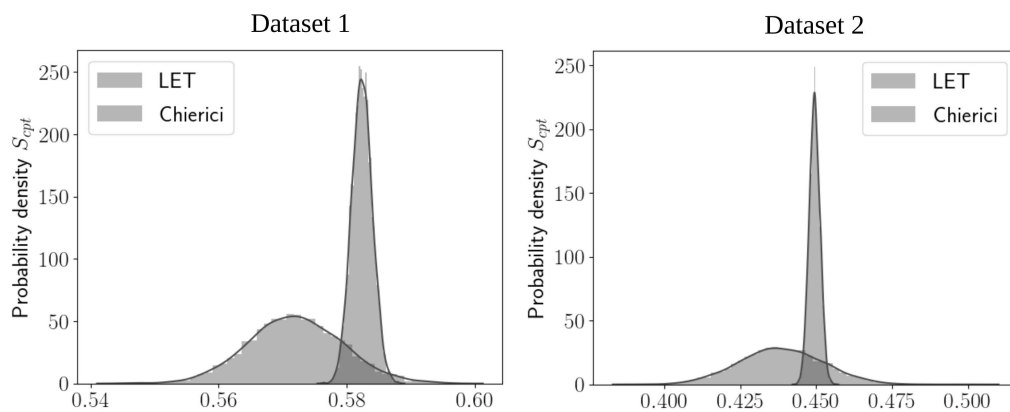


Figure 25 – Density distribution estimated for S_{cpt} using the different models for both datasets.

For the Chierici’s model, the posterior distributions obtained for the parameters by the MCMC method (Table 3) had similar shapes (normal distributions) with small variances. In contrast, for the LET model, the posterior distributions of the parameters had different shapes (normal and log-normal) with larger variances. In addition, a strong correlation between the parameters of the LET model was observed.

The inverse uncertainty propagation analysis performed in this work revealed that assuming 5% of measurement errors had different effects on the input parameter distributions as detailed in Table 3. Nevertheless, both relative permeability models propagated these uncertainties to all the outputs with a variability bounded by 3%, as shown in Table 4. However, with respect to the produced oil and water-cut, the choice of the relative permeability model (Chierici’s or LET) affected the predictions given by the simulator for dataset 1. The oil-production curve (shown in Figure 21), reported significantly different expected values between Chierici and LET models (Table 4). The average value for oil-production at $t = 1$ was about 4% higher with the LET model compared to Chierici’s model.

The SA study revealed different behaviors depending on the rock wettability and on the particular QoI. For instance, for dataset 1 and Chierici’s model the parameters with highest Sobol sensitivity index for S_{cpt} , S_f , and $V(1)$ were A and L (see Figure 22). For dataset 2, the B parameter from water relative permeability functions appears as a relevant parameter to both S_{cpt} and S_f . Another interesting result revealed interactions between all the two permeability model parameters’ for the output $V(1)$ for both datasets.

Both relative permeability models (Chierici and LET) had their corresponding parameters adjusted to reproduce two different datasets containing measurement errors, which were considered equal to 5% of the reported values. This resulted in a non-uniform distribution of error for each dataset, as shown in Figure 18, where the higher endpoints measurement contains more error than other regions of the permeability curves. This approach represents a modeling limitation of this study.

Other limitations of this study are worth remarking. In this work, we focused only on the propagation of uncertainty from the relative permeability input parameters to the model outputs considering two different relative permeability models and datasets. The present study allowed to evaluate how the uncertainty from experimental data and calibration of the model’s parameters can influence the predictions of the model. Therefore, other physical inputs like porosity, absolute permeability, cross-section area, and flow rate were not included in the analysis. Future studies can evaluate the propagation of uncertainties from these parameters to the model predictions.

The framework used for the estimation of parameters’ posterior distribution based on MCMC method started from an initial estimate of the parameters obtained from a least-squares problem. Then, the MCMC starts a sequence of chains from the neighborhood

of the initial estimate and move around randomly exploring the parameter space. In the end, the samples from the chains are used to determine the type of probability distribution (*e.g.* normal) and its parameters (for example, see Figure 20). In this work, the relative permeability models, datasets, and procedure used for the estimation of posterior distributions never obtained values for any parameters, which resulted in unphysical relative permeabilities. Consequently, the simulations of the Buckley-Leverett model employing the posterior distributions obtained with the MCMC method never resulted in any model failure.

4.5 Conclusions

In this work, uncertainty quantification and sensitivity analyses of two relative permeability models were performed in the context of two phase flow in a porous medium. Relative permeability data for water and oil from the literature were used to adjust the models using the MCMC method. Posterior distributions of parameters were determined by the MCMC method, which were used as uncertain input parameters for the two-phase flow in porous medium. We have considered two different datasets with different petrophysical properties.

The simulations results showed strong correlations between LET parameters for both analyzed datasets, whereas less significant correlations were observed for Chierici's model. Sensitivity analysis highlighted that the parameter with the highest sensitivity index varied, depending on the QoI and on the wettability of the dataset. Besides, the SA revealed high interactions between all the two permeability model parameters' for the output associated with oil-production.

This work presents modern methods for data analysis and model evaluation such as the MCMC method, global UQ and SA methods with an application to a model of two-phase flow in a porous medium at core-scale. The observations in terms of uncertainty and sensitivity of the parameters will be useful for further studies regarding the calibration of the models as well as for guiding new experiments. The method presented in this work requires no changes to the computer model and is computationally efficient, in the sense that fewer model evaluations are required to achieve convergence when compared to the classic Monte-Carlo method. Thus, the proposed method for performing UQ and SA analyses seems an attractive alternative for field-scale problems, where the computational cost of one model evaluation is typically very high.

5 Foam assisted water–gas flow parameters: from core–flood experiment to UQ and SA

This chapter was first published in *Transport in Porous Media*, 2021 by Springer Nature. The content of this chapter is a reprint of the work of Valdez *et al.* [137], DOI: 0.1007/s11242-021-01550-0. Reproduced with permission from Springer Nature.

Uncertainty quantification and sensitivity analysis are crucial tools in the development and evaluation of mathematical models. In enhanced oil recovery, the co-injection of foam in porous media has been investigated through laboratory experiments and mathematical models as a promising technique for improving sweep efficiency. In this work, we study two mathematical models of foam flow in porous media. First, we present a foam-quality scan experiment using nitrogen and low concentration of an alpha-olefin sulfonate surfactant in brine using Indiana limestone carbonate core. Second, we evaluate the models based on their ability to represent the experimental data using inverse uncertainty quantification techniques. Third, the parameters' estimated distributions are used to perform both forward uncertainty quantification and sensitivity analysis. We also present a detailed comparison of the models, and analyses on the experimental data, model discrepancy, and sources of uncertainties. The experimental results of foam apparent viscosity in carbonate rocks are consistent with other experiments in sandstones: the foam quality transition is present; the difference in apparent viscosity values is of the same magnitude as the difference in permeability. Propagation of uncertainties from the estimated parameter distributions through the models showed a good match between experimental data and model predictions. The sensitivity analysis showed that the model's parameters play different roles and depend on the quantity of interest, the foam-quality regime, and limiting water saturation. To summarize, this study provides essential information for possible improvements in the experiments and mathematical models of foam flow in EOR processes

5.1 Introduction

Water-alternating gas (WAG) injection technique is commonly used to increase the sweep efficiency in enhanced oil recovery (EOR). However, WAG is subjected to different factors that may reduce the efficiency of gas flooding for EOR. In this context, sweep efficiency may be hampered by effects like the formation of viscous fingers [62], gravity override, and reservoir heterogeneities [133]. The injection of foam in the water and gas displacement, if properly designed, can address these issues and help to restore the sweep efficiency. The foam assisted process during EOR can significantly reduce gas mobility and increase the apparent viscosity of the gas phase, which improves recovery efficiency.

Experimental studies on foam flow applications for EOR have been explored quite

successfully in the literature [62]. Foam quality-scan and flow-rate-scan experiments are usually employed to assess foam properties for calibrating the parameters of computational models [148]. In the flow quality-scan experiment, the total flow rate is constant, while the pressure drop in the core sample is measured as a function of foam quality. In the flow-rate-scan, the foam quality is fixed, while the flow rate is varied.

Physical modeling of the foam flow in porous media is challenging due to its non-Newtonian nature, its dependence on the foam texture, and the complex bubble generation/destruction process. Several models can be found in the literature [5, 74, 83, 150]. In particular, equilibrium models consider foam texture given by an empiric relation. In the present work, we analyze two simplified versions of equilibrium models: (1) default model used in STARS commercial simulator [31] and (2) linear kinetic model [5].

Model calibration is not straightforward, and specialized methods have been proposed before [12, 95, 98, 148]. The method proposed by Boeijs & Rossen [12] uses a manual procedure to fit foam flow models to the apparent foam viscosity data. The procedure works separately with data in the low- and high-quality regimes and uses the apparent viscosity and foam quality plot. The method presents some limitations for fitting experimental data with a gradual transition from the low- to high-quality regimes. [98] and [97] proposed a combined approach based on a graphical method and least-squares minimization, which uses constraints and weighting factors in the cost function to improve the fitting procedure. [45] and [95] have also used data weighting and constraints when employing non-linear least-squares minimization methods. A different approach was proposed by [148], which converted the problem of fitting many parameters to a procedure based on linear regression and single-variable optimization. Their improved algorithm avoids problems concerning non-uniqueness solutions and sensitivity issues of the initial estimates.

The methods used so far to estimate foam flow model parameters neglect the inherent uncertainty, due to technical limitations or measurement errors, present in experimental data. In addition, model discrepancy, i.e., the mismatch between model and experiment, and the correlation between the parameters are also overlooked. The uncertainties in the experimental data and the model discrepancy should be considered to assess the mathematical model's reliability. One way to investigate the above questions is via Bayesian parameter estimation methods, such as the Markov Chain Monte Carlo (MCMC) method, which is used to characterize a model's parameters in terms of their posterior distributions, given a set of experimental data and a model [18]. For linear models and parameter uncertainties described by Gaussian distributions, simple methods can backpropagate the experimental errors to the model's parameters, such as linear and non-linear least-squares methods. However, since the phenomenon of foam flow in porous media is highly complex and non-linear, the MCMC method is better suited for the task of uncertainty quantification. The MCMC method provides global information on parameter

uncertainties, such as posterior probability distribution functions of general shapes, and better estimations than least-squares methods.

A recent study described a workflow for inverse and forward uncertainty quantification (UQ) and sensitivity analysis (SA) to evaluate different models for relative permeability [138]. The framework used the MCMC method to estimate the probability distributions of parameters. For forward UQ and SA, the Polynomial Chaos Expansion (PCE) method [30] was applied to reduce the costs associated with the solution of partial differential equations. In the present work, we focus on a particular EOR technique [29] where foam injection in porous media is used to improve sweep efficiency. Algebraic foam flow models under local-equilibrium conditions are studied by performing forward UQ and SA through the more straightforward, although robust, Monte Carlo (MC) method.

In this work, we present new high-pressure (10 MPa) foam quality-scan experimental data using a mid-range permeability Indiana limestone rock ($2.70 \times 10^{-13} \text{ m}^2$). Foam-scan experimental data in carbonate rocks and at this permeability range are scarcely found in the literature and may provide further insight into how foam parameter may change with the type of rock.

These experiments are further analyzed via the use of two different mathematical models, model's parameter fitting, uncertainty quantification, and sensitivity analysis. The two models used in this work were the commercial [31] model and the Linear Kinetic (LK) model, described in [5].

The remainder of this article is organized as follows: Section 5.2 describes experimental settings, experimental data, mathematical models, and numerical methods used to study the effects of foam displacement in water and gas drainage processes. Section 5.3 introduces the framework used to execute uncertainty quantification and sensitivity analysis on experimental data and computational models. In Section 5.4, the results of inverse uncertainty quantification characterization of experimental data followed by forward UQ and SA analyses are presented. Discussions and limitations of this study are presented in Section 5.5, while in Section 5.6 we present the main contributions of this work.

5.2 Foam displacement in porous media

5.2.1 Fluids and Rocks

The brine used in this work was prepared by dissolving appropriate amounts of salt in distilled water at concentrations presented in Table 5. Prior preparation of surfactant solution, brine was degassed using a vacuum pump. All the salts used to prepare this brine were purchased from Sigma-Aldrich Brazil and were reagent grade.

A sodium alfa-olefin sulphonate (Bioterge AS-40) was the chosen surfactant for

Table 5 – Ionic composition of injection water (IW) used in this study.

Ions	Na ⁺	K ⁺	Ca ²⁺	Mg ²⁺	SO ₄ ²⁻	Cl ⁻
Concentration (mg/L)	11008	393	132	152	41	17972

foam injection, and used in this work at concentration of 0.1 wt%. It was kindly donated by Stepan Brazil, and its critical micelle concentration (CMC) in IW at 20°C and ambient pressure conditions was 0.0017 wt.%. Nitrogen (99.992% purity, Linde Brazil) was used as gas phase for foam injection in this work.

Indiana limestone (Kocurek Industries, USA) was the rock used for carrying out the foam experiments, whose dimensions and petrophysical properties of the core used in this work are presented in Table 6.

Table 6 – Dimensions and petrophysical properties of Indiana limestone used in this work. L , D , PV , φ , and k are the length, diameter, pore volume, porosity, and permeability of the Indiana Limestone core respectively.

L	D	PV	φ	k
m	m	10^{-6} m ³	-	m ²
0.150	0.0382	26.7	0.155	2.70×10^{-13}

5.2.2 Coreflood experiments

To start the experiment, the core was loaded into the Hassler core holder under confining pressure of 3.44 MPa (500 psi) in vertical position (Figure 26). The core was vacuumed for 2 h and then saturated under vacuum with IW. Confining pressure and pore pressure were then simultaneously raised to 17.2 MPa (2500 psi) and 13.8 MPa (2000 psi), respectively. The core sample was maintained at this pressure for 24 h to guarantee that the core was completely saturated with brine. Afterwards, pore pressure was decreased to 10 MPa (1500 psi) and brine permeability was measured, by injecting IW at different flowrates for several pore volumes. After measuring brine permeability, 0.1 wt% AOS surfactant solution was injected through the bypass and then through the core for at least 5 pore volumes (PV), to displace IW. Next, the system temperature was raised to 60°C. Once pressure and temperature were constant, and the system leak tight, nitrogen and surfactant solution were co-injected at constant superficial velocity (1.45×10^{-5} m/s) and total injection flow rate (0.967 mL/min), but at different gas/liquid ratios.

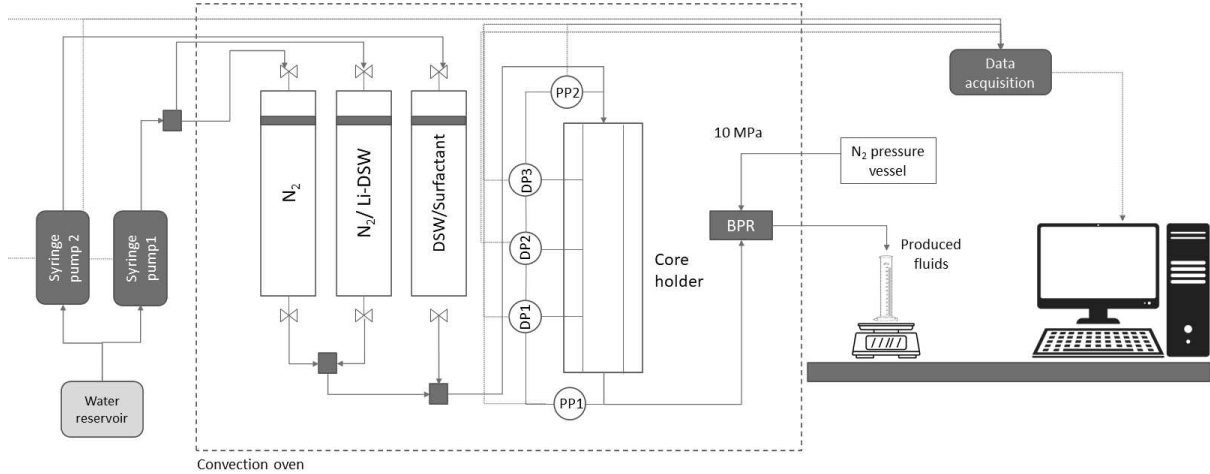


Figure 26 – Schematic drawing of coreflood apparatus used for foam injection.

The foam quality is given by

$$f_g = \frac{q_g}{q_g + q_w}, \quad (5.1)$$

where q_g and q_w are the injection flow rates of gas and liquid, respectively.

Co-injection of fluids took place in a top-to-bottom direction to avoid front instability due to gravity, at an initial foam quality (f_g) of 0.5. At each foam quality, fluids were co-injected until steady states of pressure drop and fluid production were reached. Foam apparent viscosity (μ_{app}) was calculated using the values of pressure gradient ($\Delta P_{foam}/L$), the core absolute permeability (k), the superficial (Darcy) velocity of injection (v), and core length. It is given by

$$\mu_{app} = \frac{k \Delta P_{foam}}{v L}, \quad (5.2)$$

where ΔP_{foam} was calculated as the mean value of the last 500 seconds of measured pressure drop for each foam quality (f_g). Corey relative permeability model was used for the two-phase flow of water and gas without surfactant. Considering k_{rw}^0 and k_{rg}^0 as the end-point relative permeabilities for water and gas, respectively, S_{wc} is the connate water saturation, and S_{gr} the residual gas saturation, the relative permeability models are given by:

$$k_{rw} = k_{rw}^0 \left(\frac{S_w - S_{wc}}{1 - S_{wc} - S_{gr}} \right)^{n_w}, \quad (5.3)$$

$$k_{rg} = k_{rg}^0 \left(\frac{S_g - S_{gr}}{1 - S_{wc} - S_{gr}} \right)^{n_g}, \quad (5.4)$$

where n_w and n_g are the Corey exponents for water and gas, respectively. The relative permeability data for high permeability Indiana Limestone found in the literature [102] was considered. Fitting of the experimental data resulted in the following values: $k_{rw}^0 = 0.302$, $k_{rg}^0 = 0.04$, $n_w = 2.98$, $n_g = 0.96$, $S_{wc} = 0.4$, and $S_{gr} = 0.293$.

5.2.3 Mathematical models

Two different foam flood models were analyzed in this work: a Semi-Empirical (SE) and a Population Balance (PB) model. SE models are mostly found in commercial simulators such as the [31] and UT [24], which include a texture-implicit local-equilibrium foam model that represents the effects of foam directly on the gas relative permeability by considering a mobility reduction factor. PB models employ partial differential equations to characterize the dynamics of foam bubbles in the porous medium. The displacement of water and foamed gas in a porous medium is modeled considering the principle of mass conservation for the two phases (water and gas) and a population balance equation.

For a porous medium Ω the general structure for a PB model is the following:

$$\varphi \frac{\partial S_w}{\partial t} + v \frac{\partial}{\partial x} (f_w) = 0, \quad \text{in } \Omega \times [0, T], \quad (5.5)$$

$$\varphi \frac{\partial S_g n_D}{\partial t} + \frac{\partial}{\partial x} (u_g n_D) = \varphi S_g (r_g - r_c), \quad \text{in } \Omega \times [0, T], \quad (5.6)$$

where φ represents the porosity of the core sample. The variable n_D is the normalized foam texture (related to the number of bubbles per volume). Considering that the medium is fully saturated, the solution to this problem is characterized by the pair (S_w, n_D) .

Under the assumption of local-equilibrium (LE), i.e., when the foam is no longer created or destroyed, it can be shown that the PB and SE models foam flow responses agree with each other. [51, 52] compared STARS and the [76], while [48] studied the PB model proposed by [23]. In this work, we consider the [31] mathematical model and the Linear Kinetic model [5]. In these models, the authors tailored the concept of mobility reduction factor (*MRF*) as function that alters the mobility of the gas phase. In general, the apparent viscosity can be written as the inverse of the total relative mobility as follows:

$$\mu_{app} = \left(\lambda_w + \frac{\lambda_g}{MRF} \right)^{-1}, \quad (5.7)$$

in this settings the gas fractional flow is re-defined as the next ratio including the *MRF* function:

$$f_g = \frac{\lambda_g}{MRF \left(\lambda_w + \frac{\lambda_g}{MRF} \right)} = \frac{\lambda_g}{MRF} \mu_{app}. \quad (5.8)$$

5.2.4 STARS model

In the [31] commercial simulator, the effects of foam are modeled by considering a reduction factor that affects gas mobility. In the foam modelling used in STARS, the mobility reduction factor (*MRF*) describes the effects of the surfactant concentration, of the water and oil saturations, of the shear-thinning, and also of the capillary-number. In order to allow a fair comparison between STARS model and the one proposed by [5], this

work only considers MRF dependencies on water saturation. In particular we neglect capillary effects, non-Newtonian flow behavior. The simplified STARS foam model gas mobility (λ_g) is given by:

$$\lambda_g = \frac{k_{rg}}{MRF \mu_g}, \quad MRF = 1 + fmmob F_2, \quad (5.9)$$

where F_2 accounts for water saturation effects:

$$F_2 = \frac{1}{2} + \frac{1}{\pi} \arctan(sfbet(S_w - SF)), \quad (5.10)$$

5.2.5 Linear kinetic model

The linear kinetic model proposed by [5] follows the structure of Equations (5.5) and (5.6), but it also shares similarities with the mobility reduction factor employed in the STARS model. The mobility reduction factor from [5] is given by:

$$\lambda_g = \frac{k_{rg}(S_w)}{\mu_g MRF}, \quad MRF = 1 + C_{mrf} n_D. \quad (5.11)$$

In the original work [5] the value for C_{mrf} was fixed at 18500, whereas here we allow it to change. In this model the source term from Equation (5.6) is given by:

$$\varphi S_g (r_g - r_c) = \varphi k_c S_g (n_D^{LE} - n_D), \quad (5.12)$$

where the LE state it is assumed to be:

$$n_D^{LE} = \begin{cases} \tanh(A(S_w - S_w^*)), & S_w > S_w^*, \\ 0, & S_w \leq S_w^*, \end{cases} \quad (5.13)$$

where k_c , C_{mrf} , A and S_w^* are parameters of the model. In particular, we will assume that $n_D = n_D^{LE}$, i.e., n_D is always at local equilibrium. For this case, the parameters C_{mrf} , A and S_w^* can be estimated in a similar fashion as the parameters from the STARS model.

5.3 Methods for uncertainty quantification and sensitivity analysis

In this section, we describe the methods used for analyzing the foam flow models and experimental data. First, we describe the quantities of interest that shall be evaluated by the models, then we introduce the methods for inverse and forward UQ as well as for performing sensitivity analysis. The techniques used in this work for the foam flow has also been discussed extensively for other contexts in the literature [39, 100, 117].

5.3.1 Quantities of Interest

Both foam models described in Section 5.2 are conceived to reproduce, in a computational environment, the effects of foam in applications like water and gas drainage.

In such models the main effect of foam is materialized with a mobility reduction function with similar expressions (see Equations (5.9) and (5.11)). In addition to this, both foam models attempt to replicate how apparent viscosity depends on foam quality.

To compare both foam models, the following quantities of interest (QoIs) were studied: (i) apparent viscosity (μ_{app}), (ii) mobility reduction factor (MRF), (iii) total relative mobility, and (iv) pressure drop for each foam scan data calculated at equilibrium.

The *apparent viscosity*: described in Equation (5.2) is an important quantity that links the pressure gradient measured in the core sample and the total inflow rate imposed in the core sample.

The *mobility reduction factor*: models how the presence of foam reduces gas mobility. For the analyzed foam models, this quantity was presented in Equations (5.9) and (5.11).

The *total relative mobility* is a quantity defined by:

$$\lambda_{rt} = \frac{k_{rw}}{\mu_w} + \frac{k_{rg}}{MRF\mu_g}. \quad (5.14)$$

This function has two regimes: the regime where there is no foam and λ_{rt} achieves its maximum value and the regime where foam reduces its value. In general, the transition between the two regimes is abrupt. As discussed in [44], the total relative mobility is an important indicator of fingering, which might occur when the total relative mobility upstream is larger than that downstream. The *pressure drop* (ΔP_{foam}) can be simply written as a function of the apparent viscosity (5.2) as:

$$\Delta P_{foam} = \frac{\mu_{app} v L}{k}, \quad (5.15)$$

where L is the distance between two different points for instance injection-production wells.

5.3.2 Parameter estimation and propagation of uncertainties

Our overall approach for estimating and propagating uncertainties in the model is described in detail in a previous paper [138]. To estimate the uncertainty in the parameters (inverse UQ), we used a Bayesian framework for the foam flow models based on the Markov Chain Monte Carlo (MCMC) method available in the PyMC3 package [121]. The MCMC requires the specification of prior distributions for the model parameters, which were chosen considering physical ranges of the parameters and available knowledge from the literature [45]. The inferences were performed using 400,000 samples and the slice sampler algorithm. To evaluate if the MCMC has converged, we performed multiple simulations with Markov chains from different initial parameter sets and compared the resulting posterior distributions. Owing to the large number of samples used for the experiments, other choices of prior distributions, keeping the same physical and known

ranges for the parameters, did not significantly affect the obtained posterior distributions. We acknowledged convergence after checking if the same distribution was obtained for different realizations of the MCMC method.

Once the posterior distributions are determined for all the model's input parameters using the experimental data, the propagation of such uncertainties to the foam flow model can be carried out (forward UQ). We used the classical MC method to perform this task, which samples the distributions obtained for the parameters via the MCMC method.

To analyze the propagation of uncertainty, for each QoI, we measured the expected value, variance, and confidence intervals [39]. The 90% prediction interval were also calculated by evaluating the percentiles of the distributions of the output QoIs. The 90% prediction interval (90%*PI*) highlights the results that are within the 5th and 95th percentiles.

5.3.3 Sensitivity analysis

To assess how the input parameters $x_i \in \mathbf{x}$ and their interactions contribute to the variations of any quantity of interest \mathcal{Y} , a variance-based sensitivity analysis was performed. This allows us to identify the input parameters that do not affect the variability of a chosen QoI, from the input parameters that significantly contribute to the uncertainty of the QoI. To this end, we used the main and total Sobol indices [120, 127]. The first order Sobol index (or main Sobol index), expresses how any an uncertain input x_i directly contributes to the variance of the output \mathcal{Y} . It is given by the following expression:

$$S_i = \frac{\mathbb{V}[\mathbb{E}[\mathcal{Y}|x_i]]}{\mathbb{V}[\mathcal{Y}]}.$$
 (5.16)

The first order Sobol index neglects eventual interactions between two or more different uncertain inputs. To estimate the changes on $\mathbb{V}[\mathcal{Y}]$ considering first and high-order interactions of the i -th uncertain input, the total Sobol index [120] is evaluated. It is given by:

$$S_{Ti} = 1 - \frac{\mathbb{V}[\mathbb{E}[\mathcal{Y}|x_{-i}]]}{\mathbb{V}[\mathcal{Y}]},$$
 (5.17)

where x_{-i} denotes the set of all input parameters except x_i . Sobol indices were computed with the `SALib` package using the Saltelli sampler algorithm [63].

5.4 Results

5.4.1 Quality-scan experiment

Figure 27 show the results of the foam quality-scan experiment (left) and the relative permeabilities used in this work, which was fitted from data reported in the literature [102] (right). The quality-scan results show that the foam apparent viscosity

first increases with increasing foam quality up to a maximum value (around $f_g = 0.75$), and then decreases.

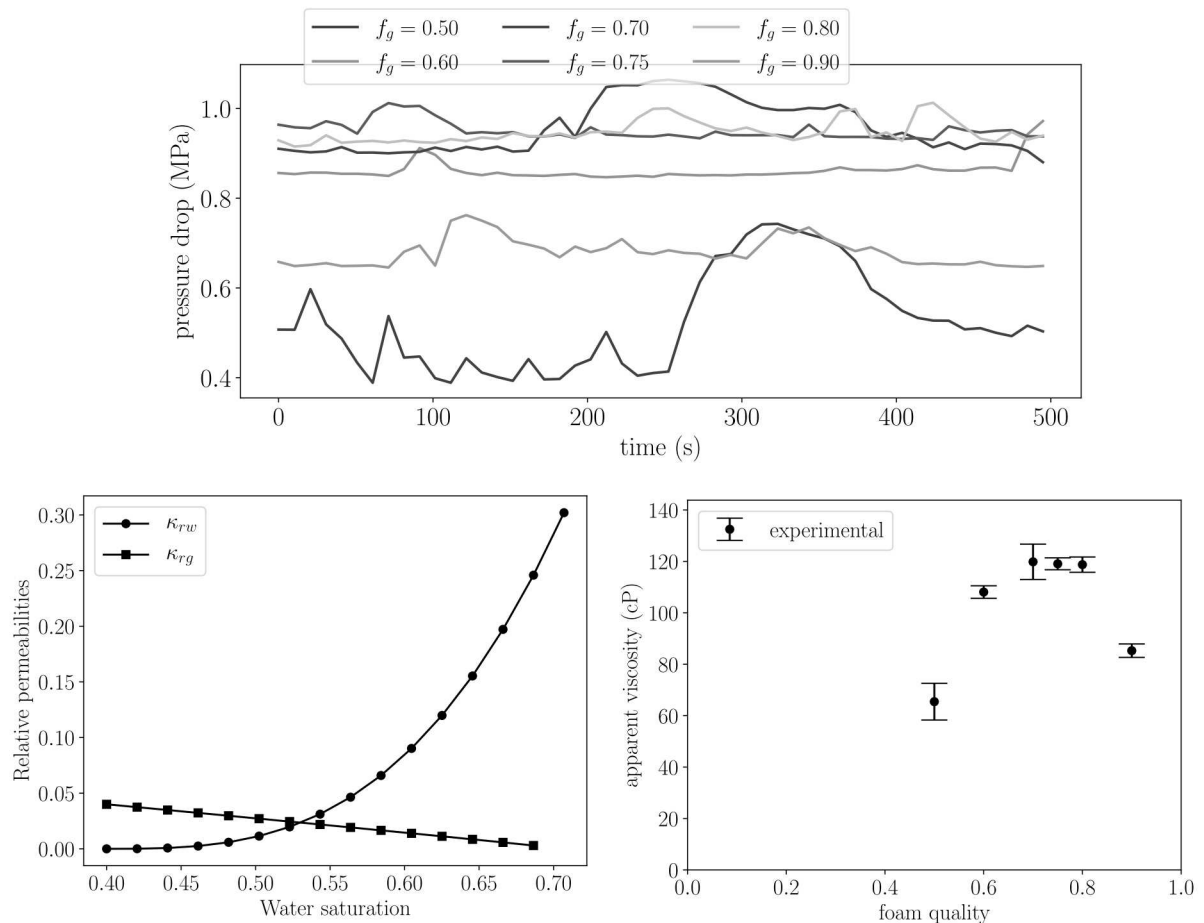


Figure 27 – Foam quality-scan experiment results: (top) pressure drop at steady state, (left) adjusted relative permeability curves adapted from [102]; and (right) apparent viscosity values as function of foam quality.

5.4.2 Characterization of foam model parameters

To characterize the posterior distribution of the foam model parameters in the STARS and LK models, the MCMC method was executed using uniform priors for all parameters \mathbf{x} . Table 7 shows the properties of the priors used. Uniform priors were chosen due to the limited knowledge about the variables of interest where only physical or practical ranges obtained in the literature are known. In particular, SF and S_w^* were bounded by physical limits considering the connate water S_{wc} and residual gas S_{gr} . For the other parameters, a large range was used for the uniform distributions, as very different values were reported before [44, 78].

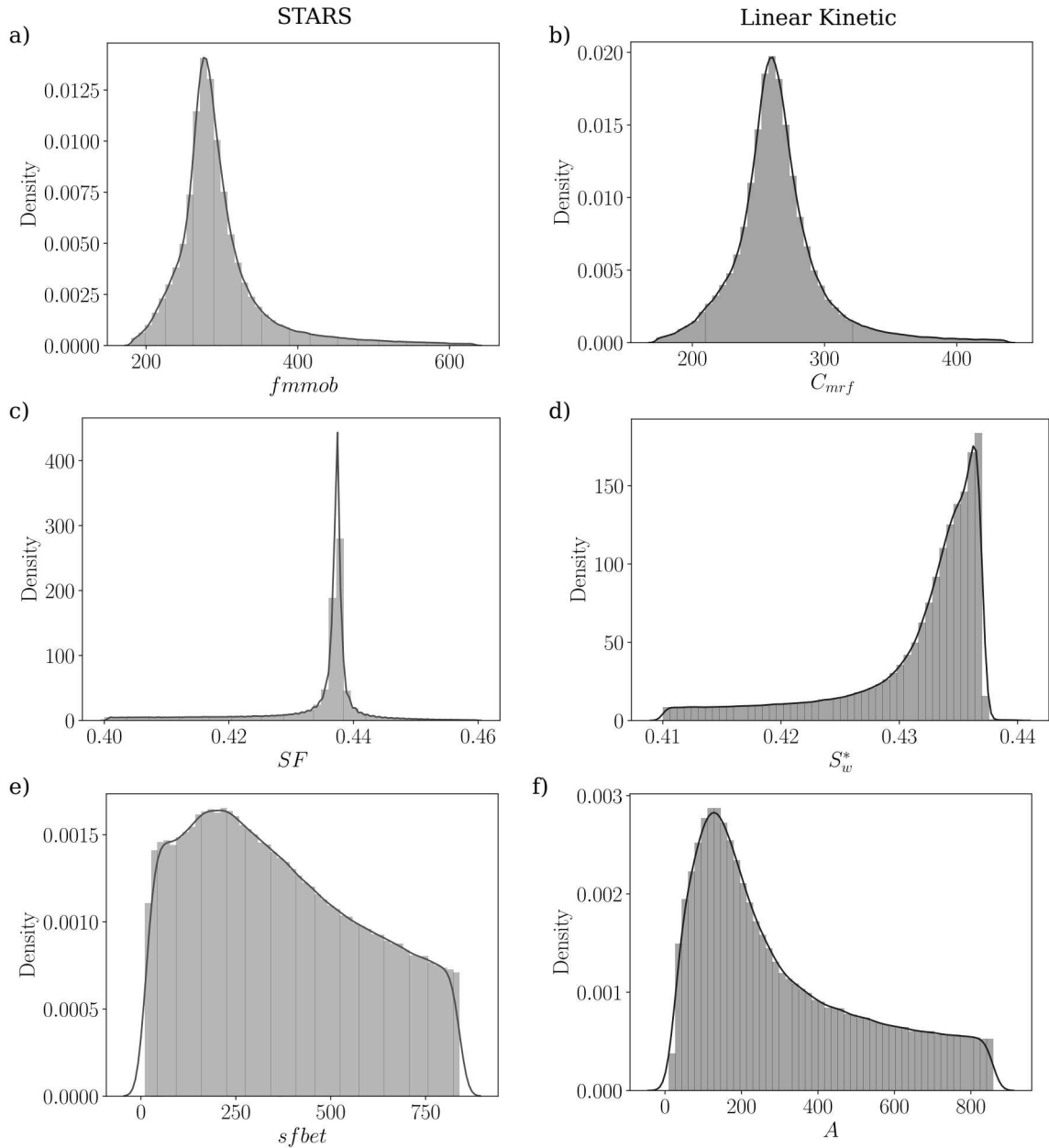


Figure 28 – Kernel density estimates for each parameter posterior distribution of the STARS (left/green) and linear kinetic [5] (right/blue) foam models.

After the execution of the MCMC method, we obtained the posterior distribution for each model parameter. Figure 28 exhibits the densities of both STARS and LK model parameters. The distributions for the STARS parameters' $fmmob$ and SF as well as C_{mrf} and S_w^* for the Linear Kinetic model are more concentrated around the most frequent value. The posterior distribution of A (LK) and $sfbet$ (STARS) are more spread and less symmetric.

To perform a forward uncertainty propagation and sensitivity analysis of the foam models, the posterior distribution of the parameters exhibited in Figure 28 were adjusted to normal or log-normal distributions. Table 7 summarizes the properties of the posterior

distributions obtained by the MCMC method and which were further used by the forward UQ and SA study.

Table 7 – Prior and posterior distributions of the parameters in the foam models: STARS and Linear Kinetic [5].

	STARS		Linear Kinetic	
Priors	$fmmob$	$\mathcal{U}(0, 1000)$	C_{mrf}	$\mathcal{U}(0, 1000)$
	SF	$\mathcal{U}(0.40, 0.707)$	S_w^*	$\mathcal{U}(0.40, 0.707)$
	$sfbet$	$\mathcal{U}(10, 1000)$	A	$\mathcal{U}(10, 1000)$
Posteriors	$fmmob$	$\mathcal{N}(295.988, 61.268)$	C_{mrf}	$\mathcal{N}(264.788, 34.452)$
	SF	$\mathcal{N}(0.434, 0.009)$	S_w^*	$\mathcal{N}(0.431, 0.006)$
	$\log(sfbet)$	$\mathcal{N}(6.526, 0.321)$	$\log(A)$	$\mathcal{N}(5.563, 0.726)$

5.4.3 Uncertainty propagation

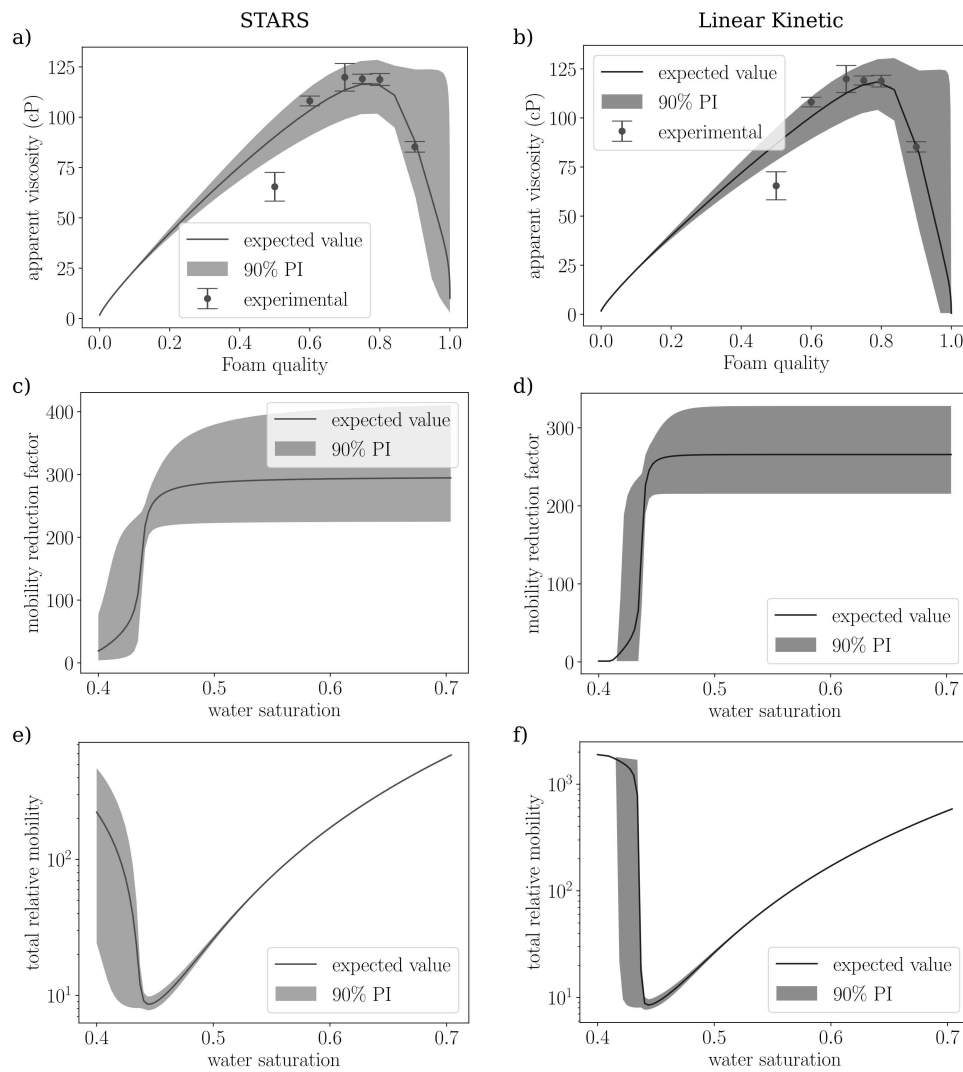


Figure 29 – Uncertainty quantification results of (a-b) apparent viscosity; (c-d) mobility reduction factor (MRF); and (e-f) total relative mobility (λ_{rt}) for the STARS (left column) and linear kinetic [5] (right column) foam models. The shaded regions correspond to the 90% prediction interval (90% PI) and the solid lines represent the expected values.

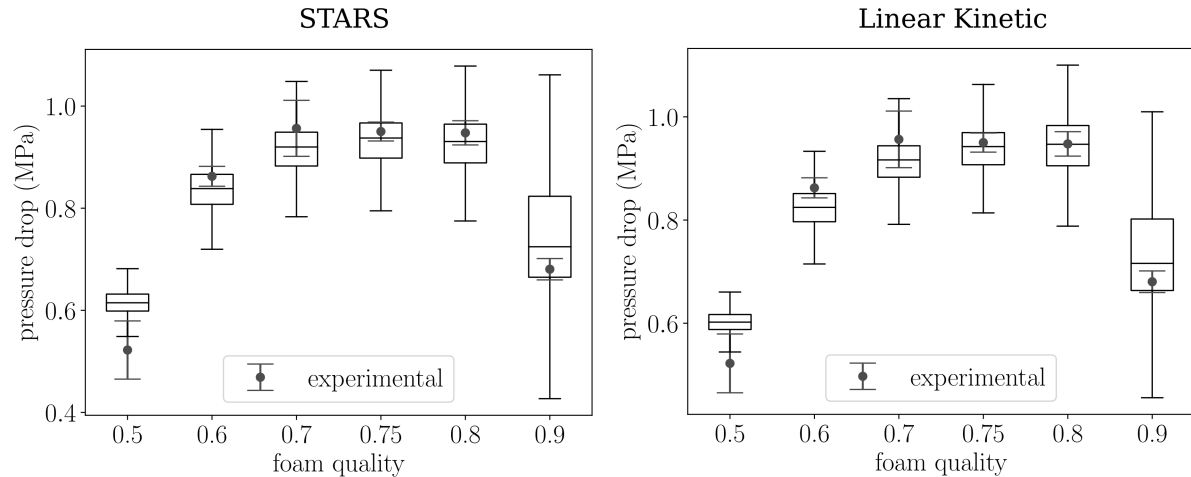


Figure 30 – Uncertainty propagation in the pressure drop using STARS (left) and Linear Kinetic (right) models. Box plots of the data evaluated by the MC execution and experimental data (red squares).

Figure 29 shows the propagation of uncertainty for apparent viscosity, mobility reduction factor, and total relative mobility computed by both foam models. First, for the apparent viscosity, the expected value curves are very close to the experimental data, except for $f_g = 0.5$. Also, the prediction interval (90% PI) observed in the low-quality regime is smaller than in the high-quality regime, where more uncertainty can be noticed in both models. More uncertainty was observed for low water saturation values for total relative mobility, around the limiting water saturation S_w^* , than for high values of water saturation. In addition, we observed higher uncertainties in the STARS model than in the Linear Kinetic model when comparing the results for mobility reduction factor and total relative mobility.

Figure 30 presents the results of the uncertainty propagation of pressure drop. At each level of foam quality (f_g) we present the results using box plots by evaluating the corresponding foam model using the posterior MCMC parameters' samples. Both STARS and Linear Kinetic models capture the experimental pressure drop within the uncertainty range, except at $f_g = 0.5$. For the high-quality regime at $f_g = 0.9$, the uncertainty range is large, undermining the model's predictions. One possible reason for this large range of uncertainty is the lack of measured data in this region. In particular, for the high-quality foam (on the descendent part of the apparent viscosity function in Fig. 29 (a)-(b)), there is only one measurement at $f_g = 0.9$. Section 5.2 investigates this issue with a more in-depth UQ analysis using an augmented dataset.

5.4.4 Sensitivity analysis

We present the sensitivity analysis results using main and total Sobol indices for all QoIs in Figure 31. For the apparent viscosity in the low-quality regime, we observe that $fmmob$ (C_{mrf}) of STARS (Linear Kinetic) almost dominates the quantity. However, in the high-quality regime, the parameter SF (S_w^*) of STARS (Linear Kinetic) becomes the most relevant one. Near the foam quality transition, the parameters $sfbet$ (STARS) and A (Linear Kinetic) also influence the apparent viscosity.

Similar behavior was observed for the mobility reduction factor (MRF) and total relative mobility (λ_{rt}). The roles of the parameters change near $S_w = 0.43$, which corresponds to the expected value found for SF (STARS) and S_w^* (Linear Kinetic) shown in Table 7. For values below 0.43, the sensitivity to SF and S_w^* is high, whereas for values above this limit, $fmmob$ (STARS) and C_{mrf} (Linear Kinetic) dominate.

In addition, we remark that high-order interactions among the parameters were only observed in the two regimes' transition, as indicated by the total Sobol indices when using the Linear Kinetic model. In the case of STARS, high-order interactions are present for low-quality regimes or S_w below the critical value.

Next, the sensitivities of the model parameters with respect to pressure drop were evaluated. Figure 32 presents the main and total Sobol indices for STARS and Linear Kinetic models for each level of foam quality used in the experiment. For both models, the sensitivity to $fmmob$ (STARS) and C_{mrf} (LK) is high in the low-quality regime. For the STARS model, the pressure drop remained sensitive to $sfbet$ uniformly for all foam qualities. In contrast, the pressure drop evaluated with the LK model showed more sensitivity to the parameter A for foam qualities near the transition region. The parameters SF (STARS) and S_w^* (LK) had relevant influences only at $f_g = 0.9$.

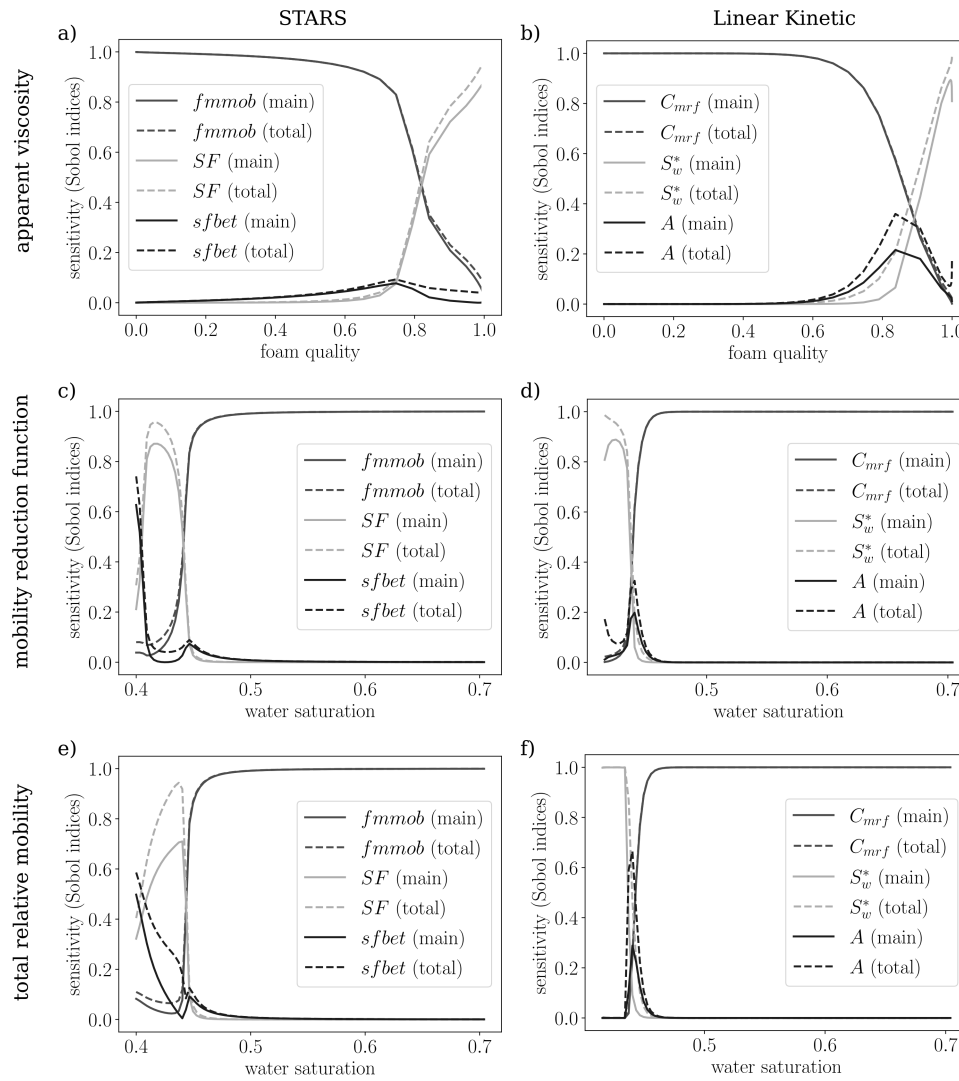


Figure 31 – Sensitivity analysis using Sobol indices results of (a-b) apparent viscosity; (c-d) mobility reduction factor (MRF); and (e-f) total relative mobility (λ_{rt}) for the STARS (left column) and LK [5] (right column) foam models.

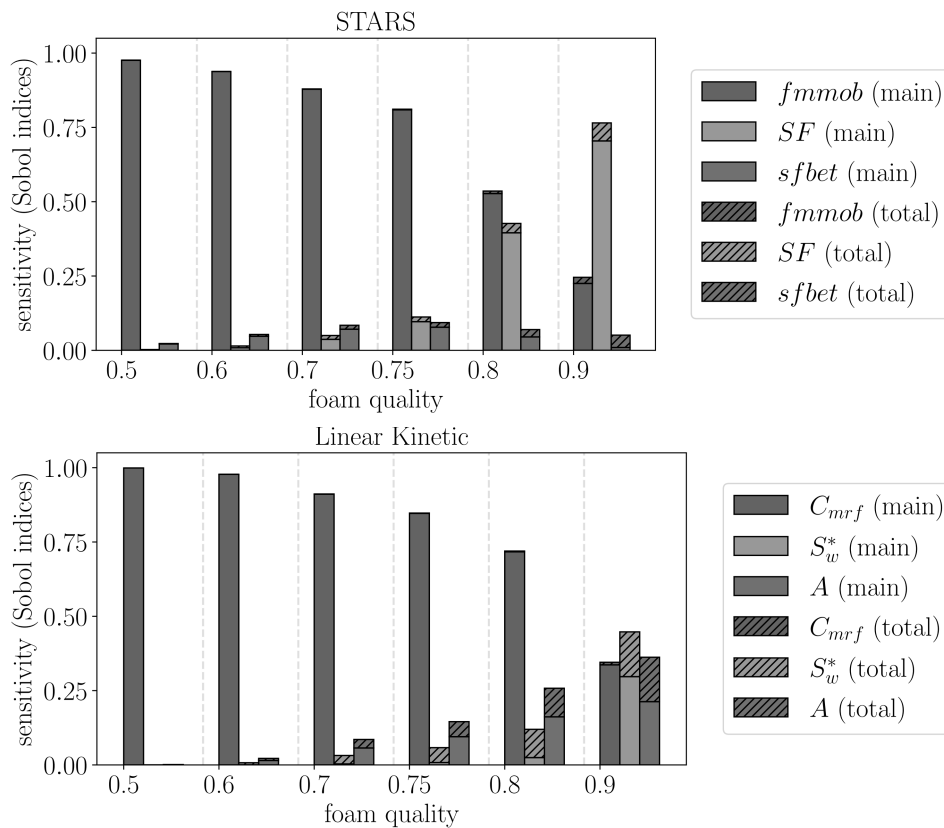


Figure 32 – Sensitivity analysis of the pressure drop for different foam quality levels. Main Sobol and total Sobol indices are shown for STARS and linear kinetic (LK).

The sensitivity analysis revealed that the model’s parameters play different roles and depend on the quantity of interest, the foam-quality regime, and limiting water saturation. It was shown that $fmmob$ for STARS and its equivalent parameter in the Linear Kinetic model are highly relevant in the low-quality regime. In contrast, in the high-quality regime the SF parameter from the STARS model (and the corresponding parameter in LK model) is the most relevant for apparent viscosity. For quantities related to mobility (such as MRF and λ_{rt}), the roles of these two parameters change with respect to water saturation: for low values of water saturation, SF is the key parameter, whereas for higher values, the $fmmob$ parameter appears with a higher impact on these quantities.

5.5 Discussions

This work aimed to study the impact of uncertainties in parameters of foam flow models and also to determine the most important parameters using sensitivity analysis. To this end, a foam quality scan experiment was performed, and the posterior distribution of the model parameters was characterized using the MCMC method. Forward UQ and SA were then performed to study the effects of the inputs on apparent viscosity, mobility reduction factor, total relative mobility, and pressure drop.

5.5.1 Experimental data and model discrepancy

Foam-quality scan experiments for mid-range permeability carbonate rocks are scarce in the literature. Most foam-quality experiments performed with nitrogen gas and AOS surfactant is performed with different permeability sandstone rocks [72, 73, 78, 79], and few are dedicated to studying foam formation in carbonate rocks. Results of foam apparent viscosity as a function of foam quality for the Indiana limestone used in this study showed similar profile and foam quality transition to experimental results performed with Bentheimer sandstones at the same surfactant concentration (0.1 wt.%) and superficial velocity (1.45×10^{-5} m/s) [73]. Foam apparent viscosity reported in this work was an order of magnitude smaller than those reported by [73], which is in agreement with the one order of magnitude difference in permeability between Indiana limestone and Bentheimer sandstone used for the experiments.

Although we have simplified both models used in this work, we have observed a good match between the experimental data and the model predictions. The only exception was the data measured at $f_g = 0.5$, i.e., both the STARS and LK models presented a discrepancy to the experimental data (see Figures 29 (a)-(b) and Figure 30).

However, taking a closer look at the raw data of measured pressure drop for $f_g = 0.5$ we have noticed large oscillations that might have undermined the calculation of its steady-state value. Figure 33 shows all the data related to pressure drop (in red) for $f_g = 0.5$, including the transient phase. A visual inspection may suggest that the pressure drop did not reach its steady-state value. Indeed, by fitting the experimental data to a simple exponential model $p(t) = (p_0 - p_{eq})e^{-bt} + p_{eq}$, with $p_0 = 0$, $p_{eq} = 0.6$, and $b = 1.66 \times 10^{-4}$, we observe a good fitting (see the blue curve in Figure 33). In addition, the value of pressure drop at equilibrium $p_{eq} = 0.6$ is within the range of values predicted by both STAR and LK models, as presented in Figure 30. Therefore, the fact that the pressure drop in the experiment did not completely reach steady-state presents itself as a possible explanation for the discrepancy of models and experimental data for $f_g = 0.5$.

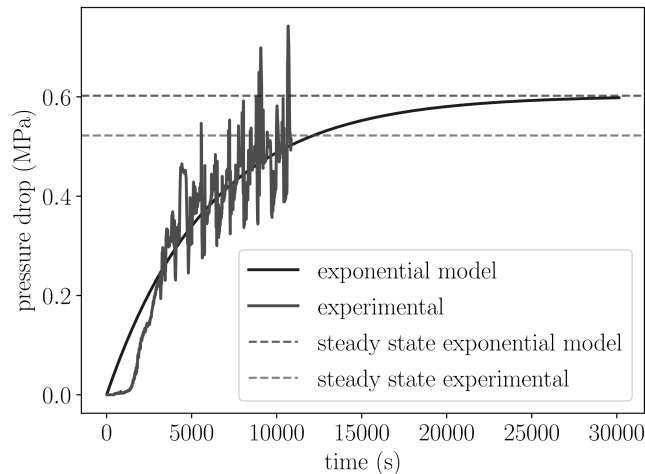


Figure 33 – Experimental records of pressure drop and evaluations of the exponential model.

5.5.2 Source of uncertainties

The propagated uncertainties presented in Figures 29 (a)-(b) and Figure 30 are quite high when compared to those found in the experimental data. Usually, many factors can contribute to these uncertainties: model discrepancy, uncertainties in the experimental data, model structure, parameter identifiability, insufficient data, among others. As discussed in the previous section, we can exclude model discrepancy, as both models were able to reproduce very well the experiments. The fitting process and inverse UQ were also successful, and the parameters were found to be identifiable, mainly due to the simplicity of the mathematical models. Experimental uncertainty was taken into account during the inverse UQ. Nonlinear models can amplify input uncertainties that come from experiments. However, it is worth first investigating if the issue is not due to the lack of experimental data.

To this end, we performed the following exercise. We artificially augmented the amount of available data by including three new synthetic pairs: $(f_g, \mu_{app}) = \{(0.84, 109.3), (0.91, 76.4), (0.99, 13.3)\}$. Using this new data set, we performed the inverse UQ via the MCMC method, followed by the forward UQ using the two mathematical models. Figure 34 shows the obtained results for this new set of data. We can observe that the propagated uncertainty was significantly reduced. Therefore, the main source of uncertainties is likely the insufficient amount of data, in particular, in the high-quality regime, i.e., for high values of f_g .

These results show the importance of the framework presented here, which combines mathematical models, inverse and forward uncertainty quantification, and sensitivity analysis. Based on these tools, we can now suggest new experiments to be performed to further contribute to the understanding of this complex phenomenon.

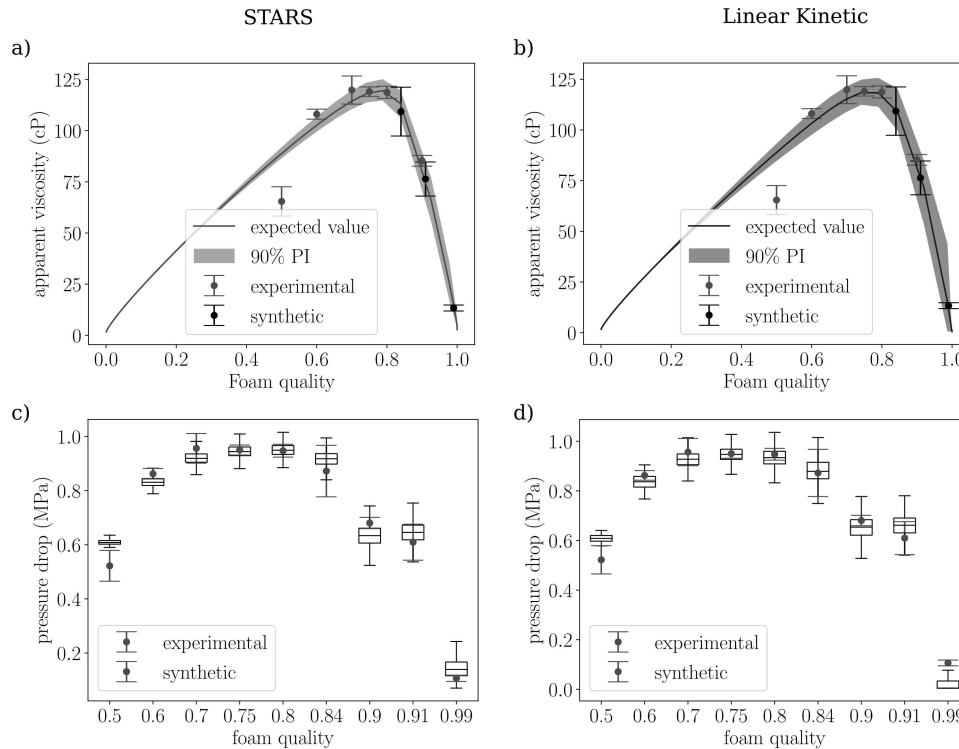


Figure 34 – Uncertainty quantification results of augmented data set: (a-b) apparent viscosity; (c-d) and pressure drop for the STARS (left column) and linear kinetic [5] (right column) foam models. The shaded regions correspond to the 90% prediction interval (90% PI) and the solid lines represent the expected values.

5.5.3 Comparing the two models

STARS and LK models' responses for foam flow in porous media under local equilibrium were similar, as demonstrated by the uncertainty propagation and sensitivity analysis presented before. However, some differences between the two models are worth discussing. The parameters $fmmob$ (STARS) and C_{mrf} (LK) are key parameters for the low-quality regime and control the amplitude of the mobility reduction due to foam.

On the other hand, SF (STARS) and S_w^* (LK) model the critical saturation, i.e., the water saturation at which foam collapses, and are key parameters for the high-quality regime. This is in consonance with the literature [78]. In addition, in [95, 98], it was reported that the water saturation obtained with different models and datasets was not sensitive to the initial guess used in the parameter fitting procedure. Similar behavior was observed here in the estimated posterior distributions, as they share small coefficients of variations (see Table 7 and Figure 28).

The transition between these two regimes is modeled by the parameters $sfbet$ (STARS) and A (LK). As mentioned before, the sensitivities of these parameters with respect to MRF and λ_{rt} , as shown in Figure 31, are different around the connate water saturation S_{wc} . To explain this behavior, Figure 35 shows the mobility reduction factor and

total relative mobility of both models using parameter values fitted to the experimental data. The figure highlights the discontinuous behavior of the Linear Kinetic model as described by equation (5.13). The discontinuity in the LK model translates into high values for the Sobol sensitivity indices around $S_w = 0.4$, whereas low sensitivity values and a smooth behavior for the corresponding parameter in the STARS are observed.

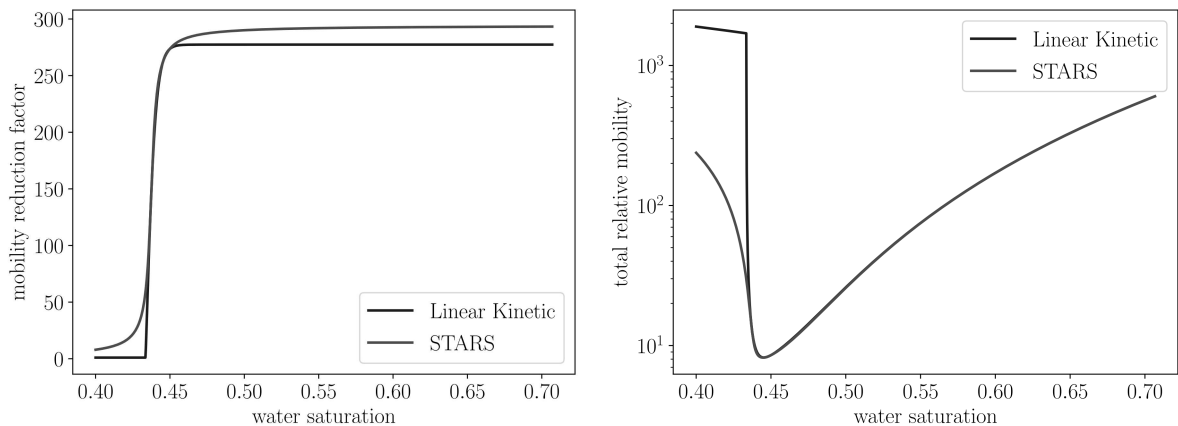


Figure 35 – Mobility reduction factor (MRF) and total relative mobility (λ_{rt}) for STARS $\{fmmob = 293.27, SF = 0.437, sfbet = 359.33\}$ and Linear Kinetic $\{C_{mrf} = 276.40, S_w^* = 0.433, A = 152.32\}$.

5.5.4 Limitations

This work has some limitations worth of discussion. The simplified STARS foam model considered in this work uses MRF depending only on the water saturation, namely the F_2 dry-out function. However, we considered this choice for the STARS functions to allow a fair comparison with the Linear Kinetic model [5], which was assumed in the local-equilibrium. A natural extension would overcome these simplifications by considering the dynamics of foam creation, destruction, and by including more terms in the STARS model to perform a more detailed analysis.

Another limitation is that we only studied uncertainties from the STARS and LK foam models' parameters. Other parameters, such as those from the relative permeability (Corey) model, connate water saturation, residual gas saturations, end-point saturation, porosity, and others, could be included in the UQ and SA study. Other models, such as LET and Chierici, can be used to describe relative permeability data following similar procedures [138]. However, since the present work focuses on uncertainties stemming from foam parameters, these models were not explored.

5.6 Conclusions

This work presented a framework for uncertainty quantification and sensitivity analysis of core-flood experimental data and Bayesian model calibration in foam flow in

porous media. The foam flow core-flood experiment in the Indiana limestone showed a foam-quality scan profile similar to those found in the literature. Foam apparent viscosities were significantly lower than in the literature, in agreement with the larger magnitude of rock permeability. After calibrating the models to the experimental data using an inverse Bayesian estimation, forward UQ analysis for apparent viscosity and pressure drop revealed larger uncertainties for the high-quality foam compared to the low-quality foam. Adding synthetic data for high-quality foam made it possible to reduce the model's uncertainties significantly. As we used experimental data with low apparent viscosity, the same analysis performed on high apparent viscosity setups may provide even greater insights in terms of uncertainty quantification. Therefore, based on the tools presented in this work, we could suggest a new set of experiments that can improve the understanding of the phenomenon.

Experimental data are inherently hampered by errors originating from equipment precision, neglected phenomena, human mistakes, and others. Likewise, models are always wrong, by definition. Yet, scientific knowledge is based on experiments and theory (model). The framework presented in this work acted as a two-way bridge. The tools allowed the evaluation of the model's reliability (via UQ) when confronting the model with experimental data: from experiments to model. The theory rarely improves by merely repeating the same experiments. Nevertheless, the framework (via SA and synthetic experiments) suggested how to increment the experimental data to reduce the model's uncertainties: from models back to experiments.

In summary, based on Bayesian inference, uncertainty propagation, and sensitivity analysis, the presented approach has great potential to improve the understanding of the phenomenon of foam flow in porous media. These tools combined can help confront the theory (models) and experiments to evaluate the model's quality and uncertainties; and suggest new experiments that can improve the model's reliability.

6 Assessing uncertainties and identifiability of foam displacement models employing different objective functions for parameter estimation

Foam injection in porous media is often used to improve the recovery in water alternated gas applications. This work presents a new objective function to calibrate foam models and investigates parameter identifiability and uncertainty quantification (UQ). The new objective function includes data of mobility reduction factor (MRF) and the traditional apparent viscosity data. Identifiability analysis shows that key parameters of the models are practically non-identifiable when using traditional objective functions that rely only on apparent viscosity. This is solved by adding MRF data to the objective function. The UQ analysis revealed a similar trend, with lower uncertainty when using the new objective function than only apparent viscosity. In summary, the new objective function generated the best-calibrated models with the highest fidelity and the lowest uncertainty. The examples presented in this manuscript are taken from the literature to highlight that the new objective function does not require new experimental observations.

6.1 Introduction

The process of alternated water and gas injection into an oil reservoir may be hampered by viscous fingers, gravity segregation, and reservoir heterogeneity (also known as channeling). A promising alternative to overcome these situations is the injection of foam for controlling gas mobility and improve sweep efficiency [43, 15]. Therefore, the injection of foam can improve oil recovery [81]. Understanding the complex phenomenon of foam flow in porous media is crucial for a successful foam-based enhanced-oil recovery (EOR) process design. A remarkable and established technique in this context is the use of numerical simulations based on mathematical models.

Numerical simulators of foam flow in EOR can be split into population balance (PB) and semi-empirical (SE) models. Population balance models [75, 74, 23, 5] take into account the effects of foam by proposing conservation laws for a new variable related to the number of foam bubbles per volume. Semi-empirical models [31, 24] do not take into account the transient dynamics of foam and simulate the effects of foam through algebraic relations and modifications of the gas mobility. Some clear advantages of the SE approach are the lower computational cost, fewer numerical issues, and fewer parameters to estimate when compared to PB models. However, to perform useful simulations to improve the design of foam-based EOR processes, one must adequately estimate the parameters of the SE foam models from experimental data.

The process of parameter estimation for SE foam models has been approached by different studies [12, 95, 98, 97, 148, 138]. Specific methods that take into account features of the foam model, nonlinear least-squares methods, and Bayesian methods have

been considered. The estimation of these parameters is usually performed considering experimental data from a foam quality scan experiment where the total velocity is fixed, and a range of experiments at different foam qualities are performed, resulting in the computation of the so-called apparent viscosity. However, many studies reported on the difficulties associated with the non-uniqueness on the estimated parameters, even for simple foam flow models [12, 98, 96, 97] which only considers the effects of water saturation and neglects, for instance, non-Newtonian behavior or the effects of surfactant concentration. When non-Newtonian effects of foam such as shear-thinning are considered in these models, the issue of non-unique (unidentifiable) parameters is expected to be even harder to handle due to the increase in the number of parameters.

In this work, we focus on the task of parameter estimation for semi-empirical foam models, such as the one considered in the commercial EOR foam simulator [31], including shear-thinning behavior. To this end, we take advantage of a set of powerful and robust techniques. For parameter identifiability analysis, the profile likelihood (PL) technique is used, whereas, for parameter estimation, we relied on the Markov Chain Monte Carlo (MCMC) method complemented by forward uncertainty quantification (UQ) and sensitivity analysis (SA). In particular, we propose to consider additional experimental data in the objective function used for model calibration, combining the traditional apparent viscosity experimental data with information that reflects the mobility reduction factor. The mobility reduction factor requires no additional experiments and can be simply derived from existing two-phase foam flow relations. The identifiability analysis shows that this approach improves the estimation of some important parameters and reduces model uncertainties, as confirmed by the MCMC method and UQ analysis.

The remainder of this text is organized as follows. Section 6.2 introduces the foam models, the employed datasets and presents the different methods for parameter estimation and analysis. In Section 6.3 the results of the analyses are presented, followed by discussions in Section 6.4. The main contributions of the manuscript are summarized in the conclusions Section 6.5.

6.2 Methods

6.2.1 Foam displacement in porous media

Based on experimental observation, the presence of foam preferentially affects the displacement of the gas phase, changing its mobility [40]. The effects of adding foam into the modeling are taken into account by modifying the viscosity of the gas phase. These effects are modeled in the CMG-STARS [31] and other simulators via the concept of mobility reduction factor (MRF). Here we consider foam as a mixture of water and gas with surfactant diluted in the liquid component. The apparent viscosity of the mixture is

obtained from Darcy's law, and is given by

$$\mu_{app} = -\frac{\kappa \nabla p}{u_g + u_w}, \quad (6.1)$$

where κ is the absolute permeability of the porous medium, ∇p is the pressure gradient, and u_w and u_g are water and gas velocities, respectively. In particular, the total flowing velocity is $u = u_w + u_g$, such that Darcy's law can be used again yielding $u = -\kappa \lambda_T \nabla p$; where λ_T is the total relative mobility of the mixture given by:

$$\lambda_T = \frac{\kappa_{rw}}{\mu_w} + \frac{\kappa_{rg}}{MRF \mu_g} = \lambda_w + \frac{\lambda_g}{MRF}, \quad (6.2)$$

where κ_{rw} and κ_{rg} are the water and gas relative permeability functions, respectively. MRF represents the mobility reduction factor that models the effects of foam bubbles in the displacement of water and (foamed) gas. Linking the total mobility definition [86, 60] with the two-phase flow (averaged) Darcy's law, the apparent viscosity of the mixture (water and foamed gas) is defined as:

$$\mu_{app} = \left(\lambda_w + \frac{\lambda_g}{MRF} \right)^{-1}, \quad (6.3)$$

which gives the following expression for the mobility reduction factor a function of apparent viscosity, foam quality, and gas mobility

$$MRF = \frac{\lambda_g}{f_g} \mu_{app}. \quad (6.4)$$

6.2.2 Foam model

Semi-empirical models of foam flow in local equilibrium, like the CMG-STARS simulator, consider the effects of foam via the mobility reduction factor that affects gas mobility. An important feature of this model is the distinction between two flowing regimes in steady-state flow: low-quality (LQR) and high-quality (HQR) regimes. In the foam modeling used in STARS, MRF may include the effects of water saturation, oil saturation, surfactant concentration, gas velocity, and critical capillary number [109, 3, 78]. However, in this work, we focus on two effects: the dry-out function (F_{water}), related to the water saturation, and the shear-thinning function (F_{shear}), which are introduced in the MRF as follows:

$$\begin{aligned} MRF &= 1 + fmmob F_{water} F_{shear}, \\ F_{water} &= \frac{1}{2} + \frac{1}{\pi} \arctg(sfbet(S_w - SF)), \\ F_{shear} &= \begin{cases} \left(\frac{fmcap}{N_{ca}} \right)^{epcap}, & \text{if } N_{ca} \geq fmcap, \\ 1 & \text{if } N_{ca} < fmcap. \end{cases} \end{aligned} \quad (6.5)$$

The capillary number is evaluated using:

$$N_{ca} = \frac{\mu_{app} u}{\sigma}, \quad (6.6)$$

where u and σ are the inflow velocity (Darcy’s velocity) and the water–gas surface tension, respectively.

The model parameters are $fmmob$, $sfbet$, SF , $epcap$, and $fmcap$. The parameter $fmmob$ is the maximum mobility reduction that can be achieved considering the effects of foam, $sfbet$ is a value representing the transition between LQR and HQR regimes (higher values of $sfbet$ represent a sharp transition, while smaller values of $sfbet$ will produce a smooth transition), and SF corresponds to the water saturation where the capillary pressure meets a critical value collapsing the foam bubbles. The value of $epcap$ characterizes the foam rheology as Newtonian or non–Newtonian, and $fmcap$ defines the smallest capillary number expected to be encountered by foam in the simulation. Although the value of $fmcap$ may influence the other parameters, it is usually not treated as a parameter during the calibration and its values is set to the lowest capillary number expected, as described in [13, 45, 79].

6.2.3 Datasets

Experimental datasets from the literature were considered in this work to explore the proposed approach for parameter estimation. In particular, we considered two synthetic cases with known parameters to explore the capabilities of the methods in recovering the true (ground truth) parameters, and also two datasets from the literature [78, 104]. The four datasets employed different commercial surfactants and have well–defined rheology presenting non–Newtonian behavior with shear–thinning. These datasets are described in more detail next.

Synthetic datasets #1 and #2

Initially, two synthetic datasets were considered, one with a sharp and another with a smoother LQR–HQR transition. In the first case a value of $sfbet = 500$ was used to represent a sharp transition, whereas on the second case $sfbet = 50$ was considered.

Kapetas *et al.* (2016)

The experimental data from this dataset was taken from the foam quality scan presented in [78]. In particular, the test case used in this manuscript corresponds to the experimental measurements observed at $20^\circ C$. The fluids employed were brine and Nitrogen and the surfactant solution used was an Alpha Olefin Sulfonate (AOS, Bio–Terge 14–16C, Stepan Chemical Co.). In the original work, the authors evaluated the effects of

the same surfactant solution at different operative temperatures (20 – 40 – 60 – 80 °C). The experimental observations registered at 20 °C reported the highest values of apparent viscosity for all the considered foam qualities. The same trend is recognized for the surface tension measurement and predictions. In [78] it is mentioned that the experimental observations presented shear-thinning effects after recognizing the maps between pressure drop and gas-velocity.

Moradi–Araghi *et al.* (1997)

An experimental dataset from [104] was also considered. In particular, we refer to the test rig labeled as RF1, where the foaming agent was a commercial surfactant known as CD-1050 developed by Chaser in a synthetic South Cowden brine. The gas-phase was CO₂, and the experimental temperature was fixed at 36 °C. The authors reported that the RF1-core sample achieved steady states of pressure drop much faster than other core samples; this is motivated by the selective mobility reduction in high permeability cores. In addition to this, the authors reported in [104] that they observed shear thinning behavior. The flowing conditions (i.e., inflow velocity and water-gas surface tension) were taken from the recent works [45, 12, 13, 95] that explored the same experimental dataset.

Table 8 summarizes the core sample and fluid properties of the datasets used in this work. The core samples' absolute permeabilities vary significantly among the datasets to show the robustness of the calibration procedure without loss of generality. Relative permeability parameters are not considered within the parameter estimation process, although they are remarkably influential on the modeling and simulation [138, 8, 9]. Corey relative permeabilities are rather taken from the corresponding sources and are also reported in Table 8.

Table 8 – Overview of input parameters for all investigations of this study.

Parameter	Synthetic	Kapetas (2016)	Moradi–Araghi (1997)
μ_w [Pa s]	7×10^{-4}	1×10^{-3}	6.5×10^{-4}
μ_g [Pa s]	2×10^{-5}	2×10^{-5}	5×10^{-5}
σ [N/m]	3×10^{-2}	2.81×10^{-2}	5×10^{-3}
u [m/s]	98.819×10^{-6}	1.383×10^{-5}	1.763×10^{-5}
κ [m ²]	5.23×10^{-13}	1.67×10^{-12}	5.44×10^{-13}
ϕ	0.18	0.24	0.18
S_{wc}	0.20	0.25	0.10
S_{gr}	0.20	0.20	0.05
n_w	4.20	2.86	4.00
n_g	1.30	0.70	1.83
K_w^0	0.20	0.39	0.22
K_g^0	0.94	0.59	1.00

6.2.4 Parameter estimation

In the literature, different methods to calibrate the MRF parameters using foam scan experimental data have been reported. Boeije & Rossen [12, 13] proposed a manual procedure that works independently for each foam quality regime. Ma *et al.* [98] and Farajzadeh *et al.* [45] proposed a weighted least squares method that captures accurately enough the flowing regime transition. In a similar study, Lotfollahi *et al.* [95] presented least-squares optimization to fit the parameters of many different SE and PB models. Recently, Gassara *et al.* [51] and Cavalcante-Filho *et al.* [48] reported results that fit the same experimental dataset for different population balance models. Motivated by the difficulties of obtaining unique results, Zeng *et al.* [148] presented a staggered method to determine the best fit values for different CMG-STARs configurations using different experimental datasets.

In this work, three different objective functions \mathcal{X}^2 for minimizing the sum of the squared differences between experimental data and model predictions are considered for parameter estimation. The different objective functions differ from each other in terms of the type of experimental data used. The first objective function (OF1) is given by:

$$\mathcal{X}_\mu^2 = \sum_{k=1}^{Np} \left(\frac{\mu_{app,k}^{exp} - \mu_{app,k}^{model}(\boldsymbol{\theta})}{\sigma(\mu_{app,k}^{exp})} \right)^2, \quad (6.7)$$

where Np is the number of experimental observations, μ_{app}^{exp} denote experimental observations, $\mu_{app}^{model}(\boldsymbol{\theta})$ denote model evaluations, and the term $\sigma(\mu_{app,k}^{exp})$ represents the experimental variability. It is important to remark that \mathcal{X}_μ^2 is the objective function traditionally employed in the literature [45, 95, 98, 97] in the context of nonlinear least squares methods for estimating foam model parameters.

Next, we introduce two objective functions considering that MRF can be directly computed from experimental data using Equation (6.4). The second objective function (OF2) computes the sum of squared differences between the experimental evaluations of the mobility reduction factor represented with Equation (6.4) with the model evaluations obtained by Equation (6.5). Thus, the second objective function \mathcal{X}_{MRF}^2 is written as follows

$$\mathcal{X}_{MRF}^2 = \sum_{k=1}^{Np} \left(\frac{MRF_k^{exp} - MRF_k^{model}(\boldsymbol{\theta})}{\sigma(MRF_k^{exp})} \right)^2, \quad (6.8)$$

where $\sigma(MRF_k^{exp})$ represents the experimental variability of the mobility reduction factor.

The third objective function (OF3) combines the objective functions \mathcal{X}_μ^2 and \mathcal{X}_{MRF}^2 , and is given by the following expression:

$$\mathcal{X}_{\mu,MRF}^2 = \sum_{k=1}^{Np} \left(\frac{\mu_{app,k}^{exp} - \mu_{app,k}^{model}(\boldsymbol{\theta})}{\sigma(\mu_{app,k}^{exp})} \right)^2 + \left(\frac{MRF_k^{exp} - MRF_k^{model}(\boldsymbol{\theta})}{\sigma(MRF_k^{exp})} \right)^2. \quad (6.9)$$

Note that OF3 not only considers apparent viscosity from experimental data as given by (6.1), but also employs information provided by equation (6.4) about the mobility reduction factor. We remark that this information does not require additional experimental realizations and can improve parameter estimation, as will be shown.

The model parameters are usually estimated [97, 98, 45] using nonlinear least squares methods, such as the Levenberg–Marquadt (LM) method, to obtain

$$\hat{\boldsymbol{\theta}} = \operatorname{argmin} [\mathcal{X}^2(\boldsymbol{\theta})], \quad (6.10)$$

the best–fit set of parameters that minimizes the chosen objective function.

We remark that in the literature [98, 97, 45, 95] the parameter estimation procedure has been limited to apply the objective function \mathcal{X}_μ^2 . In this work, we will show that the objective function $\mathcal{X}_{\mu, MRF}^2$ can improve the parameter estimation process.

6.2.5 Bayesian estimation

Parameter estimation using Bayesian methods such as the Markov Chain Monte Carlo (MCMC) method [17, 18] can provide good estimates and additional insights about the parameters of the model, as reported previously for estimation of foam model parameters [137] and relative permeability parameters [138, 9, 8].

The MCMC method relies on the Bayes’ rule for the estimation of the distribution of the model parameters, which is given by:

$$\mathbb{P}(\boldsymbol{\theta}|D) = \frac{\mathbb{P}(D|\boldsymbol{\theta}) \mathbb{P}(\boldsymbol{\theta})}{\mathbb{P}(D)}. \quad (6.11)$$

Considering the foam model parameters $\boldsymbol{\theta}$ and the dataset D , we denote by $\mathbb{P}(\boldsymbol{\theta})$ the prior distribution which encodes our prior knowledge about the parameters and $\mathbb{P}(D)$ is the evidence that the data was generated by this model. The MCMC estimates $\mathbb{P}(\boldsymbol{\theta}|D)$ which represents the posterior probability distribution of the parameters given the observed data. To describe how probable are the observed data for a specific parameter set, a likelihood function $\mathbb{P}(D|\boldsymbol{\theta})$ is defined.

Considering the objective functions described before, two likelihood functions were used in this work. The first likelihood function is associated to OF1 (\mathcal{X}_μ^2) and OF2 (\mathcal{X}_{MRF}^2), and is given by:

$$\mathcal{L}(\mathcal{M}|\mu, \sigma) = \frac{1}{4\sigma\sqrt{\pi}} \exp\left(-\left[\frac{\mathcal{M} - \mu}{2\sigma}\right]^2\right), \quad (6.12)$$

where \mathcal{M} represents the model evaluation, μ is the observed data mean value and σ is the standard deviation. Here, the model evaluation and observed data correspond to μ_{app} or MRF accordingly to the objective function used. The next multivariate normal likelihood

function [121] was used for the objective function $\mathcal{X}_{\mu, MRF}^2$:

$$\mathcal{L}(\mathbf{M}|\boldsymbol{\mu}, \mathbf{Cov}) = \frac{\det(\mathbf{Cov})^{-1}}{(2\pi)^{Np/2}} \exp\left(-\frac{1}{2}(\mathbf{M} - \boldsymbol{\mu})^T \mathbf{Cov}^{-1}(\mathbf{M} - \boldsymbol{\mu})\right), \quad (6.13)$$

where \mathbf{M} and $\boldsymbol{\mu}$ are vectors containing more than one model evaluation and experimental observation's expected value, respectively. The covariance matrix \mathbf{Cov} is evaluated considering apparent viscosity and mobility reduction factor data, and affected by the experimental error.

For all parameters of the foam model studied here, a uniform distribution was taken as its prior distribution considering physical ranges of the parameters and available knowledge from the literature [3, 78, 95]. The SF parameter is the only one which has clear physical limits defined by $S_{wc} \leq SF \leq 1 - S_{gr}$, where S_{wc} and S_{gr} are the connate water and residual gas saturation, respectively. The only restriction on the other parameters is that they should be greater than zero. In practical terms, the uniform distribution of these parameters were bounded, as described in Table 9, without any loss of generality.

Table 9 – Prior distributions of the parameters in the STARS non-Newtonian foam model used for Bayesian estimation.

Parameter	fmmob	SF	sfbet	epcap
Synthetic datasets	$\mathcal{U}(1, 300000)$	$\mathcal{U}(0.2, 0.8)$	$\mathcal{U}(10, 10000)$	$\mathcal{U}(0, 2)$
Kapetas (2016)	$\mathcal{U}(1, 200000)$	$\mathcal{U}(0.25, 0.8)$	$\mathcal{U}(10, 3000)$	$\mathcal{U}(0, 5)$
Moradi-Araghi (1997)	$\mathcal{U}(10, 40000)$	$\mathcal{U}(0.1, 0.95)$	$\mathcal{U}(10, 200)$	$\mathcal{U}(0, 1)$

The MCMC implemented in the Python library `PyMC3` with the `SLICE` sampler [121] was used for all Bayesian parameter estimations presented in this work.

6.2.6 Identifiability analysis

A crucial step during parameter estimation process is to examine parameter identifiability, which assess whether or not a set of parameters can be uniquely estimated for a given model and data set. The works of Raue *et al.* [115], Rannala *et al.* [114] as well as Kao *et al.* [77] states that a model parameter can be classified as (i) identifiable, (ii) practically non-identifiable, and (iii) structurally non-identifiable. Structural non-identifiability is related to the mathematical structure of the model, whereas practical non-identifiability is related to the quality of the observed data. Consequently, the identifiability of a model parameter depends on the quality of the experimental data as well as the structure of the model; for instance, over parametrized models are susceptible to be non-identifiable [77].

One approach to perform parameter identifiability analysis is the concept of profile likelihood [115], which we introduce as follows. For any model parameter θ_i , the associated

profile likelihood is given by:

$$\mathcal{X}_{PL}^2(\theta_i) = \min [\mathcal{X}^2(\boldsymbol{\theta})]_{\boldsymbol{\theta} \setminus \{\theta_i\}}, \quad (6.14)$$

where $\mathcal{X}_{PL}(\theta_i)$ stores the residual values after fixing $\theta_i \in [\min(\theta_i), \max(\theta_i)]$ and fitting the remaining model parameters $\boldsymbol{\theta} \setminus \{\theta_i\}$. $\mathcal{X}^2(\boldsymbol{\theta})$ takes any of the functional representations described in Equations (6.7)-(6.9).

A model is identifiable if the profile likelihood function described by Equation (6.14) presents a single minimal value [116, 77]. A model parameter θ_i is structural non-identifiable if the associated profile likelihood remains flat or shallow in the entire search range $[\min(\theta_i), \max(\theta_i)]$. Practical non-identifiable parameters have profile likelihood functions that contain a minimal value, yet it is not necessarily unique or the curvature of its likelihood profile is shallow.

Practical non-identifiability issues associated with the model parameter θ_i may be corrected, restricting the range $[\min(\theta_i), \max(\theta_i)]$ where the best fit value is being explored. Alternatively, practical non-identifiability issues are suitable to be reduced if the quality of the experimental data is improved. Another solution to mitigate practical non-identifiability issues is fixing "redundant" model parameters. In this manuscript, we will explore the alternative of improving the experimental data employed to perform the model calibration.

6.2.7 Uncertainty quantification and sensitivity analysis

Once the posterior distributions are determined for all the models' input parameters using the experimental data, the propagation of such uncertainties to the foam flow model can be carried out (forward UQ). The Monte Carlo method was employed to perform this task by simply taking the samples obtained from the posterior distributions obtained by the MCMC method. Expected value, variance, and the 90% prediction interval were computed to characterize the quantities of interest.

Global (variance based) sensitivity analysis based on Sobol sensitivity indices [127, 120] was used to assess how an input parameters $\theta_i \in \boldsymbol{\theta}$ and also interactions between them contribute to a particular output quantity \mathcal{Y} . Sobol indices were computed with the SALib package using the Saltelli sampler algorithm [63].

6.3 Results

6.3.1 Synthetic datasets

First we present the results using two synthetic datasets to show the capabilities of the proposed methodology to perform the model calibration and estimate the variability of different output quantities. The two synthetic datasets are mainly based on core and

fluid properties from the literature [3, 95]. The only difference in the datasets #1 and #2 is the parameter $sfbet$ controlling how smooth is the transition between LQR and HQR. In both cases a Gaussian noise of 5% was added to the synthetic data to explore the robustness of the parameter estimation.

Synthetic dataset #1

To evaluate identifiability issues on the parameters and whether including MRF in the objective functions could enhance it, we computed profile likelihood for all the objective functions. The results are shown in Figure 36. One can notice that the profile likelihood using the objective functions OF2 and OF3 are identifiable with clear minima, which are in good agreement with the ground truth parameters. The OF1, however, highlights difficulty for the identification of $fmmob$ and $epcap$ as can be observed in their flat profiles.

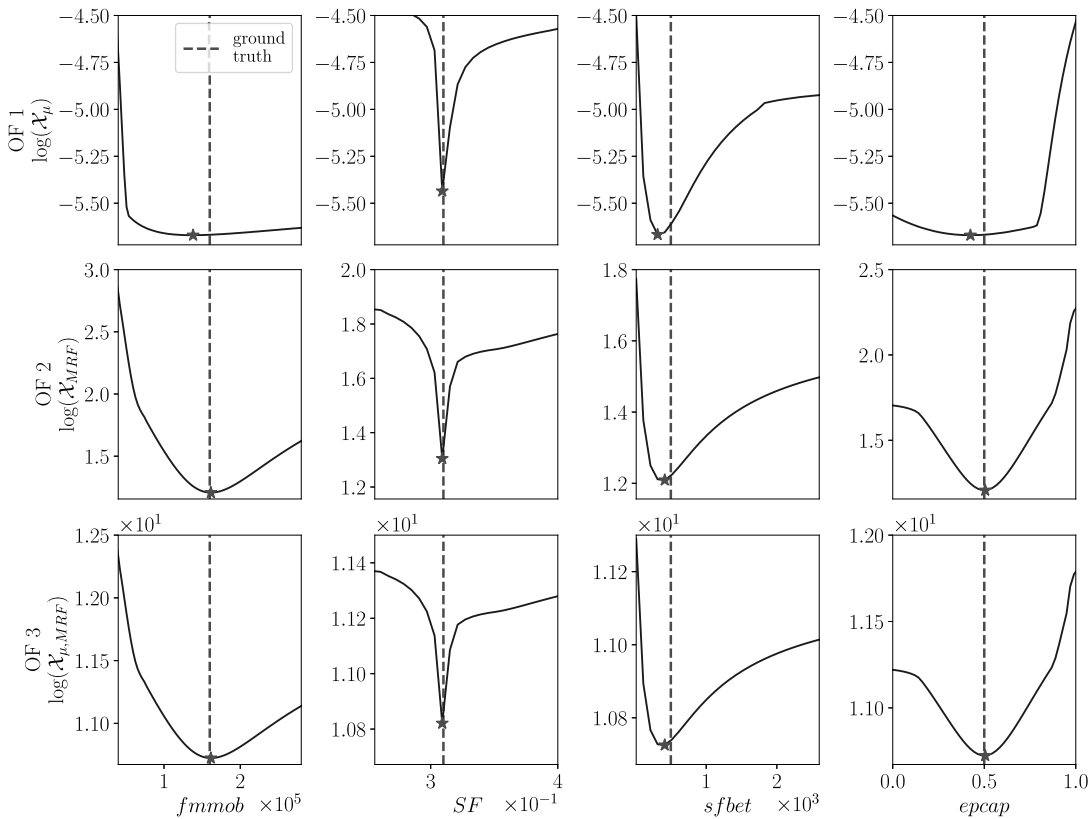


Figure 36 – Profile likelihood for the synthetic dataset #1 considering the different objective functions. Red stars correspond to the minimum and dashed green line to the ground truth parameter set.

The posterior PDFs obtained by MCMC for the foam parameters are shown in Figure 37 together with the ground truth parameter set. The posterior density distributions obtained using OF2 and OF3 properly tail out to zero, ensuring that the parametric uncertainty is not overestimated. Note that the posterior PDF obtained with the OF3 is

more restricted, indicating a better identification of the parameters. The posterior PDF obtained using OF1 also tails out to zero, except for the *fmmob* posterior. The practical non-identifiability of *fmmob* and *epcap*, previously observed via the profile likelihood, translates in wider posterior PDFs, resulting in more uncertainty.

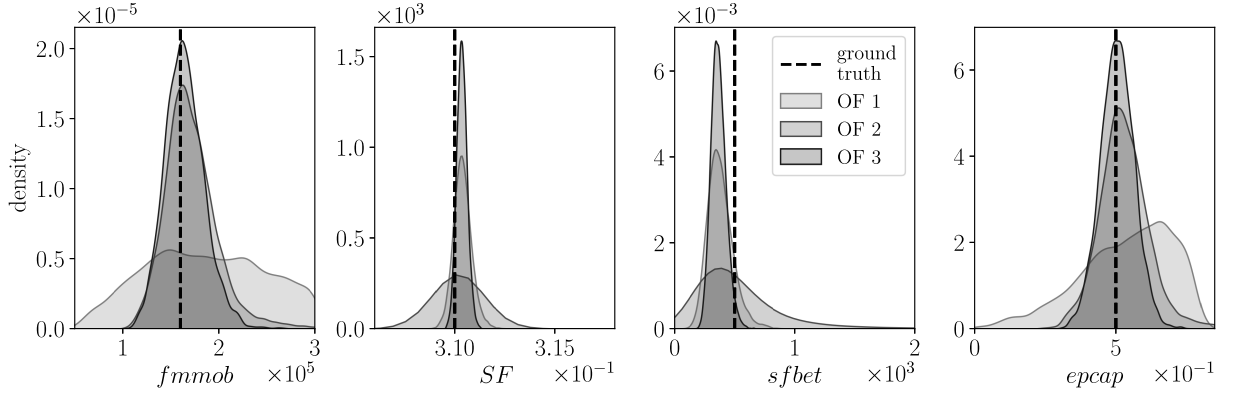


Figure 37 – Posterior PDFs obtained for the synthetic dataset #1.

The expected values of the parameters obtained for each objective function and the ground truth is presented in Table 10 for the synthetic dataset #1. Clearly objective function 3 delivers better estimates when compared to the other objective functions, specially for *fmmob* and *epcap* parameters.

Table 10 – Non-Newtonian model parameters calibrated to fit the synthetic dataset #1.

Parameters	fmmob	SF	sfbet	epcap
Ground Truth	1.60e+05	3.10e-01	5.00e+02	5.00e-01
OF1	1.87e+05	3.10e-01	3.85e+02	5.37e-01
OF2	1.72e+05	3.09e-01	7.22e+02	5.30e-01
OF3	1.65e+05	3.10e-01	3.71e+02	5.06e-01

Figure 38 shows the results of uncertainty propagation for apparent viscosity and mobility reduction factor as functions of the foam quality. For the apparent viscosity, the OF1 exposes uncertainty on both foam quality regimes, whereas the OF2 presents more uncertainty in the high-quality regime. Clearly, the uncertainty propagation pattern obtained using the MCMC samples associated with the objective function OF3 presents less uncertainty in both regimes than the other objective functions. For the mobility reduction factor, we can observe more uncertainty using the objective function OF1 in the LQR, while for the OF2 there is more uncertainty in the HQR. The uncertainty propagation for the OF3 presents less uncertainty on almost all foam quality values, as expected since OF3 represents a combination of the other two objective functions.

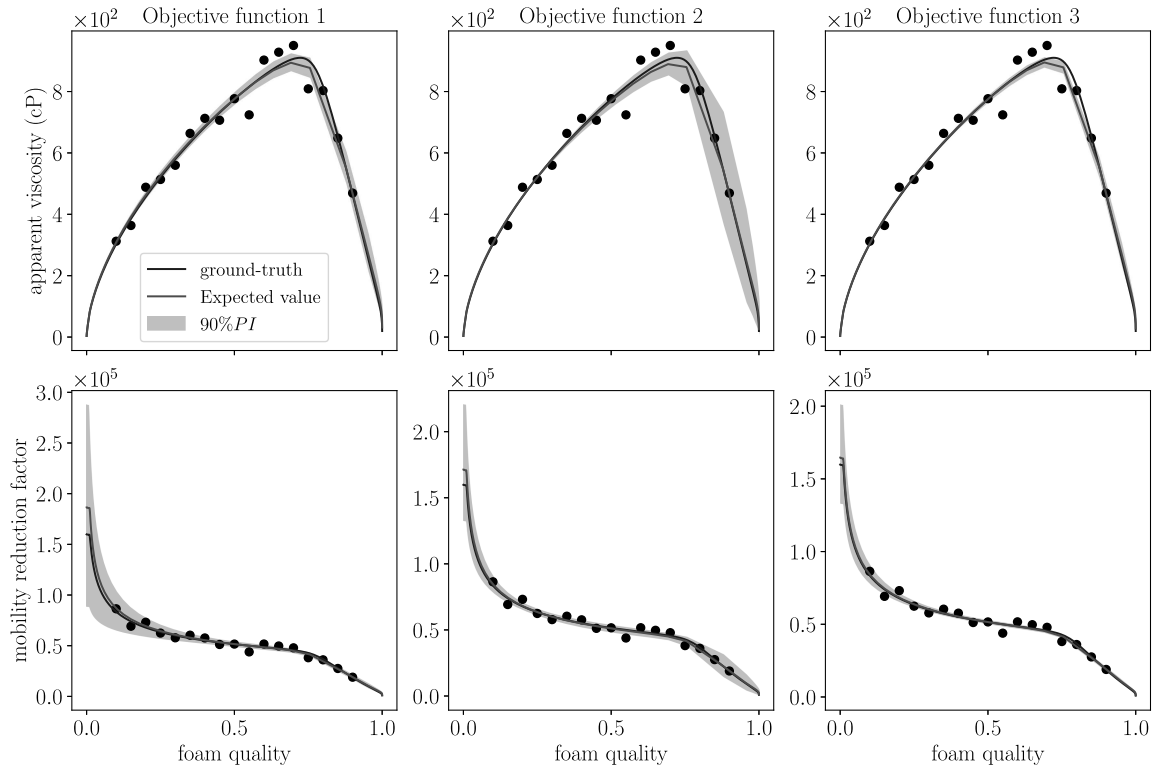


Figure 38 – Forward uncertainty quantification in terms of apparent viscosity and mobility reduction factor for the synthetic dataset # 1.

Synthetic dataset #2

This case consists of modifying the previous synthetic dataset #1, where the $sfbet$ parameter that controls the foam quality regime’s transition sharpness is significantly reduced. The remaining parameters were unchanged. In this case, the LQR–HQR transition is smoother than the previous dataset. Again, a Gaussian noise of 5% relative to the experimental measurements of apparent viscosity was considered.

Figure 39 shows the profile likelihood evaluated with the different objective functions. In particular, we observe flat profiles for $fmmob$ and $epcap$, meaning difficulties in estimating unique values for these using OF1. Also, note that the minimum value obtained for the $sfbet$ parameter is not as good in the synthetic case #1. On a different take, the profile likelihoods obtained with the objective functions OF2 and OF3 show explicit unique minimal values.

The posterior density distributions obtained with the MCMC method for each objective function are depicted in Figure 40. In particular, we can observe that the worst calibration results correspond to the MCMC samples obtained with OF2 and OF1. Non–negligible misfits are observed between the ground–truth values and the mean value of each distribution. In particular, we observe problems to constrain the variability of the parameters. Note that the OF2, which only considers MRF data for the likelihood, is not

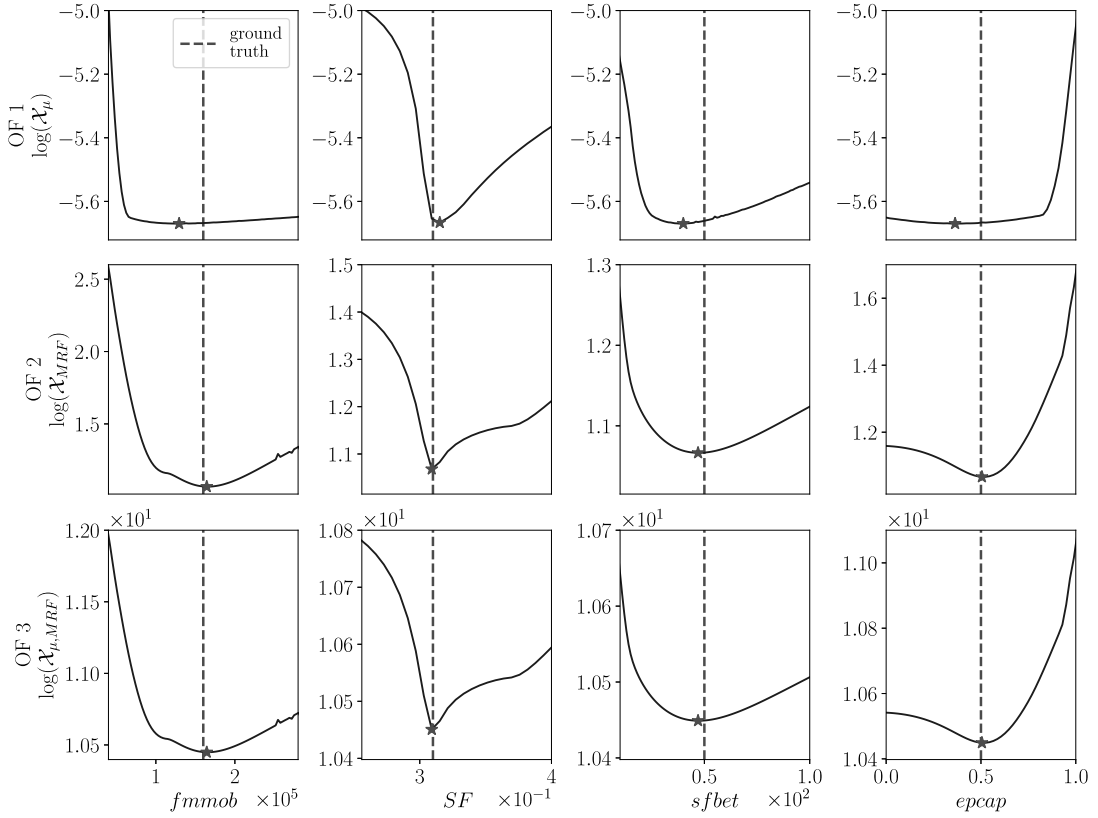


Figure 39 – Profile likelihood comparison analyzing the best fit configurations of the Synthetic dataset #2. Red stars correspond to the minimum.

sufficient to obtain a reasonable estimation of $sfbet$. Nevertheless, the posterior density distributions obtained with OF3 are clustered around the ground–truth reference values and tail to zero for all parameters, ensuring a small degree of uncertainty.

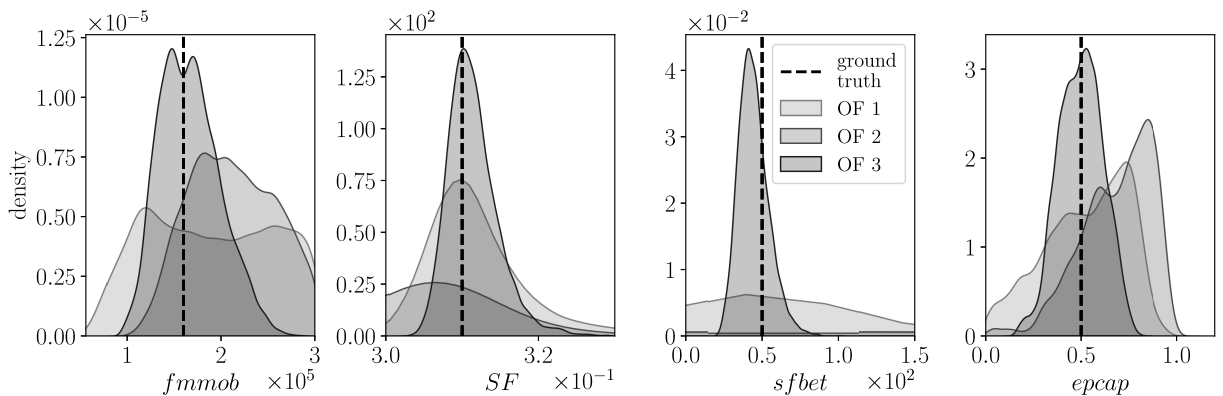


Figure 40 – Posterior density distributions obtained employing the objective functions OF1, OF2, and OF3; employing the Synthetic dataset #2.

Table 11 shows the expected values of the model parameters. The problems related to the density distributions employing the objective function OF2 are reflected in Table 11, where we can observe the poor estimates for $fmmob$, SF , and $sfbet$. Nevertheless, the

results associated with the objective function OF3 show the best results possible for all the parameters.

Table 11 – Non-Newtonian model parameters calibrated to fit the synthetic dataset # 2.

Parameters	fmmob	SF	sfbet	epcap
Ground Truth	1.60e+05	3.10e-01	5.00e+01	5.00e-01
OF1	1.89e+05	3.13e-01	7.76e+01	5.28e-01
OF2	2.12e+05	2.84e-01	2.38e+03	6.85e-01
OF3	1.67e+05	3.11e-01	4.48e+01	4.98e-01

Figure 41 shows the uncertainty propagation analyzing the apparent viscosity and mobility reduction factor as functions of the foam quality. The uncertainty pattern obtained considering the MCMC samples associated with the objective function OF2 propagates variability preferentially on the HQR. Differently, the uncertainty propagation related to OF1 and OF3 presented fewer uncertainties, reproducing with the expected values the ground-truth model evaluations. In addition, the model evaluations related to the objective function OF3 possess the lowest variability when recovering the ground-truth behavior. Concerning mobility reduction factor (lower panel of Figure 41), we can observe significant variability on the LQR for the objective function 1. A similar uncertainty pattern is observed on the UQ analysis for OF3, yet showing less variability. For OF2, one can note that the uncertainty is clustered on the lowest foam quality and highest foam quality values.

6.3.2 Experimental data from Kapetas *et al.* (2016)

Figure 42 shows the posterior PDFs obtained after executing the MCMC method employing different likelihood functions for the Kapetas *et al.* (2016) dataset. In particular, we can observe problems to estimate the variability of the *fmmob* parameter using the objective function OF1. The same problems are recognized on the density distributions for the parameters *SF* and *sfbet* when adopting the objective function OF2. The objective function OF3 results in proper shapes that tail to zero, ensuring low uncertainty for the estimated parameters.

Figure 43 shows the uncertainty propagation employing the MCMC samples obtained using different likelihood functions. The likelihood function OF1 propagates less variability to the apparent viscosity than to the mobility reduction factor. In contrast to this behavior, the likelihood function OF2 propagates less variability to the mobility reduction factor than to the apparent viscosity. As expected, the results related to OF3 combine the features of the other two cases, without excessive uncertainties in both apparent viscosity and mobility reduction factor, the only exception being at very low f_g values for mobility reduction factor.

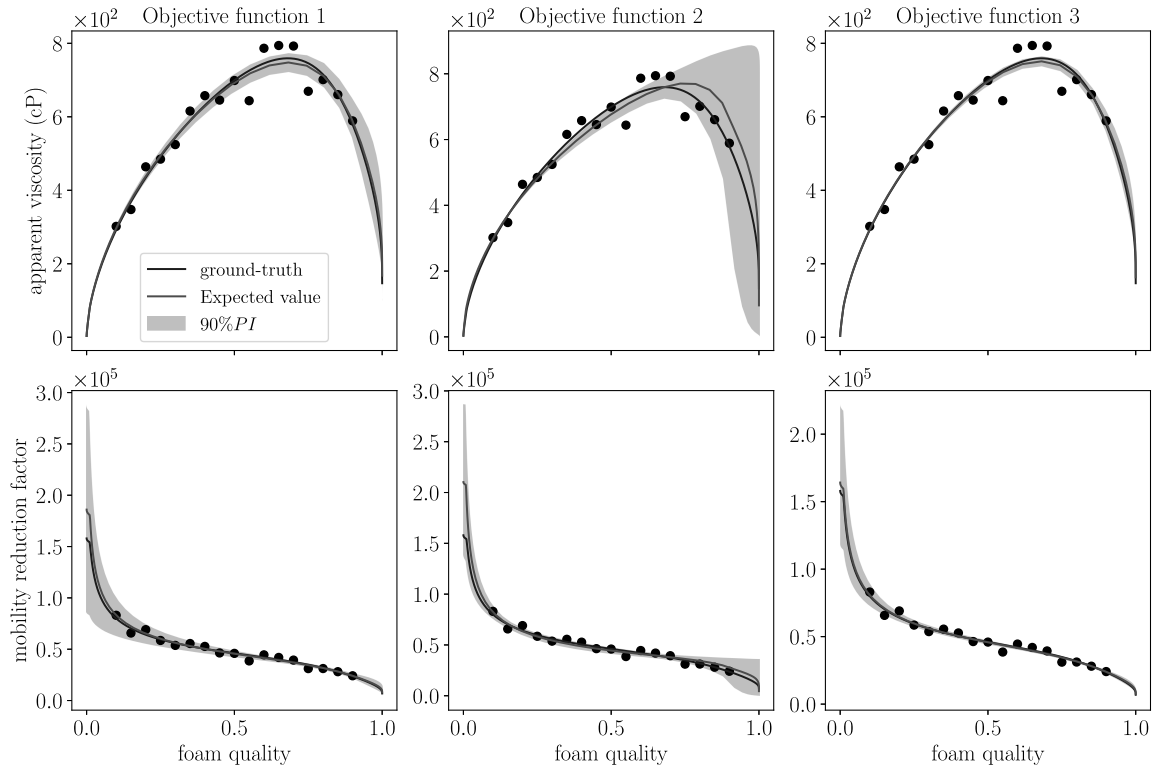


Figure 41 – Forward uncertainty quantification in terms of apparent viscosity and mobility reduction factor for the synthetic dataset #2.

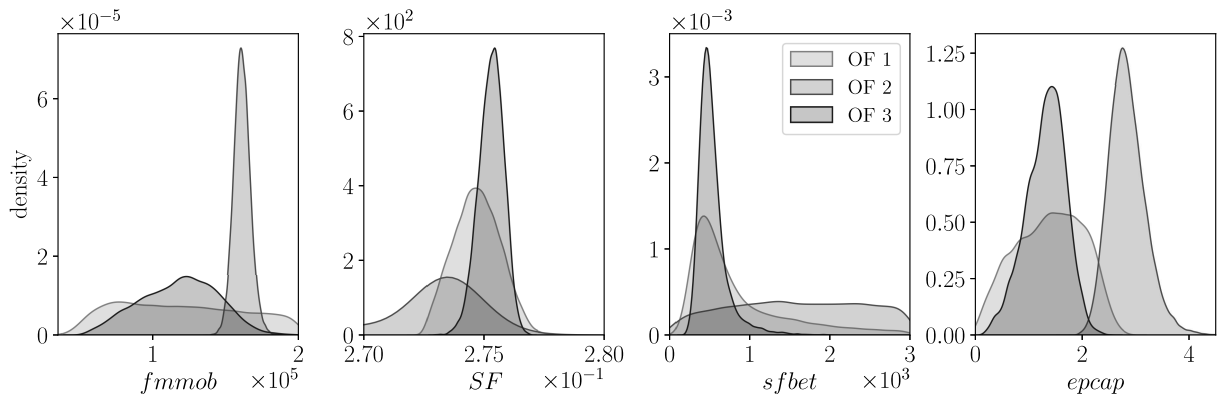


Figure 42 – Posterior density distributions obtained employing the objective functions OF1, OF2, and OF3; employing the Kapetas *et al.* (2016) dataset.

6.3.3 Experimental data from Moradi–Araghi *et al.* (1997)

Figure 44 shows the density distribution function obtained employing different likelihood functions. Figure 44 present proper density distributions for all the parameters, ensuring that the variability is not over estimated. Note, however, the multi-modal behavior for the parameters $fmmob$ and $epcap$. The three likelihood functions returns proper density distributions associated to the parameters SF and $sfbet$.

Figure 45 presents the uncertainty propagation, adopting MCMC samples obtained

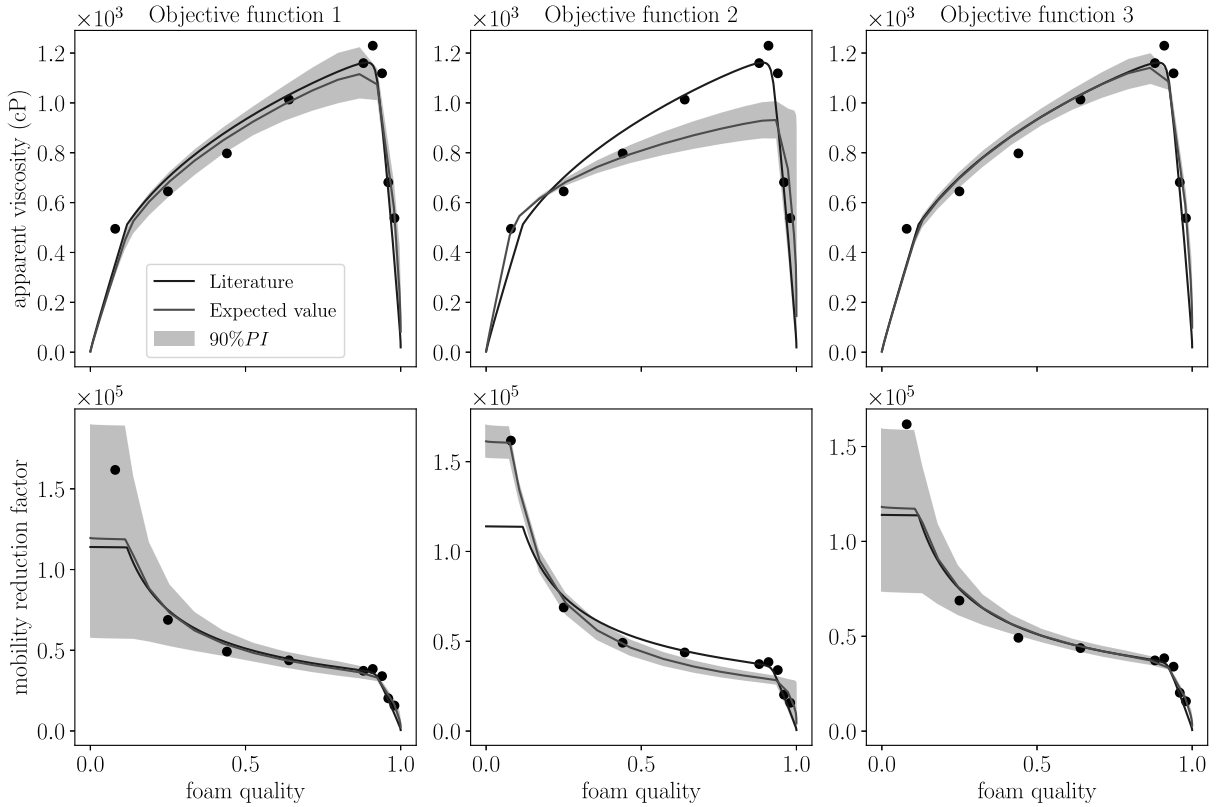


Figure 43 – Forward uncertainty quantification in terms of apparent viscosity and mobility reduction factor for Kapetas *et al.* (2016) dataset. Top row: uncertainty propagation for the apparent viscosity as function of the foam quality. Bottom row: uncertainty propagation for the mobility reduction factor as function of the foam quality.

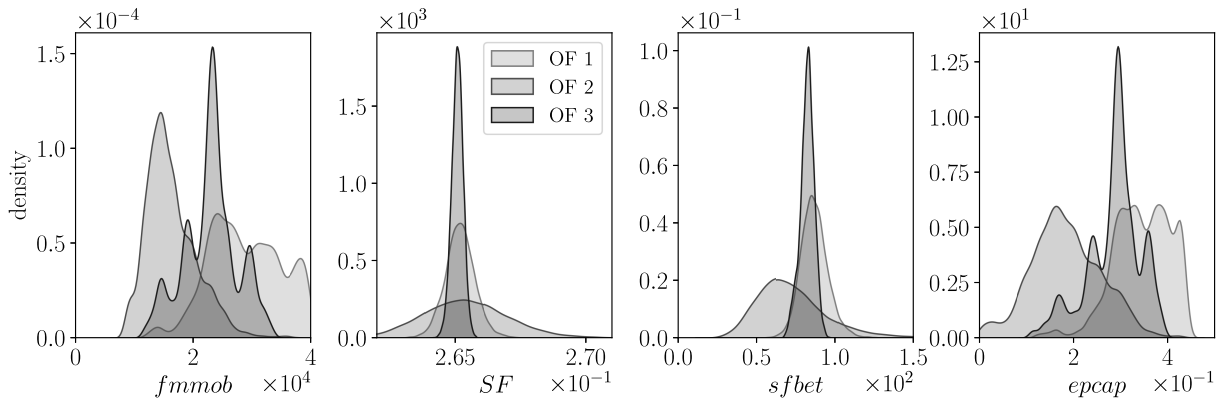


Figure 44 – Posterior density distributions obtained employing the objective functions OF1, OF2, and OF3; employing the Moradi–Araghi *et al.* (1997) dataset.

after using different likelihood functions. We generally observe low variability on apparent viscosity for the samples obtained with OF1 and OF3 and note higher uncertainties when using the OF2 samples in the HQR. For the MRF, we note that most of the uncertainty is propagated to the LQR.

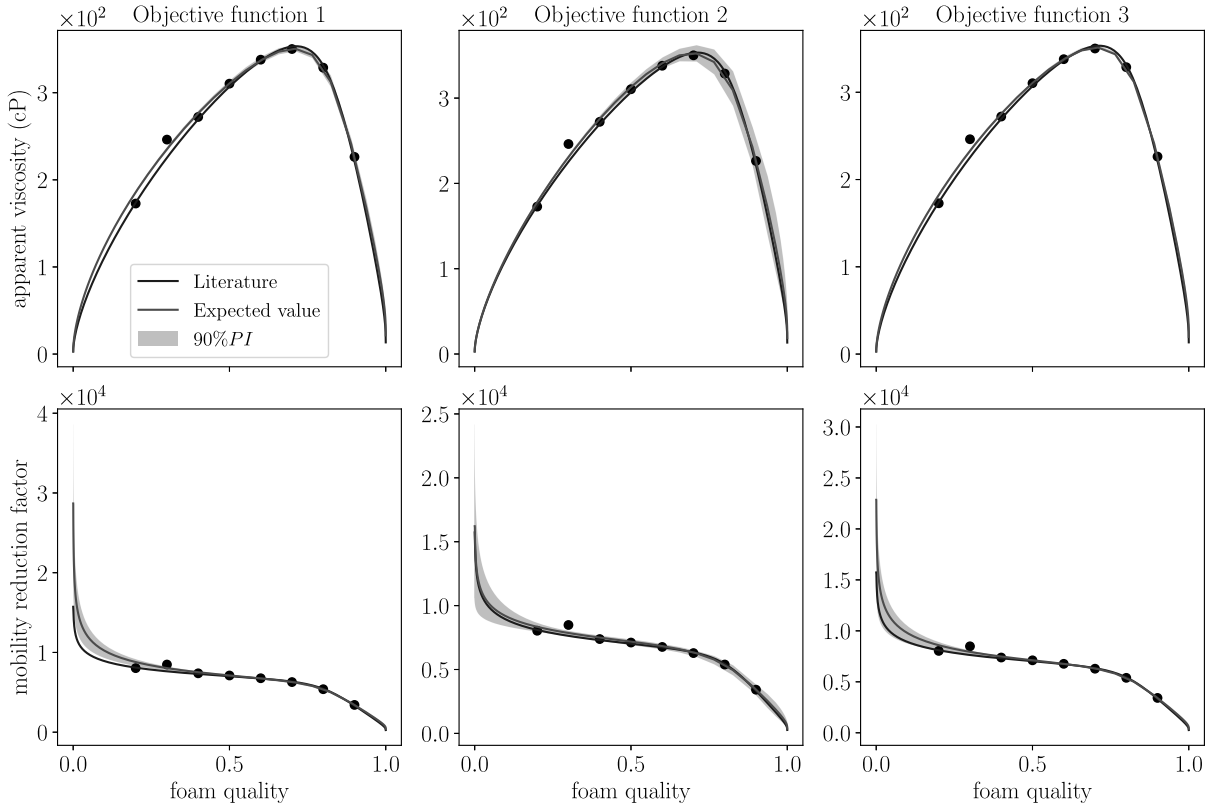


Figure 45 – Summary of forward uncertainty quantification and sensitivity analysis results considering the Moradi–Araghi *et al.* (1997) dataset, comparing the three objective functions. Top row: uncertainty propagation for the apparent viscosity as function of the foam quality. Bottom row: uncertainty propagation for the mobility reduction factor as function of the foam quality.

6.4 Discussion

The synthetic datasets were used to show that the model calibration quality relies strongly on the objective function and experimental data used. The objective function OF1 shows limitations to reproduce the ground truth behavior, whereas the objective function OF2 shows promising capabilities to solve the synthetic dataset #1. Nevertheless, the objective function OF3 was the only one that could reproduce both synthetic datasets accurately.

The identifiability analysis showed that key parameters, $fmmob$ and $epcap$, are practically non-identifiable when the traditional objective function OF1 is used. This is remediated when using the MRF as experimental data in the objective functions OF2 and OF3. The inverse UQ analysis revealed a similar trend. The PDFs for $fmmob$ and $epcap$ recovered by the MCMC method had narrower compact support with OF2 and OF3 than when using OF1, i.e., low uncertainty. However, here we have a tradeoff since the opposite was observed for the parameters SF and $sfbet$.

Finally, the forward UQ results revealed how the experimental data of apparent viscosity and MRF complement each other. The results obtained with OF1 consistently showed low uncertainty in the apparent viscosity but very high uncertainty in the MRF for LQR. This is likely due to the mathematical structure of apparent viscosity. In the LQR, total mobility (the inverse of apparent viscosity) is dominated by water mobility. This way, any uncertainty in the MRF at LQR is filtered out of μ_{app} . On the other hand, small uncertainties in the MRF appear amplified in the apparent viscosity in the HQR. These two situations were consistently observed and suggest why the combination of the two experimental data, MRF and μ_{app} , in the objective function OF3 generated the best calibrations with high fidelity and lowest uncertainty.

6.4.1 Sensitivity analysis

Figure 46 presents the results of a sensitivity analysis based on Sobol indices for the synthetic dataset #1. The SA study was carried out using the range of the parameters estimated from the MCMC for each objective function. The results of SA for the other cases (synthetic data #2, Kapetas *et al.* (2016), and Moradi–Araghi *et al.* (1997)) are very similar, and therefore are not reported here for the sake of compactness.

The reported sensitivities for apparent viscosity and mobility reduction factor are very similar. For instance it is possible to recognize that the parameters $fmmob$ and $epcap$ are responsible for most of the uncertainty in the QoIs. In particular the effects of $epcap$ are important mostly in the LQR part of the diagram, while $fmmob$ has a significant impact in the entire foam quality range. We can observe that the parameters SF and $fbet$ are more relevant on the HQR.

We can also observe from Figure 46 that the parameter $epcap$, controlling shear-thinning effects, has a significant impact on both apparent viscosity and mobility reduction factor in a wide range of foam qualities. In particular, the impact of $epcap$ on MRF explains why including its data on the parameter estimation process improves the estimation of parameters for this non-Newtonian case.

The fact that the total Sobol indices are higher than the main indices in the results for objective function 1 indicates interactions between the parameters $fmmob$ and $epcap$. These interactions are smaller for the objective function 2, and almost negligible for the objective function 3. Parameter interactions can cause model parameters to be not uniquely identifiable. In fact, this was noticed before in density distributions presented in Figure 37 and shallow profile likelihood in Figure 36.

6.5 Conclusions

In this work, we studied the problem of parameter estimation and identifiability for non-Newtonian foam models in two-phase flow in porous media. We proposed a new

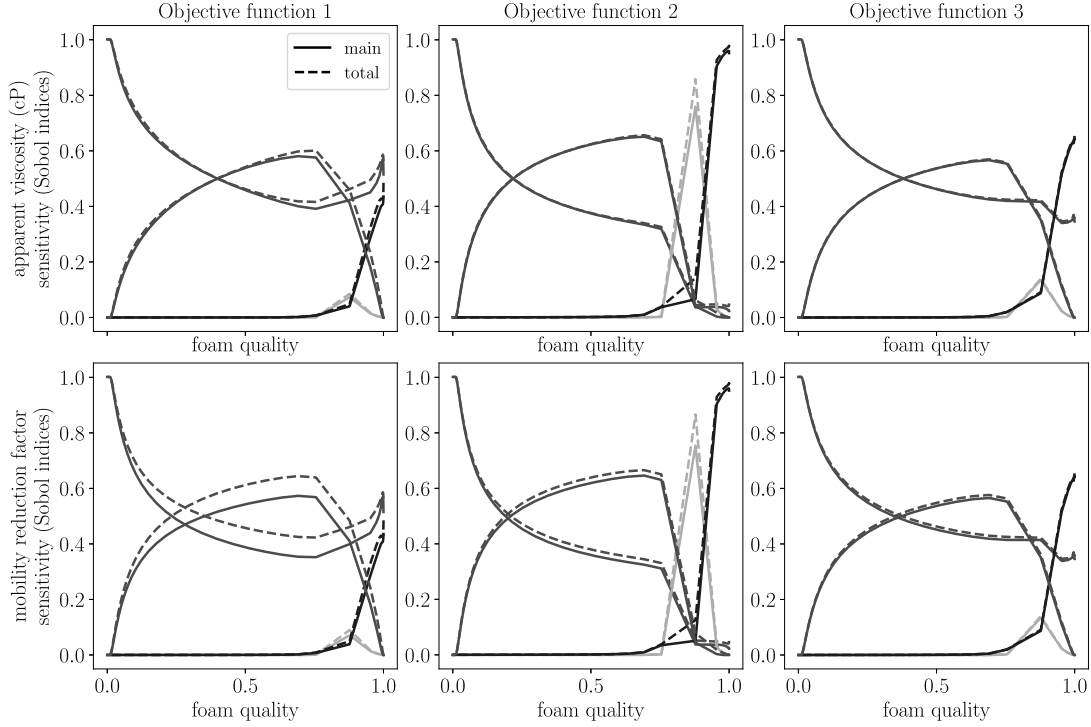


Figure 46 – Main and total Sobol sensitivity indices for the synthetic dataset #1. Red: $fmmob$, yellow: SF , blue: $sfbet$, and green: $epcap$.

objective function that can be used to perform model calibration employing nonlinear least square methods and Bayesian inference methods. The proposed objective function includes experimental data for mobility reduction factor and the traditional data for apparent viscosity. Nevertheless, it is important to highlight that there was no need for new experiments to obtain the experimental values of MRF.

Identifiability analysis showed that key parameters of the models are practically non-identifiable when using the traditional objective function that relies only on the experimental data for apparent viscosity. This is solved by adding the MRF experimental data to the objective function. The inverse UQ analysis revealed a similar trend. The probability density functions estimated for the parameters were more compact, i.e., with lower uncertainty when using the new objective function than when using only apparent viscosity. Finally, the forward UQ revealed how the experimental data of apparent viscosity and MRF complement each other. In summary, the new objective function generated the best calibrations with high fidelity and the lowest uncertainty.

The proposed approach for parameter estimation of the STARS foam flow model was explored for the particular case of dry-out and shear-thinning behavior in the MRF function. However, this approach can be useful for extended versions of the STARS model, which include parameters for taking into account the other effects (*e.g.* surfactant concentration and oil saturation) into foam mobility.

7 Conclusions

In this thesis, different aspects of multiphase flow in a porous medium were studied and analyzed under the perspective of inverse and forward UQ and SA. The contributions of this work were divided in three parts.

In particular, in a first study, we have considered the two-phase flow described by the Buckley–Leverett equation and considered two different relative permeability models for the UQ and SA studies. In the second study the co-injection of foam into the water–gas flow taking into account experimental data was approached. Two different modeling foam flow dynamics were adopted and compared: semi-empirical and population balance models. Moreover, the third study explored the consequences of performing the adjustment of foam models using different objective functions. The results of this last problem reflected on the reliability of the foam model forward evaluations.

In the first work presented, relative permeability data for water and oil from the literature were used to adjust the relative permeability models. The posterior distributions of parameters were determined by the MCMC method. The distributions were used as uncertain input parameters for the two-phase flow in a porous medium. The results showed strong correlations between LET parameters for both datasets, whereas less significant correlations were observed for Chierici’s model. Sensitivity analysis highlighted that the highest sensitivity index parameter varied, depending on the QoI and wettability. Besides, the SA revealed high interactions between all the two permeability model parameters’ for the output associated with oil production. These observations in terms of uncertainty and sensitivity of the parameters will be helpful for further studies regarding the calibration of the models and guiding new experiments. The method presented in this work requires no changes to the computer model. It is computationally efficient because fewer model evaluations are required to achieve convergence compared to the classic Monte Carlo method. Thus, the proposed method for performing UQ and SA analyses seems an attractive alternative for field-scale problems, where the computational cost of one model evaluation is typically very high.

In the second part of this work, we have investigated the propagation of uncertainties from experimental data to computational models of foam flow in porous media. Two established foam flood models were considered under local equilibrium conditions concerning foam creation and destruction. A core-flood experiment based on a foam quality scan was performed and used to characterize these models’ parameters using a Bayesian estimation technique. Monte Carlo evaluations were then used to perform a sensitivity analysis and propagate uncertainties from input parameters to quantities of interest.

The sensitivity analysis revealed that the model’s parameters play different roles and

depend on the quantity of interest, the foam–quality regime, and limiting water saturation. It was shown that $fmmob$ for STARS and its equivalent parameter in the Linear Kinetic model are highly relevant in the low–quality regime. In contrast, in the high–quality regime, the SF parameter from the STARS model (and the corresponding parameter in the LK model) is the most relevant for apparent viscosity. For quantities related to mobility (such as MRF and λ_{rt}), the roles of these two parameters change concerning water saturation: for low values of water saturation, SF is the crucial parameter, whereas, for higher values, the $fmmob$ parameter appears with a higher impact on these quantities. Higher uncertainties were observed in the high–quality regime for apparent viscosity and pressure drop than in the low–quality regime. By artificially augmenting the data set with synthetic data at the high–quality regime, it was possible to reduce the uncertainties significantly. Together, these results show the importance of the framework presented here, which combines mathematical models, inverse and forward uncertainty quantification, and sensitivity analysis. Based on these tools, we can suggest new experiments to further contribute to the understanding of this complex phenomenon.

In the third part, we explored how the CMG–STARS model’s reliability is affected by different objective functions used to calibrate foam models. Techniques from Bayesian inference, deterministic model calibration, forward uncertainty quantification, and variance–based sensitivity analysis were used to compare and evaluate the responses of the same foam model using different experimental observations. The traditional objective function to adjust foam models was compared against two new potential objective functions. In particular, after executing the MCMC and evaluating the profile likelihood of each model parameter, we observed that the results obtained employing the traditional objective function overestimate the uncertainty and may suffer from unidentifiability, turning the model evaluations less reliable. In contrast, using the objective function that combines the experimental measurements of apparent viscosity (traditional) with experimental records of mobility reduction factor, the posterior density distributions are more constrained, retrieving a better identification of parameters, resulting in more reliable model evaluations. The results and conclusions of this study case are of utmost relevance for the successful application of foam–assisted EOR models in projects.

The approach presented in this work, which is based on Bayesian estimation, uncertainty propagation, and sensitivity analysis, holds great potential to advance the physical modeling and calibration of foam flow models in porous media. When applied to more complex models of foam flow, it can help assess the model’s reliability and identify parameters that most affect the predictions. This could be used to guide the calibration and tuning of the foam flow model used. Therefore, it could be viewed as a possible way to improve foam application in EOR processes based on reservoir simulators.

7.1 Academic contributions

During the development of the present work, different academic contributions were published in specialized journals and presented in scientific conferences.

Articles in peer reviewed journal:

- Valdez, A. R., Rocha, B. M., Chapiro, G., & dos Santos, R. W. (2020). Uncertainty quantification and sensitivity analysis for relative permeability models of two-phase flow in porous media. *Journal of Petroleum Science and Engineering*, 107297, doi:10.1016/j.petrol.2020.107297.
- Valdez, A. R., Rocha, B. M., Gramatges A., Façanha J. M., de Souza A, Chapiro, G., & dos Santos, R. W. (2021) Foam assisted water-gas flow parameters: from core-flood experiment to uncertainty quantification and sensitivity analysis. *Transport in Porous Media*. doi:10.1007/s11242-021-01550-0.

Articles in preparation to be submitted to peer reviewed journal:

- Valdez, A. R., Rocha, B. M., Chapiro, G., & dos Santos, R. W. (2021). Assessing uncertainties and identifiability of foam displacement models employing different objective functions for parameter estimation.

Complete articles published in conference proceedings:

- Valdez, A., dos Santos, R. W., Chapiro, G., & Rocha, B. M. (2020). Um estudo de quantificação de incertezas e análise de sensibilidade de funções de fluxo fracionário da equação de Buckley-Leverett. *Proceeding Series of the Brazilian Society of Computational and Applied Mathematics*, 7(1).

Abstracts published in conference proceedings:

- Valdez, A., dos Santos, R. W., Chapiro, G., & Rocha, B. M. (2020). A study of uncertainty quantification and sensitivity analysis of a relative permeability model used to simulate two-phase flow in porous media. *3rd BR-InterPore Conference on Porous Media*, Petrópolis, RJ, Aug 2019
- dos Santos, R. W., Valdez, A., Rocha, B. M. & Chapiro, G., (2020) Uncertainty quantification in a model for foam flooding in porous media. *12th Annual meeting InterPore* (online), August, 2020.
- Valdez, A., Rocha, B. M., Chapiro, G. & dos Santos, R. W. (2021) Rheological response of foam flooding models considering experimental uncertainties. *13th Annual meeting InterPore* (online), June, 2021.

7.2 Future steps

The simplified STARS foam model considered in this work uses MRF depending only on the water saturation ($F2$ or F_{water}) and shear–thinning ($F5$ or F_{shear}) functions. The identifiability and inverse UQ analysis performed for the CMG–STARS foam model could be extended to consider the functions describing other effect such as surfactant concentration and oil saturation.

Another limitation is that we only studied uncertainties from the STARS and LK foam models' parameters. Other parameters, such as those from the relative permeability (Corey) model, connate water saturation, residual gas saturations, end–point saturation, porosity, and others, could be included in a complete recovery analysis using UQ and SA. Other models, such as LET and Chierici, can be used to describe relative permeability data following similar procedures.

One natural extension of this work would be to consider the dynamics of creation and coalescence of foam bubbles, by taking into account other models such as, the Zitha & Du [149] model, the Kam & Rossen [76, 75] model, as well as the transient part of the Linear Kinetic [5] model studied in this work. The modeling of foam dynamics in porous media remains until our days as a cumbersome and challenging problem without a generalized methodology to solve the problem. The conclusions obtained from this thesis represent possible alternatives to draw general patterns among the different foam models.

Bibliography

- 1 Abdul, H., Muggeridge, A.: Fingering regimes in unstable miscible displacements. *Physics of Fluids* **32**(1), 016,601 (2020). DOI <https://doi.org/10.1063/1.5128338>
- 2 Albrecht, R., Marsden, S.: Foams as blocking agents in porous media. *Society of Petroleum Engineers Journal* **10**(01), 51–55 (1970)
- 3 Alvarez, J., Rivas, H., Rossen, W.: Unified model for steady-state foam behavior at high and low foam qualities. *SPE journal* **6**(03), 325–333 (2001)
- 4 Aronson, A., Bergeron, V., Fagan, M., Radke, C.: The influence of disjoining pressure on foam stability and flow in porous media. *Colloids and Surfaces A: Physicochemical and Engineering Aspects* **83**(2), 109–120 (1994). DOI [https://doi.org/10.1016/0927-7757\(94\)80094-4](https://doi.org/10.1016/0927-7757(94)80094-4)
- 5 Ashoori, E., Marchesin, D., Rossen, W.: Roles of transient and local equilibrium foam behavior in porous media: Traveling wave. *Colloids and Surfaces A: Physicochemical and Engineering Aspects* **377**(1), 228 – 242 (2011). DOI <https://doi.org/10.1016/j.colsurfa.2010.12.042>
- 6 Babadagli, T.: Philosophy of EOR. *Journal of Petroleum Science and Engineering* **188** (2020). DOI <https://doi.org/10.1016/j.petrol.2020.106930>
- 7 Bear, J.: *Modeling Phenomena of Flow and Transport in Porous Media. Theory and applications of transport in porous media.* Springer International Publishing (2018). DOI [10.1007/978-3-319-72826-1](https://doi.org/10.1007/978-3-319-72826-1)
- 8 Berg, S., Unsal, E., Dijk, H.: Non-uniqueness and uncertainty quantification of relative permeability measurements by inverse modelling. *Computers and Geotechnics* **132**, 103,964 (2020). DOI <https://doi.org/10.1016/j.compgeo.2020.103964>
- 9 Berg, S., Unsal, E., Dijk, H.: Sensitivity and uncertainty analysis for parameterization of multiphase flow models. *Transport in Porous Media* pp. 1–31 (2021). DOI <https://doi.org/10.1007/s11242-021-01576-4>
- 10 Bergeron, V., Radke, C.: Disjoining pressure and stratification in asymmetric thin-liquid films. *Colloid and Polymer Science* **273**(2), 165–174 (1995). DOI <https://doi.org/10.1007/BF00654014>
- 11 Blunt, M.: *Multiphase flow in permeable media: A pore-scale perspective.* Cambridge University Press (2017)
- 12 Boeije, C., Rossen, W.: Fitting foam simulation model parameters to data. In: *IOR 2013-17th European Symposium on Improved Oil Recovery*, pp. cp–342. European Association of Geoscientists & Engineers (2013)
- 13 Boeije, C.S., Rossen, W.: Fitting foam-simulation-model parameters to data: I. coinjection of gas and liquid. *SPE Reservoir Evaluation & Engineering* **18**(02), 264–272 (2015)

- 14 Boukadi, F., Bemani, A., Babadagli, T.: Investigating uncertainties in relative permeability measurements. *Energy Sources* **27**(8), 719–728 (2005). DOI 10.1080/00908310490450638
- 15 Bouquet, S., Douarche, F., Roggero, F., Bourbiaux, B.: Foam processes in naturally fractured carbonate oil-wet reservoirs: technical and economic analysis and optimization. *Journal of Petroleum Science and Engineering* **190**, 107,111 (2020). DOI <https://doi.org/10.1016/j.petrol.2020.107111>
- 16 Brooks, R.H., Corey, A.T.: Hydraulic properties of porous media. Hydrology papers no. 3. Fort Collins, Colorado : Colorado State University (1964)
- 17 Brooks, S.: Markov chain Monte Carlo method and its application. *Journal of the royal statistical society: series D (the Statistician)* **47**(1), 69–100 (1998)
- 18 Brooks, S., Gelman, A., Jones, G., Meng, X.: Handbook of Markov chain monte carlo. CRC press (2011)
- 19 Buckley, S., Leverett, M.: Mechanism of fluid displacement in sands. *Transactions of the AIME* **146** (1942). DOI 10.2118/942107-G
- 20 Burdine, N., et al.: Relative permeability calculations from pore size distribution data. *Journal of Petroleum Technology* **5**(03), 71–78 (1953)
- 21 Camacho, A., Talavera, A., Emerick, A., Pacheco, M., Zannia, J.: Uncertainty quantification in reservoir simulation models with polynomial chaos expansions: Smolyak quadrature and regression method approach. *Journal of Petroleum Science and Engineering* **153**, 203–211 (2017). DOI 10.1016/j.petrol.2017.03.046
- 22 Castillo, R.S., Haar, S.T., Ponnens, C., Bos, M., Rossen, W.: Fractional-flow theory for non-newtonian surfactant-alternating-gas foam processes. *Transport in Porous Media* **131**(2), 399–426 (2020). DOI <https://doi.org/10.1007/s11242-019-01351-6>
- 23 Chen, Q., Gerritsen, M., Kovscek, A.: Modeling foam displacement with the local-equilibrium approximation: theory and experimental verification. *SPE Journal* **15**(01), 171–183 (2010)
- 24 Cheng, L., Reme, A., Shan, D., Coombe, D., Rossen, W., et al.: Simulating foam processes at high and low foam qualities. In: SPE/DOE improved oil recovery symposium. Society of Petroleum Engineers (2000)
- 25 Chierici, G.L.: Novel relations for drainage and imbibition relative permeabilities (SPE-10165-PA). *Society of Petroleum Engineers Journal* **24** (1984). DOI 10.2118/10165-PA
- 26 Chierici, G.L.: Principles of petroleum reservoir engineering. Volume 1. Springer-Verlag Berlin Heidelberg (1994). DOI 10.1007/978-3-662-02964-0
- 27 Childs, E.C., Collis-George, N.: The permeability of porous materials. *Proceedings of the Royal Society of London. Series A. Mathematical and Physical Sciences* **201**(1066), 392–405 (1950)

- 28 Chorin, A.: The instability of fronts in a porous medium. *Communications in mathematical physics* **91**(1), 103–116 (1983). DOI <https://doi.org/10.1007/BF01206054>
- 29 Ciriello, V., Federico, V.D.: Similarity solutions for flow of non-newtonian fluids in porous media revisited under parameter uncertainty. *Advances in Water Resources* **43**, 38–51 (2012). DOI <https://doi.org/10.1016/j.advwatres.2012.03.028>
- 30 Ciriello, V., Federico, V.D., Riva, M., Cadini, F., Sanctis, J.D., Zio, E., Guadagnini, A.: Polynomial chaos expansion for global sensitivity analysis applied to a model of radionuclide migration in a randomly heterogeneous aquifer. *Stochastic Environmental Research and Risk Assessment* **27**(4), 945–954 (2013). DOI <https://doi.org/10.1007/s00477-012-0616-7>
- 31 CMG: CMG–STARS users manual; version 2019.10 (2019)
- 32 Corey, A.T.: The interrelation between gas and oil relative permeabilities. *Producers Monthly* **19**(1), 38–41 (1954)
- 33 Darcy, H.: *Les Fontaines publiques de la ville de Dijon. Exposition et application des principes à suivre et des formules à employer dans les questions de distribution d’eau, etc.* V. Dalamont (1856)
- 34 de Paula, F.F., Quinelato, T., Igreja, I., Chapiro, G.: A numerical algorithm to solve the two-phase flow in porous media including foam displacement. In: *Computational Science – ICCS 2020*. Springer International Publishing (2020). DOI https://doi.org/10.1007/978-3-030-50436-6_2
- 35 Debusschere, B., Najm, H., Pébay, P., Knio, O., Ghanem, R., tre, O.L.M.: Numerical challenges in the use of polynomial chaos representations for stochastic processes. *SIAM journal on scientific computing* **26**(2), 698–719 (2004). DOI [10.1137/S1064827503427741](https://doi.org/10.1137/S1064827503427741)
- 36 Douarche, F., Veiga, S.D., Feraille, M., Enchéry, G., Touzani, S., Barsalou, R.: Sensitivity analysis and optimization of surfactant-polymer flooding under uncertainties. *Oil & Gas Science and Technology–Revue d’IFP Energies nouvelles* **69**(4), 603–617 (2014). DOI [10.2516/ogst/2013166](https://doi.org/10.2516/ogst/2013166)
- 37 Ebeltoft, E., Lomeland, F.: Versatile three-phase correlations for relative permeability and capillary pressure. In: *International Symposium of the Society of Core Analysts held in Napa Valley, California, USA*. SCA, vol. 34, pp. 1–14 (2013)
- 38 Ebeltoft, E., Lomeland, F., Brautaset, A., Haugen, A.: Parameter based scal-analysing relative permeability for full field application. In: *International Symposium of the Society of Core Analysis, Avignon, France*, pp. 8–11 (2014)
- 39 Eck, V.G., Donders, W.P., Sturdy, J., Feinberg, J., Delhaas, T., Hellevik, L.R., Huberts, W.: A guide to uncertainty quantification and sensitivity analysis for cardiovascular applications. *International Journal for Numerical Methods in Biomedical Engineering* **32**(8) (2015). DOI [10.1002/cnm.2755](https://doi.org/10.1002/cnm.2755)
- 40 Eftekhari, A., Farajzadeh, R.: Effect of foam on liquid phase mobility in porous media. *Scientific reports* **7**(1), 1–8 (2017). DOI <https://doi.org/10.1038/srep43870>

- 41 Falls, A., Hirasaki, G., Patzek, T., Gauglitz, D., Miller, D., Ratulowski, T.: Development of a mechanistic foam simulator: the population balance and generation by snap-off. *SPE reservoir engineering* **3**(03), 884–892 (1988)
- 42 Falls, A., Musters, J., Ratulowski, J.: The apparent viscosity of foams in homogeneous bead packs. *SPE Reservoir Engineering* **4**(02), 155–164 (1989)
- 43 Farajzadeh, R., Andrianov, A., Krastev, R., Hirasaki, G., Rossen, W.: Foam–oil interaction in porous media: implications for foam assisted enhanced oil recovery. *Advances in colloid and interface science* **183**, 1–13 (2012). DOI <https://doi.org/10.1016/j.cis.2012.07.002>
- 44 Farajzadeh, R., Eftekhari, A., Hajibeygi, H., Kahrobaei, S., der Meer, J.V., Vincent-Bonnieu, S., Rossen, W.: Simulation of instabilities and fingering in surfactant alternating gas (SAG) foam enhanced oil recovery. *Journal of Natural Gas Science and Engineering* **34**, 1191–1204 (2016). DOI <https://doi.org/10.1016/j.jngse.2016.08.008>
- 45 Farajzadeh, R., Lotfollahi, M., Eftekhari, A., Rossen, W., Hirasaki, G.: Effect of permeability on implicit-texture foam model parameters and the limiting capillary pressure. *Energy & fuels* **29**(5), 3011–3018 (2015). DOI <https://doi.org/10.1021/acs.energyfuels.5b00248>
- 46 Feinberg, J., Eck, V., Langtangen, H.: Multivariate polynomial chaos expansions with dependent variables. *SIAM Journal on Scientific Computing* **40**(1), A199–A223 (2018). DOI [10.1137/15M1020447](https://doi.org/10.1137/15M1020447)
- 47 Feinberg, J., Langtangen, H.P.: Chaospy: An open source tool for designing methods of uncertainty quantification. *Journal of Computational Science* **11**, 46–57 (2015). DOI [10.1016/j.jocs.2015.08.008](https://doi.org/10.1016/j.jocs.2015.08.008)
- 48 Filho, J.C., Delshad, M., Sepehrnoori, K.: Estimation of foam-flow parameters for local equilibrium methods by use of steady-state flow experiments and optimization algorithms. *SPE Reservoir Evaluation & Engineering* **21**(01), 160–173 (2018)
- 49 Foreman-Mackey, D., Hogg, D.W., Lang, D., Goodman, J.: emcee: The mcmc hammer. *pasp* **125**, 306 (2013). DOI [10.1086/670067](https://doi.org/10.1086/670067)
- 50 Gardner, W.: Some steady-state solutions of the unsaturated moisture flow equation with application to evaporation from a water table. *Soil science* **85**(4), 228–232 (1958)
- 51 Gassara, O., Douarche, F., Braconnier, B., Bourbiaux, B.: Equivalence between semi-empirical and population-balance foam models. *Transport in Porous Media* **120**(3), 473–493 (2017). DOI <https://doi.org/10.1007/s11242-017-0935-8>
- 52 Gassara, O., Douarche, F., Braconnier, B., Bourbiaux, B.: Calibrating and scaling semi-empirical foam flow models for the assessment of foam-based EOR processes (in heterogeneous reservoirs). *Transport in Porous Media* **131**(1), 193–221 (2020). DOI <https://doi.org/10.1007/s11242-018-01223-5>
- 53 Ghanem, R., Higdon, D., Owhadi, H.: Handbook of uncertainty quantification, vol. 6. Springer (2017). DOI <https://doi.org/10.1007/978-3-319-12385-1>

- 54 Goodman, J., Weare, J.: Ensemble samplers with affine invariance. *Communications in Applied Mathematics and Computational Science* **5**(1), 65–80 (2010)
- 55 Gratiet, L.L., Marelli, S., Sudret, B.: Metamodel-based sensitivity analysis: polynomial chaos expansions and gaussian processes. *Handbook of Uncertainty Quantification* pp. 1–37 (2016). DOI https://doi.org/10.1007/978-3-319-12385-1_38
- 56 Green, D., Willhite, G.: Enhanced oil recovery, vol. 6. Henry L. Doherty Memorial Fund of AIME, Society of Petroleum Engineers (1998)
- 57 Hanssen, J.: Foam as a gas-blocking agent in petroleum reservoirs I: Empirical observations and parametric study. *Journal of Petroleum Science and Engineering* **10**(2), 117–133 (1993). DOI [https://doi.org/10.1016/0920-4105\(93\)90036-E](https://doi.org/10.1016/0920-4105(93)90036-E)
- 58 Hanssen, J.: Foam as a gas-blocking agent in petroleum reservoirs ii: Mechanisms of gas blockage by foam. *Journal of Petroleum Science and Engineering* **10**(2), 135–156 (1993). DOI [https://doi.org/10.1016/0920-4105\(93\)90037-F](https://doi.org/10.1016/0920-4105(93)90037-F)
- 59 He, L., Huang, G., Lu, H., Wang, S., Xu, Y.: Quasi-monte carlo based global uncertainty and sensitivity analysis in modeling free product migration and recovery from petroleum-contaminated aquifers. *Journal of hazardous materials* **219**, 133–140 (2012). DOI <https://doi.org/10.1016/j.jhazmat.2012.03.067>
- 60 Heller, J.: Co2 foams in enhanced oil recovery. In: *Foams: Fundamentals and Applications in the Petroleum Industry*. ACS Publications (1994)
- 61 Heller, J., Kuntamukkula, M.: Critical review of the foam rheology literature. *Industrial & engineering chemistry research* **26**(2), 318–325 (1987)
- 62 Hematpur, H., Mahmood, S., Nasr, N., Elraies, K.: Foam flow in porous media: Concepts, models and challenges. *Journal of Natural Gas Science and Engineering* **53**, 163–180 (2018). DOI <https://doi.org/10.1016/j.jngse.2018.02.017>
- 63 Herman, J., Usher, W.: Salib: An open-source python library for sensitivity analysis. *Journal of Open Source Software* **2**(9), 97 (2017). DOI [10.21105/joss.00097](https://doi.org/10.21105/joss.00097)
- 64 Hirasaki, G., Lawson, J.: Mechanisms of foam flow in porous media: apparent viscosity in smooth capillaries. *Society of Petroleum Engineers Journal* **25**(02), 176–190 (1985)
- 65 Hirasaki, G., Miller, C., Szafranski, R., Tanzil, D., Lawson, J., Meinardus, H., Londergan, J., Jackson, R., Pope, G., Wade, W.: Field demonstration of the surfactant/foam process for aquifer remediation. In: *SPE Annual Technical Conference and Exhibition*. Society of Petroleum Engineers (1997)
- 66 Hogg, D., Foreman-Mackey, D.: Data analysis recipes: Using markov chain monte carlo. *The Astrophysical Journal Supplement Series* **236**(1), 11 (2018). DOI <https://doi.org/10.3847/1538-4365/aab76e>
- 67 Honarpour, M., Koederitz, F., Herbert, A.: Relative permeability of petroleum reservoirs. CRC Press (2018)

- 68 Hosder, S., Walters, R., M. Balch, M.: Efficient sampling for non-intrusive polynomial chaos applications with multiple uncertain input variables. In: 48th AIAA/ASME/ASCE/AHS/ASC Structures, Structural Dynamics, and Materials Conference, p. 1939 (2007)
- 69 Irmay, S.: On the hydraulic conductivity of unsaturated soils. *Eos, Transactions American Geophysical Union* **35**(3), 463–467 (1954)
- 70 Jha, B., Cueto-Felgueroso, L., Juanes, R.: Fluid mixing from viscous fingering. *Physical review letters* **106**(19), 194,502 (2011). DOI <https://doi.org/10.1103/PhysRevLett.106.194502>
- 71 Johnson, E., Bossler, D., Bossler, V.: Calculation of relative permeability from displacement experiments (SPE-1023-G) (1959)
- 72 Jones, S., Laskaris, G., Vincent-Bonnieu, S., Farajzadeh, R., Rossen, W.: Effect of surfactant concentration on foam: From coreflood experiments to implicit-texture foam-model parameters. *Journal of Industrial and Engineering Chemistry* **37**, 268–276 (2016)
- 73 Kahrobaei, S., Farajzadeh, R.: Insights into effects of surfactant concentration on foam behavior in porous media. In: IOR 2019–20th European Symposium on Improved Oil Recovery, vol. 2019, pp. 1–13. European Association of Geoscientists & Engineers (2019)
- 74 Kam, S.: Improved mechanistic foam simulation with foam catastrophe theory. *Colloids and Surfaces A: Physicochemical and Engineering Aspects* **318**(1-3), 62–77 (2008). DOI <https://doi.org/10.1016/j.colsurfa.2007.12.017>
- 75 Kam, S., Nguyen, Q., Li, Q., Rossen, W.: Dynamic simulations with an improved model for foam generation. *SPE Journal* **12**(01), 35–48 (2007)
- 76 Kam, S., Rossen, W.: A model for foam generation in homogeneous media. *SPE Journal* **8**(04), 417–425 (2003)
- 77 Kao, Y., Eisenberg, M.: Practical unidentifiability of a simple vector-borne disease model: Implications for parameter estimation and intervention assessment. *Epidemics* **25**, 89–100 (2018). DOI <https://doi.org/10.1016/j.epidem.2018.05.010>
- 78 Kapetas, L., Bonnieu, S., Danelis, S., Rossen, W., Farajzadeh, R., Eftekhari, A., Shafian, S.M., Bahrim, R.K.: Effect of temperature on foam flow in porous media. *Journal of Industrial and Engineering Chemistry* **36**, 229–237 (2016). DOI <https://doi.org/10.1016/j.jiec.2016.02.001>
- 79 Kapetas, L., Bonnieu, S., Farajzadeh, R., Eftekhari, A., Shafian, S.M., Bahrim, R.K., Rossen, W.: Effect of permeability on foam-model parameters: An integrated approach from core-flood experiments through to foam diversion calculations. *Colloids and Surfaces A: Physicochemical and Engineering Aspects* **530**, 172–180 (2017). DOI <https://doi.org/10.1016/j.colsurfa.2017.06.060>
- 80 Kapetas, L., van El, W., Rossen, W.: Representing slow foam dynamics in laboratory corefloods for foam enhanced oil recovery. In: SPE Improved Oil Recovery Symposium. Society of Petroleum Engineers (2014)

- 81 Katiyar, A., Patil, P., Rohilla, N., Rozowski, P., Evans, J., Bozeman, T., Nguyen, Q.: Industry-first hydrocarbon-foam eor pilot in an unconventional reservoir: design, implementation, and performance analysis. In: Unconventional Resources Technology Conference, Denver, Colorado, 22-24 July 2019, pp. 233–255. Unconventional Resources Technology Conference (URTeC), SPE (2019)
- 82 Khatib, Z., Hirasaki, G., Falls, A.: Effects of capillary pressure on coalescence and phase mobilities in foams flowing through porous media. *SPE reservoir engineering* **3**(03), 919–926 (1988)
- 83 Kovscek, A.R., Patzek, T.W., Radke, C.J.: A mechanistic population balance model for transient and steady-state foam flow in boise sandstone. *Chemical Engineering Science* **50**(23), 3783–3799 (1995)
- 84 Lake, L., Johns, R., Rossen, W., Pope, G.: *Fundamentals of enhanced oil recovery*. Society of Petroleum Engineers Richardson, TX (2014)
- 85 Langtangen, H., Tveito, A.A., Winther, R.: Instability of buckley-leverett flow in a heterogeneous medium. *Transport in Porous Media* **9**(3), 165–185 (1992). DOI <https://doi.org/10.1007/BF00611965>
- 86 Lee, H., Heller, J., Hoefer, A.: Change in apparent viscosity of co2 foam with rock permeability. *SPE reservoir engineering* **6**(04), 421–428 (1991)
- 87 Leverett, M.: Capillary behavior in porous solids. *Transactions of the AIME* **142**(01), 152–169 (1941)
- 88 Leverett, M., Lewis, W.: Steady flow of gas-oil-water mixtures through unconsolidated sands. *Transactions of the AIME* **142**(01), 107–116 (1941)
- 89 Leverett, M., et al.: Flow of oil-water mixtures through unconsolidated sands. *Transactions of the AIME* **132**(01), 149–171 (1939)
- 90 Lomeland, F.: LET correlations for relative permeability and capillary pressure. <https://frode54.wordpress.com/table-generators/> (2019). [Online; accessed September 2019]
- 91 Lomeland, F., Ebeltoft, E., Hasanov, B.: A versatile representation of upscaled relative permeability for field applications (SPE-154487-MS). In: 74th EAGE Conference and Exhibition incorporating EUROPEC 2012 (2012)
- 92 Lomeland, F., Ebeltoft, E., Thomas, W.H.: A new versatile relative permeability correlation. In: *Proceedings of the International Symposium of the Society of Core Analysts*, (2005) (2005). SCA2005-32
- 93 Lomeland, F., Ebeltoft, E., Thomas, W.H.: A new versatile capillary pressure correlation. In: Paper SCA 2008-08 presented at the International Symposium of the Society of Core Analysts held in Abu Dhabi, UAE, vol. 29 (2008)
- 94 Lomeland, F., Orec, A.S.: Overview of the LET family of versatile correlations for flow functions. In: *International Symposium of the Society of Core Analysts held at Trondheim, Norway* (2018)

- 95 Lotfollahi, M., Farajzadeh, R., Delshad, M., Varavei, A., Rossen, W.: Comparison of implicit-texture and population-balance foam models. *Journal of Natural Gas Science and Engineering* **31**, 184–197 (2016).
DOI <http://dx.doi.org/10.1016/j.jngse.2016.03.018>
- 96 Ma, K., Farajzadeh, R., Lopez-Salinas, J., Miller, C., Biswal, S., Hirasaki, G.: Estimation of parameters for the simulation of foam flow through porous media: Part 3; non-uniqueness, numerical artifact and sensitivity. In: SPE enhanced oil recovery conference. Society of Petroleum Engineers (2013)
- 97 Ma, K., Farajzadeh, R., Lopez-Salinas, J., Miller, C., Biswal, S., Hirasaki, G.: Non-uniqueness, numerical artifacts, and parameter sensitivity in simulating steady-state and transient foam flow through porous media. *Transport in porous media* **102**(3), 325–348 (2014). DOI <https://doi.org/10.1007/s11242-014-0276-9>
- 98 Ma, K., Lopez-Salinas, J., Puerto, M., Miller, C., Biswal, S., Hirasaki, G.: Estimation of parameters for the simulation of foam flow through porous media. part 1: the dry-out effect. *Energy & fuels* **27**(5), 2363–2375 (2013).
DOI <https://doi.org/10.1021/ef302036s>
- 99 Marle, C.: *Multiphase flow in porous media*. Éditions Technip (1981)
- 100 McClarren, R.: *Uncertainty Quantification and Predictive Computational Science*. Springer (2018). DOI <https://doi.org/10.1007/978-3-319-99525-0>
- 101 Moghadasi, L., Guadagnini, A., Inzoli, F., Bartosek, M.: Interpretation of two-phase relative permeability curves through multiple formulations and model quality criteria. *Journal of Petroleum Science and Engineering* **135**, 738 – 749 (2015).
DOI <https://doi.org/10.1016/j.petrol.2015.10.027>
- 102 Mohamed, I., Nasr-El-Din, H.: Formation damage due to co2 sequestration in deep saline carbonate aquifers. In: SPE International Symposium and Exhibition on Formation Damage Control. Society of Petroleum Engineers (2012)
- 103 Mollaei, A., Lake, L., Delshad, M.: Application and variance based sensitivity analysis of surfactant–polymer flooding using modified chemical flood predictive model. *Journal of Petroleum Science and Engineering* **79**(1-2), 25–36 (2011).
DOI <https://doi.org/10.1016/j.petrol.2011.07.016>
- 104 Moradi-Araghi, A., Johnston, E., Zornes, D., Harpole, K.: Laboratory evaluation of surfactants for co2-foam applications at the south cowden unit. In: International Symposium on Oilfield Chemistry. Society of Petroleum Engineers (1997)
- 105 Muskat, M., Meres, M.: The flow of heterogeneous fluids through porous media. *Physics* **7**(9), 346–363 (1936)
- 106 Nagel, J., Sudret, B.: Spectral likelihood expansions for bayesian inference. *Journal of Computational Physics* **309**, 267–294 (2016).
DOI <https://doi.org/10.1016/j.jcp.2015.12.047>
- 107 Newville, M., Otten, R., Nelson, A., Ingargiola, A., Stensitzki, T., Allan, D., Fox, A., Carter, F., Michał, Pustakhod, D., Glenn, Ram, Y., MerlinSmiles, Deil, C., Stuermer, Beelen, A., Frost, O., gasquev, Hansen, A.L.R., Stark, A., Spillane, T., Caldwell, S.,

- Pollreno, A., andrewhannum, Borreguero, J., Fraine, J., deep 42-thought, Maier, B.F., Gamari, B., Almarza, A.: *lmfit/lmfit-py* 0.9.13 (2019). DOI [10.5281/zenodo.2620617](https://doi.org/10.5281/zenodo.2620617)
- 108 Olajire, A.: Review of ASP EOR (alkaline surfactant polymer enhanced oil recovery) technology in the petroleum industry: Prospects and challenges. *Energy* **77**, 963–982 (2014). DOI <https://doi.org/10.1016/j.energy.2014.09.005>
- 109 Osterloh, W., Jr, M.J.: Effects of gas and liquid velocity on steady-state foam flow at high temperature. In: *SPE/DOE Enhanced Oil Recovery Symposium*. Society of Petroleum Engineers (1992)
- 110 National Agency of Petroleum, N.G., ANP, B.: *Anp-activities report*. <http://www.anp.gov.br/exploracao-e-producao-de-oleo-e-gas/previsao-de-producao-e-atividades> (2020). [Online; accessed September 2020]
- 111 National Agency of Petroleum, N.G., ANP, B.: *Oil and gas production dynamic panel*. <http://www.anp.gov.br/exploracao-e-producao-de-oleo-e-gas/painel-dinamicos-de-producao-de-petroleo-e-gas-natural> (2020). [Online; accessed September 2020]
- 112 Pettersson, P., Tchelepi, H.: Stochastic galerkin framework with locally reduced bases for nonlinear two-phase transport in heterogeneous formations. *Computer Methods in Applied Mechanics and Engineering* **310**, 367–387 (2016). DOI <https://doi.org/10.1016/j.cma.2016.07.013>
- 113 Portoís, C., Essouayed, E., Annable, M., Guiserix, N., Joubert, A., Atteia, O.: Field demonstration of foam injection to confine a chlorinated solvent source zone. *Journal of contaminant hydrology* **214**, 16–23 (2018). DOI <https://doi.org/10.1016/j.jconhyd.2018.04.003>
- 114 Rannala, B.: Identifiability of parameters in mcmc bayesian inference of phylogeny. *Systematic biology* **51**(5), 754–760 (2002). DOI <https://doi.org/10.1080/10635150290102429>
- 115 Raue, A., Kreutz, C., Maiwald, T., Bachmann, J., Schilling, M., Klingmüller, U., Timmer, J.: Structural and practical identifiability analysis of partially observed dynamical models by exploiting the profile likelihood. *Bioinformatics* **25**(15), 1923–1929 (2009). DOI <https://doi.org/10.1093/bioinformatics/btp358>
- 116 Raue, A., Kreutz, C., Theis, F., Timmer, J.: Joining forces of bayesian and frequentist methodology: a study for inference in the presence of non-identifiability. *Philosophical Transactions of the Royal Society A: Mathematical, Physical and Engineering Sciences* **371**(1984), 20110,544 (2013). DOI <https://doi.org/10.1098/rsta.2011.0544>
- 117 Renardy, M., Yi, T.M., Xiu, D., Chou, C.S.: Parameter uncertainty quantification using surrogate models applied to a spatial model of yeast mating polarization. *PLOS Computational Biology* **14**(5), 1–26 (2018). DOI [10.1371/journal.pcbi.1006181](https://doi.org/10.1371/journal.pcbi.1006181). URL <https://doi.org/10.1371/journal.pcbi.1006181>

- 118 Saffman, P., Taylor, G.: The penetration of a fluid into a porous medium or hele–shaw cell containing a more viscous liquid. *Proceedings of the Royal Society of London. Series A. Mathematical and Physical Sciences* **245**(1242), 312–329 (1958)
- 119 Saltelli, A., Annoni, P., Azzini, I., Campolongo, F., Ratto, M., Tarantola, S.: Variance based sensitivity analysis of model output. design and estimator for the total sensitivity index. *Computer Physics Communications* **181**(2), 259–270 (2010). DOI <https://doi.org/10.1016/j.cpc.2009.09.018>
- 120 Saltelli, A., Ratto, M., Andres, T., Campolongo, F., Cariboni, J., Gatelli, D., Saisana, M., Tarantola, S.: *Global sensitivity analysis. The primer*, vol. 304. John Wiley & Sons Ltd. (2008). DOI [10.1002/9780470725184](https://doi.org/10.1002/9780470725184)
- 121 Salvatier, J., Wiecki, T., Fonnesbeck, C.: Probabilistic programming in python using pymc3. *PeerJ Computer Science* **2**, e55 (2016). DOI [10.7717/peerj-cs.55](https://doi.org/10.7717/peerj-cs.55)
- 122 Saraiva, T., Szklo, A., PereiraLucena, A.F., Chavez-Rodriguez, M.: Forecasting brazil’s crude oil production using a multi-hubbert model variant. *Fuel* **115**, 24–31 (2014). DOI <https://doi.org/10.1016/j.fuel.2013.07.006>
- 123 Saye, R., Sethian, J.: Multiscale modelling of evolving foams. *Journal of Computational Physics* **315**, 273–301 (2016). DOI <https://doi.org/10.1016/j.jcp.2016.02.077>
- 124 Silpngarnlers, N., Guler, B., Ertekin, T., A.Grader: Development and testing of two-phase relative permeability predictors using artificial neural networks (SPE-69392-MS). In: *SPE Latin American and Caribbean Petroleum Engineering Conference* (2001). Society of Petroleum Engineers (2001). DOI <https://doi.org/10.2118/69392-MS>
- 125 da Silva Moreira, P.H., da Silveira, T.M.G., Drexler, S., Couto, P.: Application of MCMC optimization method to estimate relative permeability of carbonate rocks from unsteady-state core flood experiments (SPE-195562-MS). In: *SPE Europec featured at 81st EAGE Conference and Exhibition*. Society of Petroleum Engineers (2019). DOI <https://doi.org/10.2118/195562-MS>
- 126 Sobol, I.: Sensitivity estimates for nonlinear mathematical models. *Mathematical modelling and computational experiments* **1**(4), 407–414 (1993)
- 127 Sobol, I.: Global sensitivity indices for nonlinear mathematical models and their Monte Carlo estimates. *Mathematics and computers in simulation* **55**(1-3), 271–280 (2001). DOI [https://doi.org/10.1016/S0378-4754\(00\)00270-6](https://doi.org/10.1016/S0378-4754(00)00270-6)
- 128 Subbey, S., Monfared, H., Christie, M., Sambridge, M.: Quantifying uncertainty in flow functions derived from scal data. *Transport in porous media* **65**(2), 265–286 (2006). DOI <https://doi.org/10.1007/s11242-005-5998-2>
- 129 Sudret, B.: *Uncertainty propagation and sensitivity analysis in mechanical models—Contributions to structural reliability and stochastic spectral methods*, vol. 147. Habilitationa diriger des recherches, Université Blaise Pascal, Clermont-Ferrand, France (2007)

- 130 Sudret, B.: Global sensitivity analysis using polynomial chaos expansions. *Reliability engineering & system safety* **93**(7), 964–979 (2008). DOI <https://doi.org/10.1016/j.ress.2007.04.002>
- 131 Sudret, B.: Polynomial chaos expansions and stochastic finite element methods. In: *Risk and reliability in geotechnical engineering*, pp. 265–300. CRC Press (2014)
- 132 Tabeling, P., Zocchi, G., Libchaber, A.: An experimental study of the saffman-taylor instability. *Journal of Fluid Mechanics* **177**, 67–82 (1987)
- 133 Talebian, S., Masoudi, R., Tan, I., Zitha, P.: Foam assisted CO₂-EOR: A review of concept, challenges, and future prospects. *Journal of Petroleum Science and Engineering* **120**, 202–215 (2014). DOI <https://doi.org/10.1016/j.petrol.2014.05.013>
- 134 Tao, T., Watson, A.: Accuracy of JBN estimates of relative permeability: part 1-error analysis (SPE-11589-PA). *Society of Petroleum Engineers Journal* **24**(02), 209–214 (1984)
- 135 Tao, T., Watson, A.: Accuracy of JBN estimates of relative permeability: part 2-algorithms (SPE-12571-PA). *Society of Petroleum Engineers Journal* **24**(02), 215–223 (1984). DOI <https://doi.org/10.2118/12571-PA>
- 136 Tripathi, I., Mohanty, K.: Instability due to wettability alteration in displacements through porous media. *Chemical Engineering Science* **63**(21), 5366–5374 (2008). DOI <https://doi.org/10.1016/j.ces.2008.07.022>
- 137 Valdez, A., Rocha, B., Pérez-Gramatges, A., Façanha, J., de Souza, A., Chapiro, G., dos Santos, R.: Foam assisted water-gas flow parameters: from core-flood experiment to uncertainty quantification and sensitivity analysis. *Transport in Porous Media* (2021). DOI [10.1007/s11242-021-01550-0](https://doi.org/10.1007/s11242-021-01550-0)
- 138 Valdez, A.R., Rocha, B.M., Chapiro, G., dos Santos, R.W.: Uncertainty quantification and sensitivity analysis for relative permeability models of two-phase flow in porous media. *Journal of Petroleum Science and Engineering* (2020). DOI <https://doi.org/10.1016/j.petrol.2020.107297>
- 139 Welge, H.J.: A simplified method for computing oil recovery by gas or water drive. *Journal of Petroleum Technology* **4** (1952). DOI [10.2118/124-G](https://doi.org/10.2118/124-G)
- 140 Whitaker, S.: Flow in porous media i: A theoretical derivation of darcy’s law. *Transport in porous media* **1**(1), 3–25 (1986). DOI <https://doi.org/10.1007/BF01036523>
- 141 Woods, A.: *Flow in porous rocks*. Cambridge University Press (2015)
- 142 Wyckoff, R., Botset, H.: The flow of gas-liquid mixtures through unconsolidated sands. *Physics* **7**(9), 325–345 (1936)
- 143 Wyckoff, R., Botset, H., Muskat, M., Reed, D.: The measurement of the permeability of porous media for homogeneous fluids. *Review of Scientific Instruments* **4**(7), 394–405 (1933)

- 144 Xiu, D.: Numerical methods for stochastic computations: A spectral method approach. Princeton University Press, Princeton, NJ, USA (2010). DOI [10.2307/j.ctv7h0skv](https://doi.org/10.2307/j.ctv7h0skv)
- 145 Xiu, D., Karniadakis, G.: The Wiener-Askey polynomial chaos for stochastic differential equations. *SIAM Journal on Scientific Computing* **24**(2), 619–644 (2002). DOI [10.1137/S1064827501387826](https://doi.org/10.1137/S1064827501387826)
- 146 Yazdi, A., Norouzi, M.: Numerical study of saffman–taylor instability in immiscible nonlinear viscoelastic flows. *Rheologica Acta* **57**(8), 575–589 (2018). DOI <https://doi.org/10.1007/s00397-018-1101-0>
- 147 Yoshida, N., Levine, J., Stauffer, P.: Investigation of uncertainty in CO₂ reservoir models: A sensitivity analysis of relative permeability parameter values. *International Journal of Greenhouse Gas Control* **49**, 161–178 (2016). DOI <https://doi.org/10.1016/j.ijggc.2016.03.008>
- 148 Zeng, Y., Muthuswamy, A., Ma, K., Wang, L., Farajzadeh, R., Puerto, M., Vincent-Bonnieu, S., Eftekhari, A.A., Wang, Y., Da, C.: Insights on foam transport from a texture-implicit local-equilibrium model with an improved parameter estimation algorithm. *Industrial & Engineering Chemistry Research* **55**(28), 7819–7829 (2016)
- 149 Zitha, P., Du, D.: A new stochastic bubble population model for foam flow in porous media. *Transport in Porous Media* **83**(3), 603–621 (2010). DOI <https://doi.org/10.1007/s11242-009-9462-6>
- 150 Zitha, P.L.J.: A new stochastic bubble population model for foam in porous media. In: *SPE/DOE Symposium on Improved Oil Recovery*. Society of Petroleum Engineers (2006)